Control of Hypersonic Flight Trajectories To Minimize Heat Load

by

S. S. A. K. Javeed Nizami

A Thesis Presented to the

FACULTY OF THE COLLEGE OF GRADUATE STUDIES

KING FAHD UNIVERSITY OF PETROLEUM & MINERALS

DHAHRAN, SAUDI ARABIA

In Partial Fulfillment of the
Requirements for the Degree of

MASTER OF SCIENCE

In

MECHANICAL ENGINEERING

June, 1994

Order Number 1360396

Control of hypersonic flight trajectories to minimize heat load

Nizami, Syed Shah Ali Khasim Javeed, M.S.

King Fahd University of Petroleum and Minerals (Saudi Arabia), 1994

U·M·I

300 N. Zeeb Rd.
Ann Arbor, MI 48106

CONTROL OF HYPERSONIC FLIGHT TRAJECTORIES TO MINIMIZE HEAT LOAD

BY

S. S. A. K. JAVEED NIZAMI

A Thesis Presented to the

FACULTY OF THE COLLEGE OF GRADUATE STUDIES

KING FAHD UNIVERSITY OF PETROLEUM & MINERALS

DHAHRAN, SAUDI ARABIA

In Partial Fulfillment of the
Requirements for the Degree of

MASTER OF SCIENCE

In

MECHANICAL ENGINEERING

JUNE 1994

KING FAHD UNIVERSITY OF PETROLEUM AND MINERALS
DHAHRAN, SAUDI ARABIA

This thesis, written by

Syed Shah Ali Khasim Javeed Nizami

under the direction of his Thesis Advisor, and approved by his Thesis committee, has been presented to and accepted by the Dean, College of Graduate Studies, in partial fulfillment of the requirements for the degree of

MASTER OF SCIENCE IN MECHANICAL ENGINEERING

Thesis Committee:

Chairman (Dr. Ahmed Z. Al-Garni)

Member (Dr. Kamal A. F. Moustafa)

Member (Dr. Bekir S. Yilbas)

Member (Dr. Syed M. Zubair)

Dr. Mohammed O. Budair
Department Chairman

Dr. Ala H. Rabeh
Dean, College of Graduate Studies

Date: 25. 6. 94

Dedicated to

Memory of my Father,

Late Mr. Syed Shah Mohammed Arif Nizami

Acknowledgment

In the name of Allah, Most Merciful. Read, In the name of thy Lord and Cherisher, Who created. Created man from a [leech-like] clot. Read,and thy lord Is Most Bountiful, He Who taught [the use of] the pen. Taught man that Which he knew not. Nay, but man doth Transgress all bounds. In that he looketh Upon himself as self-sufficient. Verily, to thy Lord Is the return [of all]. (The Holy QURAN, Surah no. 96)

First and foremost, I thank ALLAH for his blessings, guidance, mercy and all that he has provided me with, and peace be upon his prophet Mohammed. This work is an attempt towards understanding more and using in the best possible way the fabulous world ALLAH has created. I ask ALLAH with sincere devotion to accept this effort.

I dedicate this work to the memory of my father late Mr. Syed Shah Mohammed Arif Nizami, whose efforts and inspiration are responsible for building my career.

I express my deep regard and sincere thanks to my advisor Dr. Ahmed Z. AL-Garni, for his guidance and advice. I thank him for introducing me to the area of Aerospace Engineering, and sharing with me his expertise. He has made my process of learning and my stay at KFUPM a pleasure.

I would like to thank my committee members: Dr. Bekir S. Yilbas, Dr. Kamal A.F. Moustafa and Dr. Syed M. Zubair, for their critique, advise and encouragement.

Finally, I express my thanks to all my family members, friends and colleagues, for standing by me at all times. In short, I should say that they have made my work a joy, and my life worth living.

Contents

List of Figures

Abstract

Name:	**Syed Shah Ali Khasim Javeed Nizami**
Title:	**Control of Hypersonic Flight Trajectories to Minimize Heat Load**
Major Field:	**Mechanical Engineering**
Date of Degree:	**Muharram, 1415H. (June, 1994G.)**

This work studies optimized controls which minimize the heat load at the stagnation point of an ascending hypersonic flight vehicle. Two types of control schemes are studied, namely, a polynomial type feedback controller and a neural controller. To validate the results obtained a comparison is made with previous analytical and numerical studies. Different cases are then studied by considering the specific impulse of the SCRAM-Jet engine as a constant or varying with Mach no. The effect of variation of initial and final attitudes is also studied. The results show that the minimized heat load is in the range of $300 - 350 kJ/cm^2$ *in general. It is also observed that the proposed neural controller performs well.*

Master of Science Degree

King Fahd University of Petroleum and Minerals

Dhahran, Saudi Arabia

Muharram 1415H. (June 1994G.)

ملخص بحث

الاسم بالكامل : سيد شاه علي قاسم جاويد نظامي .
مسمى البحث : التحكم في مسارات الطيران الفرط صوتية لتخفيض الكم الحراري .
التخصص العام : هندسة ميكانيكية .
تاريخ الدرجة : محرم ١٤١٥هـ (يونيه ١٩٩٤م) .

هذا العمل لدراسة التحكمات الأمثل التي تخفض الكم الحراري على نقطة الركود (الأسخن في الجسم) ، وذلك في المسار الصاعد للطائرة والتي تسير بسرعة فرط صوتية . وقد تم دراسة نوعين من التحكم وهما طريقة متعدد الحدود وطريقة الخليات العصبية بتغذية مرتدة . ومن أجل التأكد من صحة النتائج استخدمت دراسات تحليلية وحسابية سابقة للمقارنة . والدراسة استخدمت الدفع النوعي الثابت وكذلك المتغير بتأثير السرعة ، لمحرك نفاث ضغاطي ذو السرعة الفوق صوتية في الحارق .

وقد تم دراسة تأثير الارتفاعات عند بداية المسار ونهايته في مسار الصعود . النتائج أظهرت أن الكم الحراري المخفض هو ٣٠٠ - ٣٥٠ كيلوجول لكل سنتيمتر مربع . ولوحظ أيضاً أن استخدام التحكم بطريقة الخليات العصبية كان موفقاً .

درجة ماجستير علوم
جامعة الملك فهد للبترول والمعادن
الظهران - المملكة العربية السعودية
محرم ١٤١٥هـ (يونيه ١٩٩٤م)

Chapter 1

INTRODUCTION

1.1 Motivation

Flight has fascinated many minds, and revolutionized the idea of global commercial transportation systems. It is not only a means of transport, but it has many defense applications and it has made possible human access to the depths of the solar system. From the day man first flew a heavier than air vehicle at the beginning of this century to this present time, there has been a tremendous development in the technology. There is a continuing demand for vehicles having faster speeds and better performances in every respect.

In the second half of the present century, one of the most challenging problems encountered is of optimal flight trajectories. The problem consists of finding the best trajectory, in some sense, for the motion of a vehicle in three-dimensional space. An

interesting aspect of atmospheric flight is that the performance index may have a wide variety.

In this era the developing need for economical access to space and the commercial global transportation has increased the demand for hypervelocity, trans-atmospheric vehicles (TAV's). Such aerospace vehicles are proposed to have flexible operational characteristics approaching those of aircraft. The TAV's will take-off from and land at conventional runways and operate in low earth orbits. A lower speed variant would be a vehicle which will transport passengers or high value cargoes to any locations on the earth in a small fraction of the flight time of current jet airliners.

The missions that are proposed for the aerospace plane would require extended periods of hypervelocity flight at altitudes ranging from about 10 km to over 100 km. Such flight missions should apparently comply with certain mission requirements such as, minimum heat load, number of g's experienced during the flight, and restrictions in the quantity of fuel carried aboard the vehicle, and etc. The mission requirements change with the kind of application we consider. All these things lead to the problem of optimal flight operation trajectories.

One of the many cases where optimization of flight trajectories is essential is the severe heating problem encountered by TAV's. The missions proposed for a typical aerospace plane would use an air-breathing engine; hence it needs to travel for long periods of times at hypervelocities in denser atmosphere. Such extended periods of hypervelocities in the atmosphere causes severe heating problems. Tauber and

Menees [5] have found that the heating load of a TAV during ascent to be nine times greater than the heating load of space shuttle re-entry. This leads to very high wall temperatures to occur. No material can sustain at such high temperatures. This serious problem makes it essential for us to seek trajectories that minimize the heat load without violating the other constraints.

1.2 A look at other studies related to present work

The systematic study of flight is one of the most important and exciting scientific fields of endeavor. The mathematical modelling of flight has been known for quite some time. There has been considerable amount of work done in the area of flight trajectories. Flight trajectories of hypersonic re-entry vehicles also received considerable attention. In the 1950's, some very good work was done by Allen et. al., [6] and Chapman [7], which contributed much to the knowledge of trajectory behavior and the dynamics involved. There are also quite some published papers that dealt directly with optimization of flight trajectories performance and control. The work of Vinh [8], Griffin [9] and Vinh et. al., [10] are some of the prominent ones.

The space shuttle has been one of the prime targets of hypersonic research in the 1970's. The take-off of the space shuttle was like a rocket, in nearly a vertical

position with the least possible time spent in the lower atmosphere. Hence, the heat load was low during the ascending phase and higher during the reentry. The reentry heat load studies were done by [11] and [12]. [13] showed that ascending phase heat load is less than 2% of the reentry. But for hypersonic vehicles of the future which will use air-breathing engines, it was shown that the heat loads will be nine times more than shuttle reentry. Al-Garni [14], Al-Garni et.al. [15], Al-Garni [16] have performed studies that give an insight into the amount of heat load during ascending trajectories. In the same study in [14], a computational study was performed to find suboptimal trajectories which minimize the heat load. The study was conducted under an assumption of constant specific impulse (I_{sp}).

1.3 Scope of the work

In this study we seek to obtain Aerodynamic and thrust controls that minimize heat load of a ascending hypersonic vehicle. The study is based on modeling the trajectory optimization problem as a general nonlinear optimization problem such that, standard solution procedures are applicable. The approach was based on transforming the infinite dimensional problem to a finite dimensional optimization problem by introducing a control scheme. Two forms of controllers, a feedback controller in polynomial form, and a neural controller are studied. Results are validated by comparison with pervious numerical and analytical results. Various cases are then studied by considering

1. Constant specific impulse I_{sp},

2. variable specific impulse $I_{sp}(M)$, and

3. different initial and final altitudes.

In all there are eight cases which are arranged as CASE1a-b, CASE2a-b, Case3a-b, and CASE4a-b. The work is organized as follows.

In chapter 2, the back ground material needed for this study is presented. This covers material from different fields of engineering. Specifically, the equations of motion for flight, atmospheric properties, aerodynamic and propulsive forces, the heating model, and an introduction to neural networks is presented.

Chapter 3, presents the problem definition and solution methodology. It starts with the definition of dimensionless variables and then the conversion of equations to dimensionless form. The constraints on flight trajectories are presented next. We then go ahead to formally define the problem and then present a solution methodology.

Chapter 4, presents the simulation results for the eight cases considered in this study. The results are presented graphically in a way that is easy to interpret.

Finally in chapter 5, the conclusions of the study and suggestions for future research are presented.

Chapter 2

FUNDAMENTAL CONCEPTS AND HYPERSONIC FLIGHT

2.1 Introduction

This Chapter presents the necessary fundamental material related to the study of hypersonic flight. We begin by first deriving the general equation of motion of a rigid vehicle modelled as a point mass. The equations are first presented for the general case of rotating earth which, will be later simplified.

In the sections that follow we discuss the dynamics,the aerodynamics, the propulsion and the heat transfer equations of hypersonic flight. We also give an introduction to neural networks. This chapter is organized as follows; section 2.2 presents the equation of motion,section 2.3 presents the atmospheric model, section 2.4 discusses

the aerodynamic forces. section 2.5 the propulsive forces, section 2.6 presents the hypersonic aerodynamic heating, and finally section 2.7 presents an introduction to neural networks.

2.2 Derivation of equations of flight

In deriving the equations of motion we are making the following assumptions in the light of previous workers [1], - [17]:

1. The Earth is spherical.
2. It has a homogenous, and radially acting gravitational force vector.
3. The atmosphere is stationary and depends only on the radial distance from the centre.
4. The aircraft is considered as a point variable mass.
5. The motion of the vehicle is influenced by aerodynamic, gravitational, and propulsion forces.
6. Maneuvering of the vehicle can be achieved through the aerodynamic forces and/or through the thrust force.

The motion of the vehicle is described by the position vector $\vec{r}(t)$, velocity vector $\vec{V}(t)$, and mass m(t). The vehicle is subjected to a total force $\vec{F}$ composed of gravitational force $m\vec{g}$, the aerodynamic force $\vec{A}$ and a thrusting force $\vec{T}$, i.e.,

$$\vec{F} = \vec{T} + \vec{A} + m\vec{g} \tag{2.1}$$

From second law of motion, we have for an inertial reference frame

$$\vec{F} = m\frac{d\vec{V}}{dt}. \tag{2.2}$$

Our task is to evaluate all the terms involved in the above equations in terms of trajectory variables.

Consider the Earth to be rotating at a constant angular velocity $\vec{\omega}$ about the Z-axis. We define an inertial reference frame OX_1, Y_1, Z_1 such that O is at the centre of the earth and OX_1Y_1 is the equatorial plane. Let us also define a different reference $OXYZ$ fixed with respect to the earth (i.e., it is rotating with the same angular velocity $\vec{\omega}$). Let OZ coincide with OZ_1, see Fig.2.1 We will use the earth fixed axis $OXYZ$ as the reference frame (inertial frame) to derive the equation of motion. We can resolve the position vector $\vec{r}$ as

$$\vec{r} = r_x\hat{i} + r_y\hat{j} + r_z\hat{k}, \tag{2.3}$$

Therefore, we have

$$\frac{d\vec{r}}{dt} = \frac{\delta\vec{r}}{\delta t} + \vec{\omega} \times \vec{r}, \tag{2.4}$$

taking the derivative of Eq. (2.4) with respect to time yields the expressions for absolute acceleration,

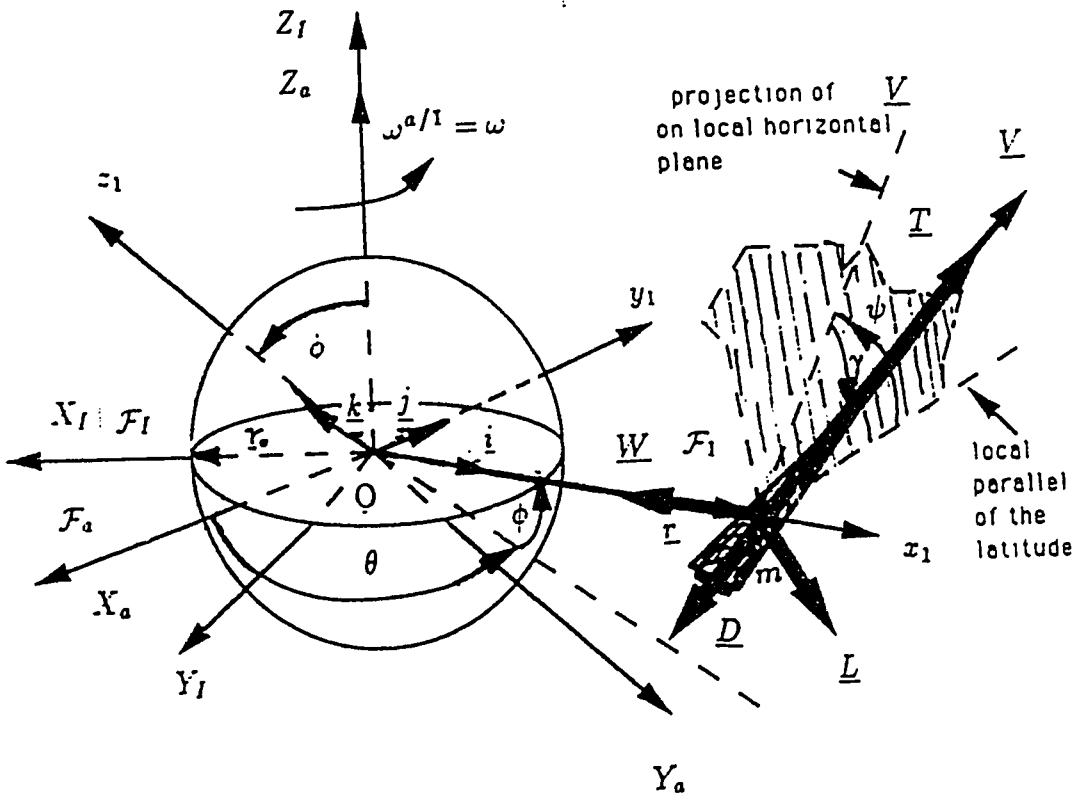

Figure 2.1: Coordinate system.

$$\frac{d\vec{V}}{dt} = \frac{\delta^2\vec{r}}{\delta t^2} + \left(\frac{dr_x}{dt}\right)\left(\frac{d\hat{i}}{dt}\right) + \left(\frac{dr_y}{dt}\right)\left(\frac{d\hat{j}}{dt}\right) + \left(\frac{dr_z}{dt}\right)\left(\frac{d\hat{k}}{dt}\right) + \vec{\omega} \times \left[\frac{\delta\vec{r}}{\delta t} + \vec{\omega} \times (\vec{\omega} \times \vec{r})\right] \tag{2.5}$$

Substituting $\frac{d\vec{\omega}}{dt} = 0$ and using the equations

$$\frac{d\hat{i}}{dt} = \bar{\omega} \times \hat{i}$$

$$\frac{d\hat{j}}{dt} = \bar{\omega} \times \hat{j}$$

$$\frac{d\hat{k}}{dt} = \bar{\omega} \times \hat{k}$$

we get

$$\frac{d\vec{V}}{dt} = \frac{\delta^2\vec{r}}{\delta t^2} + 2\vec{\omega} \times \frac{\delta\vec{r}}{\delta t} + \vec{\omega} \times (\vec{\omega} \times \vec{r}) \tag{2.6}$$

Substituting Eq. 2.6 in Eq. 2.2 we have

$$\vec{F} = m\left(\frac{\delta^2\vec{r}}{\delta t^2} + 2\vec{\omega} \times \frac{\delta\vec{r}}{\delta t} + \vec{\omega} \times (\vec{\omega} \times \vec{r})\right) \tag{2.7}$$

For convenience we re-define the notation for the time derivative and write the above equation as.

$$m\left(\frac{d\vec{V}}{dt}\right) = \vec{F} - 2m(\vec{\omega} \times \vec{V}) - m\vec{\omega} \times (\vec{\omega} \times \vec{r}) \tag{2.8}$$

In the above equation, $\vec{V}$ is the velocity of the vehicle with respect to the earth fixed axes and the time derivative is taken with respect to these axes. From the

above equation we can see that since $\vec{\omega} \neq 0$, we get two additional force terms or proportionally two additional accelerations. The term $-2(\vec{\omega} \times \vec{V})$ is the Coriolis acceleration and the term $-\vec{\omega} \times (\vec{\omega} \times \vec{r})$ is the transport acceleration. For a given distance r the transport acceleration depends on the direction of the vector $\vec{r}$,that is, on the latitude of the vehicle. This acceleration is zero when $\vec{r}$ is colinear to $\vec{\omega}$ solely when the vehicle is aligned with the poles. This acceleration is at a maximum with a value w^2r when the vehicle is in the equatorial plane. For earth since ω is small, we can neglect this component. On the other hand, the Coriolis acceleration depends on the magnitude and the direction of the velocity $\vec{V}$ of the vehicle with respect to the earth. It is zero when the flight path (i.e., $\vec{V}$) is orthogonal to the polar axis (i.e.,$\vec{\omega}$). For orbital speed, this maximum Coriolis acceleration is of the order of $10^{-3}g_0$, where g_o is acceleration of gravity at sea level. For re-entry vehicles, long navigation, or external atmospheric operation flights, this Coriolis acceleration should be retained for better accuracy, while for aircraft operation or transatmospheric(aerospace plane) performance and control, were the study is of an approximate nature and not mission specific as in this work, the term can be neglected.

Equation 2.8 and the kinematic equation

$$\frac{d\vec{r}}{dt} = \vec{V} \tag{2.9}$$

are the vector equations for the position vector $\vec{r}$ and the velocity vector $\vec{V}$. They are equivalent to six scalar equations.

Consider the earth fixed system $OXYZ$ (Fig.2.2). The position vector $\vec{r}$ is defined by the magnitude r, its longitude θ, measured from the X-axis in the equatorial plane, positively eastward, and its latitude ϕ, measured from the equatorial plane, along a meridian, positively northward.

Let us also define a rotating coordinate system $Oxyz$ such that the x-axis is along the position vector, the y-axis is along the equatorial plane in the eastward direction, and the z-axis completes the right handed coordinate system. Let γ be the angle between local horizontal plane (i.e. the plane passing through the vehicle located at the point M and orthogonal to the position vector $\vec{r}$) and the velocity vector. The angle γ is called the flight path angle. Let ψ be the angle between local parallel of the latitude and projection of $\vec{V}$ on the horizontal plane. The angle ψ is called the heading angle and is measured positively in the right handed direction about the x-axis. Let $\hat{i}, \hat{j}$ and $\hat{k}$ be the unit vector along the axes of the rotating system $Oxyz$. Therefore,we have [14]-[1]

$$\vec{r} = r\hat{i}$$

Resolving $\vec{V}$ in it's components along $Oxyz$

$$\vec{V} = (V\sin\gamma)\hat{i} + (V\cos\gamma\cos\psi)\hat{j} + (V\cos\gamma\sin\psi)\hat{k} \qquad (2.10)$$

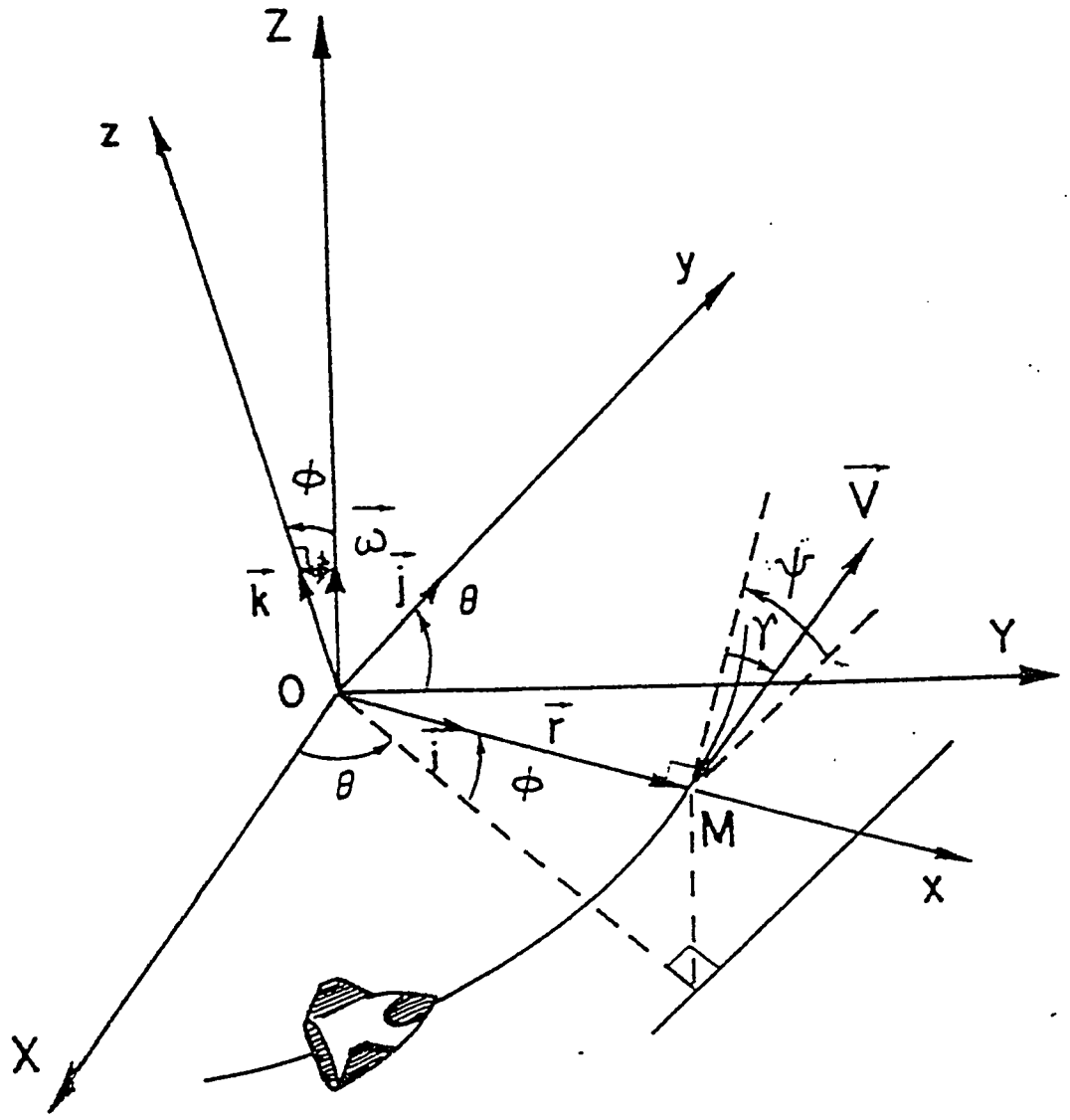

Figure 2.2: Reference frames [1].

Similarly the angular velocity $\vec{\omega}$ can be represented by its components as

$$\vec{\omega} = (\omega \sin\phi)\hat{i} + (\omega \cos\phi)\hat{k} \tag{2.11}$$

Hence we have

$$\begin{aligned} \vec{\omega} \times \vec{V} = \quad & -(\omega V \cos\gamma \cos\phi \cos\psi)\hat{i} + \omega V(\sin\gamma \cos\phi \\ & - \cos\gamma \sin\phi \sin\psi)\hat{j} + (\omega V \cos\gamma \sin\phi \cos\psi)\hat{k} \end{aligned} \tag{2.12}$$

Now

$$\vec{\omega} \times \vec{r} = (r\omega \cos\phi)\hat{j} \tag{2.13}$$

$$\omega \times (\vec{\omega} \times \vec{r}) = (-r\omega^2 \cos^2\phi)\hat{i} + (r\omega^2 \sin\phi \cos\phi)\hat{k} \tag{2.14}$$

In the force term $\vec{F}$, the gravity force for a central field is

$$m\vec{g} = -mg(r)\hat{i} \tag{2.15}$$

The aerodynamic force $\vec{A}$ can be decomposed into two force Drag, $\vec{D}$ (opposite to the velocity vectors), Lift, $\vec{L}$ (Orthogonal to the velocity vector). In symmetric flight the thrust vector $\vec{T}$ always lies in the lift drag plane as shown in Fig.2.3.

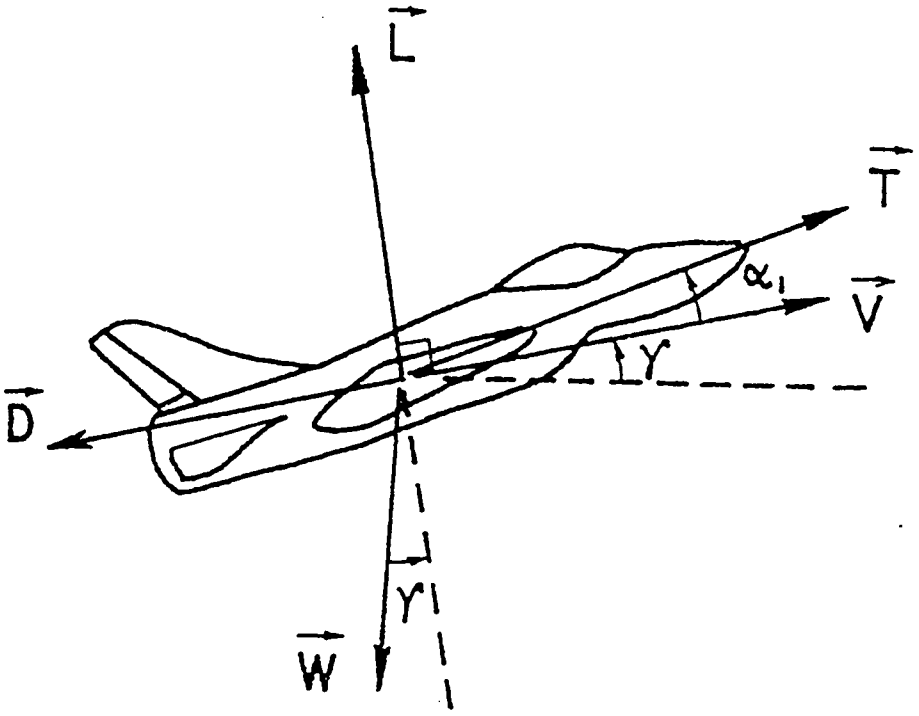

Figure 2.3: Aerodynamic and propulsive forces.

We can decompose the thrust into a tangential component T_T (along the velocity) and a normal component T_N (along the lift). The angle between thrust and the velocity vector α_1 is called "thrust angle of attack." Therefore we have

$$T_T = T\cos\alpha_1, \quad T_N = T\sin\alpha_1 \tag{2.16}$$

Now, we can write both the aerodynamic and propulsive forces together in both the directions as

$$\vec{F}_T = T\cos\alpha_1 - D, \quad \vec{F}_N = T\sin\alpha_1 + L \tag{2.17}$$

Since $\vec{F}_T$ is along $\vec{V}$ we can resolve it into components along xyz in the same way as $\vec{V}$ and we get (similar to Eq. 2.10).

$$\vec{F}_T = (\vec{F}_T\sin\gamma)\vec{i} + (\vec{F}_T\cos\gamma\cos\psi)\vec{j} + (\vec{F}_T\cos\gamma\sin\psi)\vec{k} \tag{2.18}$$

In planar flight, the vector $\vec{F}_N$ is in the $(\vec{r},\vec{V})$ plane, i.e., there is no lateral component of force F_n. But in a more general case a lateral force is produced by the control action of ailerons. If we rotate $\vec{L}$, hence $\vec{F}_N$ about the velocity vector $\vec{V}$ we create a lateral component of the force $\vec{F}_N$ which has the effect of changing the orbital plane. In such a situation, we have to resolve the force $\vec{F}_N$ along the xyz axis. To do this consider Fig.2.4, and Fig.2.5.

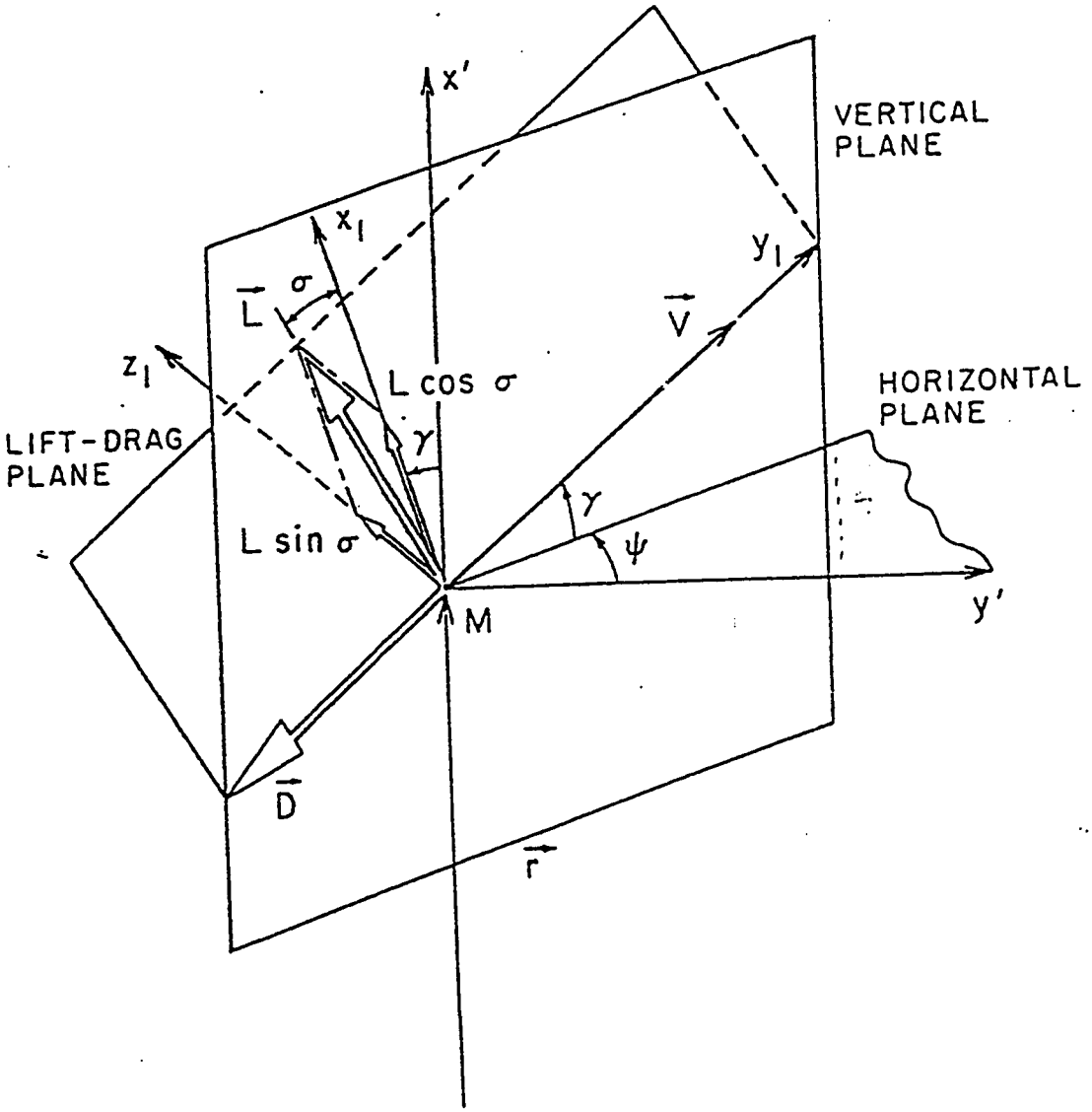

Figure 2.4: Aerodynamic forces.

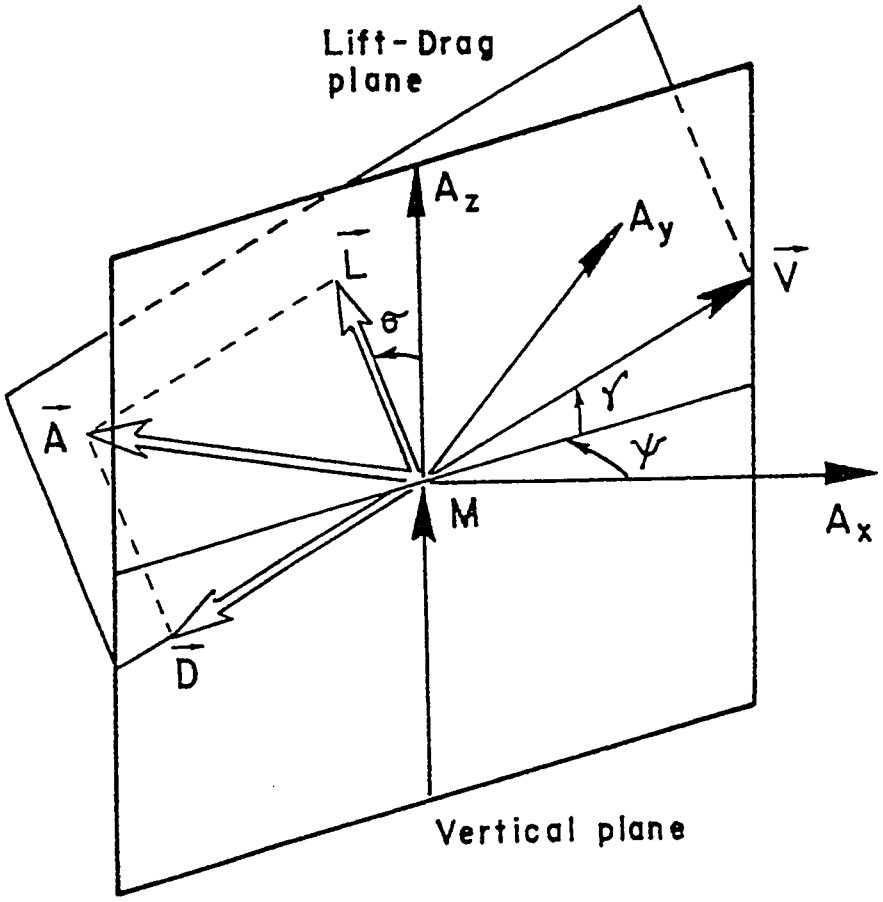

Figure 2.5: Components of the velocity and the aerodynamic force in a topocentric coordinate system.

Let us assume that the lift vector $\vec{L}$ is rotated out of the $(\vec{r}, \vec{V})$ plane due to aileron control by an angle σ. This angle is called " bank angle ". The force $\vec{F}_n$ (which is along $\vec{L}$) is decomposed as $\vec{F}\cos\sigma$ (perpendicular to $\vec{N}$ in $(\vec{r}, \vec{V})$ plane), $\vec{F}_n \sin\sigma$ (lateral force, orthogonal to $(\vec{r}, \vec{V})$ plane.)

Let us define axis $x'y'z'$ with centre at M as an axis parallel to the rotating axis xyz. Also defining $x_1y_1z_1$ to be an axis centred at point M, along the direction of $\vec{F}_n \cos\sigma$, $\vec{V}$, and $\vec{F}_n \sin\sigma$ respectively.

We can get the system x_1, y_1, z_1, from $x'y'z'$ by first rotating an angle ψ about x' and then rotating an angle γ about z'. The details of mathematical transformations are as follows [1]:

$$A' = [R_1][R_2][A_1]$$

$$R_1 = \begin{bmatrix} 1 & 0 & 0 \\ 0 & \cos\psi & -\sin\psi \\ 0 & \sin\psi & \cos\psi \end{bmatrix}$$

and

$$R_2 = \begin{bmatrix} \cos\gamma & \sin\gamma & 0 \\ -\sin\gamma & \cos\gamma & 0 \\ 0 & 0 & 1 \end{bmatrix}$$

thus, we have

$$\begin{bmatrix} x' \\ y' \\ z' \end{bmatrix} = \begin{bmatrix} 1 & 0 & 0 \\ 0 & \cos\psi & -\sin\psi \\ 0 & \sin\psi & \cos\psi \end{bmatrix} \begin{bmatrix} \cos\gamma & \sin\gamma & 0 \\ -\sin\gamma & \cos\gamma & 0 \\ 0 & 0 & 1 \end{bmatrix} \begin{bmatrix} x_1 \\ y_1 \\ z_1 \end{bmatrix}$$

Multiplying the two matrices we get

$$\begin{bmatrix} x' \\ y' \\ z' \end{bmatrix} = \begin{bmatrix} \cos\gamma & \sin\gamma & 0 \\ -\cos\psi\sin\gamma & \cos\gamma\cos\psi & -\sin\psi \\ -\sin\gamma\sin\psi & \cos\gamma\sin\psi & \cos\psi \end{bmatrix} \begin{bmatrix} x_1 \\ y_1 \\ z_1 \end{bmatrix} \tag{2.19}$$

We know that the components of F_n in the $Mx_1y_1z_1$ coordinates are $\vec{F}_n\cos\sigma$,0, $\vec{F}_n\sin\sigma$, respectively. Resolving the components in $Mx'y'z'$ coordinate system which is the same as $Oxyz$ system, using Eq. 2.19 , we get [1]

$$\begin{aligned} \vec{F}_N = \; & (F_N\cos\sigma\cos\gamma)\hat{i} - (F_N\cos\sigma\sin\gamma\cos\psi + F_N\sin\sigma\sin\psi)\hat{j} \\ & -(F_N\cos\sigma\sin\gamma\sin\psi - F_N\sin\sigma\cos\psi)\hat{k} \end{aligned} \tag{2.20}$$

Now, we have resolved all the terms in the equation Eq. 2.8 and 2.9 into components along $Oxyz$.

In order to take time derivative of the vector $\vec{r}$ and $\vec{V}$ in Eq. 2.8 and 2.9, with respect to earth fixed coordinate system $OXYZ$, using their components along rotating system Oxyz we need to evaluate the angular velocity Ω of the rotating axis. We have

$$\vec{\Omega} = \vec{\omega} + \vec{\phi}$$

we know that $\vec{\omega} = (\sin\phi\,\dot{\theta})\hat{i} + (\cos\phi\,\dot{\theta})\hat{k}$ and $\vec{\phi} = -\dot{\phi}j$. Therefore, we have

$$\Omega = \left(\sin\phi\frac{d\theta}{dt}\right)\hat{i} - \left(\frac{d\phi}{dt}\right)\hat{j} + \left(\cos\phi\frac{d\theta}{dt}\right)\hat{k} \tag{2.21}$$

Now, we get the time derivative of $\hat{i}, \hat{j}, \hat{k}$ with respect to earth fixed system OXYZ.

$$\begin{aligned}
\tfrac{d\hat{i}}{dt} &= \vec{\Omega} \times \hat{i} &&= \left(\cos\phi\tfrac{d\theta}{dt}\right)\hat{j} + \left(\tfrac{d\phi}{dt}\right)\hat{k} \\
\tfrac{d\hat{j}}{dt} &= \vec{\Omega} \times \hat{j} &&= -\left(\cos\phi\tfrac{d\theta}{dt}\right)\hat{i} + \left(\sin\phi\tfrac{d\theta}{dt}\right)\hat{k} \\
\tfrac{d\hat{k}}{dt} &= \vec{\Omega} \times \hat{k} &&= -\left(\tfrac{d\phi}{dt}\right)\hat{i} - \left(\sin\phi\tfrac{d\theta}{dt}\right)\hat{j}
\end{aligned} \tag{2.22}$$

we have $\vec{r} = r\vec{i}$. Therefore,

$$\vec{V} = \frac{d\vec{r}}{dt} = \frac{dr}{dt}\hat{i} + r\frac{d\hat{i}}{dt}$$

Substituting Eq. 2.22 we get

$$\vec{V} = \frac{d\vec{r}}{dt} = \left(\frac{dr}{dt}\right)\hat{i} + \left(r\cos\phi\frac{d\theta}{dt}\right)\hat{j} + \left(r\frac{d\phi}{dt}\hat{k}\right) \tag{2.23}$$

Comparing the coefficients of Eq. 2.10 and Eq. 2.23, we have three scalar equations.

$$\frac{dr}{dt} = V\sin\gamma \tag{2.24}$$

$$\frac{d\theta}{dt} = \frac{V\cos\gamma\cos\psi}{r\cos\phi} \tag{2.25}$$

$$\frac{d\phi}{dt} = \frac{V\cos\gamma\sin\psi}{r} \tag{2.26}$$

These are the three kinematic relations.

From Eq. 2.10 we have

$$\vec{V} = (V\sin\gamma)\hat{i} + (V\cos\gamma\cos\psi)\hat{j} + (V\cos\gamma\sin\psi)\hat{k} \tag{2.27}$$

taking derivative with respect to time (i.e., finding $\frac{d\vec{V}}{dt}$) and using Eqs. 2.22 and 2.24-2.26, we get.

$$\begin{aligned}\frac{d\vec{V}}{dt} = &\left[\sin\gamma\frac{dV}{dt} + V\cos\gamma\frac{d\gamma}{dt} - \frac{V^2}{r}\cos^2\gamma\right]\hat{i} + \left[\cos\gamma\cos\psi\frac{dV}{dt} - V\sin\gamma\cos\psi\frac{d\gamma}{dt}\right.\\ &\left. -V\cos\gamma\sin\psi\frac{d\psi}{dt} + \frac{V^2}{r}\cos\gamma\cos\psi(\sin\gamma - \cos\gamma\sin\psi\tan\phi)\right]\hat{j}\\ &+\left[\cos\gamma\sin\psi\frac{dV}{dt} - V\sin\gamma\sin\psi\frac{d\gamma}{dt} + V\cos\gamma\cos\psi\frac{d\psi}{dt}\right.\\ &\left. +\frac{V^2}{r}\cos\gamma(\sin\gamma\sin\psi + \cos\gamma\cos^2\psi\tan\phi)\right]\hat{k}\end{aligned} \tag{2.28}$$

From Eq. 2.8 we have

$$m\frac{d\vec{V}}{dt} = \vec{F} - 2m\vec{\omega}\times\vec{V} - m\vec{\omega}\times(\vec{\omega}\times\vec{r}) \tag{2.29}$$

Substituting in this equation for $\frac{d\vec{V}}{dt}$, $\vec{F}$, $\vec{\omega} \times \vec{V}$, $\vec{\omega} \times (\omega \times r)$.

We get the i-th component as

$$\sin\gamma\frac{dV}{dt} + V\cos\gamma\frac{d\gamma}{dt} - \frac{V^2}{r}\cos^2\gamma = \frac{1}{m}F_T\sin\gamma + \frac{1}{m}F_N\cos\sigma\cos\gamma$$
$$-g + 2\omega V\cos\gamma\cos\phi\cos\psi + \omega^2 r\cos^2\phi \qquad (2.30)$$

The j-th component will be

$$\cos\gamma\frac{dV}{dt} \quad -V\sin\gamma\frac{d\gamma}{dt} - V\cos\gamma\tan\psi\frac{d\psi}{dt} + \frac{V^2}{r}\cos\gamma(\sin\gamma - \cos\gamma\sin\psi\tan\phi)$$
$$= \frac{1}{m}F_T\cos\gamma - \frac{1}{m}(F_N\cos\sigma\sin\gamma + F_N\sin\sigma\tan\psi)$$
$$-\frac{2\omega V}{\cos\psi}(\sin\gamma\cos\phi - \cos\gamma\sin\psi\sin\phi) \qquad (2.31)$$

and the k-th component will be

$$\cos\gamma\frac{dV}{dt} - V\sin\gamma\frac{d\gamma}{dt} + \frac{V\cos\gamma}{\tan\psi}\frac{d\psi}{dt} + \frac{V^2}{r}\cos\gamma\left(\sin\gamma + \frac{\cos\gamma\cos\psi\tan\phi}{\tan\psi}\right)$$
$$= \frac{1}{m}F_T\cos\gamma - \frac{1}{m}F_N\left(\cos\sigma\sin\gamma - \frac{\sin\sigma}{\tan\psi}\right) \qquad (2.32)$$
$$-2\omega V\frac{\cos\gamma\sin\phi}{\tan\psi} - \omega^2 r\frac{\sin\phi\cos\phi}{\sin\psi}$$

Thus we obtain three scalar equations, solving for $\frac{dV}{dt}$, $\frac{d\gamma}{dt}$, $\frac{d\psi}{dt}$. We get

$$V\frac{d\psi}{dt} = \frac{1}{m}\frac{F_N\sin\sigma}{\cos\gamma} - \frac{V^2}{r}\cos\gamma\cos\psi\tan\phi + 2\omega V[\tan\gamma\cos\phi\sin\psi - \sin\phi]$$
$$-\frac{\omega^2 r}{\cos\gamma}\cos\psi\sin\phi\cos\phi \qquad (2.33)$$

$$\frac{dV}{dt} = \frac{1}{m}F_T - g\sin\gamma + \omega^2 r\cos\phi[\cos\phi\sin\gamma - \cos\gamma\sin\psi\sin\phi] \tag{2.34}$$

$$V\frac{d\gamma}{dt} = \frac{1}{m}F_N\cos\sigma - g\cos\gamma + \frac{V^2}{r}\cos\gamma + 2\omega V\cos\psi\cos\phi$$
$$+\omega^2 r\cos\phi[\cos\gamma\cos\phi + \sin\gamma\sin\psi\sin\phi] \tag{2.35}$$

The three equations 2.33, 2.34, and 2.35 are the force equations. We have the ω terms in the expressions because of the rotation of the earth.

The above derived equations represent a general vehicle in flight over a spherical rotating earth. It should be noted that in the above equation the vehicle mass m is variable. The equation for the change of mass is given in a later section. We have also to characterize the aerodynamic and the propulsive forces F_T, and F_N; this is also dealt in a later section.

2.3 The atmosphere and density variations

Earth's atmosphere is a dynamically changing system. It's properties such as pressure, temperature and density depend on various reasons such as location on the globe, time of day, season etc. To take all these factors into account when considering design of flight vehicle is impractical. Hence we adopt a specific set of data representing average conditions, as in U.S. Standard Atmosphere [18]. In the present study the temperature and pressure are based on the standard atmospheric data.

We can obtain the density as a function of altitude from two basic equations. The first the equation of state (empirical equation see [2]) which relates the pressure P, density ρ, and temperature T' is given as,

$$P = \rho R T' \tag{2.36}$$

where R is the universal gas constant, equal to $287 J/kgK$. The second equation relates the rate of change of pressure with altitude to the change in weight of the atmosphere and is given by (hydrostatic equation [2])

$$dP = -\rho g dr \tag{2.37}$$

where g is the acceleration due to gravity.

From equation (2.36), on differentiation we have.

$$\frac{d\rho}{\rho} = \frac{dP}{P} - \frac{dT'}{T'} \tag{2.38}$$

Which when combined with Eq. 2.36 and 2.37 gives

$$\frac{d\rho}{\rho} = -\left[\frac{g}{RT'} + \frac{1}{T'}\frac{dT'}{dr}\right] dr \tag{2.39}$$

This equation can be written as.

$$\frac{d\rho}{\rho} = -\beta\, dr \tag{2.40}$$

where

$$\beta = \frac{g}{RT'} + \frac{1}{T'}\frac{dT'}{dr} \tag{2.41}$$

in the above equation β, is called the reciprocal of the scale height.

We can write from Eq. 2.40

$$\frac{d\rho}{dt} = -\rho\beta\frac{dr}{dt} \tag{2.42}$$

We can consider β, as a constant over small intervals of altitude. The value of β, can be found by the adjustment of concordance with the standard atmosphere.

2.4 Aerodynamic forces; The drag Polar and aerodynamic -lift-to-aerodynamic-drag-ratio

In describing a model it is essential to specify the aerodynamic forces that act on the vehicle. We can get a functional form for the magnitude of aerodynamic forces A_R by doing a simple dimensional analysis ([19]) which is given by

$$A_R = \frac{1}{2} C_A \rho S V^2 \tag{2.43}$$

Where S is the surface area, C_A is a dimensionless coefficient which is a function of Mach number M, defined as the ratio of the speed of the vehicle V, to the speed

of sound a' ($M = V/a'$), the shape of the body and its attitude with respect to the relative velocity of the air. In the present work, the vehicle is considered as symmetric and the velocity vector lies in the plane of symmetry. This is a good assumption [19] for a hypersonic vehicle.

For a symmetric body vehicle, the attitude is conveniently described by the angle of attack α, which is defined as the angle between the relative velocity vector and a reference line fixed with respect to the vehicle.

In deriving the equation of motion we have considered the aerodynamic force to consist of the Drag force $\vec{D}$ opposite to the velocity vector and the Lift force $\vec{L}$ orthogonal to the velocity vector. The lift and drag forces are expressed as, [14]

$$L = L_a + L_r \tag{2.44}$$

$$D = D_a + D_r \tag{2.45}$$

Where L_a is the aerodynamic lift force, L_r the lift due to ram drag, D_a the aerodynamic drag, and D_r is the ram drag.

From Eq. 2.43 we can express the aerodynamic lift and drag forces as.

$$D_a = \frac{1}{2}\rho S V^2 C_{Da} \tag{2.46}$$

$$L_a = \frac{1}{2}\rho S V^2 C_{La} \tag{2.47}$$

Where C_{Da} and C_{La}, are called the aerodynamic drag coefficients and the aerodynamic lift coefficient respectively.

The coefficients of the lift and drag are functions of angle of attack, Mach number and reynolds number if we retain the effects of viscosity and compressibility [1].

$$C_{Da} = C_{Da}(\alpha, M, R_e), \quad C_{La} = C_{La}(\alpha, M, R_e) \tag{2.48}$$

Where R_e, is the reynolds number defined as

$$R_e = \frac{\rho V l}{\mu'} \tag{2.49}$$

In the above equation l characterizes the length or size and μ' is the viscosity.

Drag polar

At a given Mach and Reynolds number, the aerodynamic drag and lift coefficients are functions of the angle of attack. At low angles of attack, the variation of C_L is linear with respect to α. On other hand, at relatively high angles of attack, the effect of flow separation is important, and the lift coefficient varies non-linearly with the angle of attack and depends strongly on the Reynolds number. It reaches a maximum value $C_L = C_{L_{max}}$ at an angle of attack $\alpha = \alpha_{max}$, called the stalling

angle of attack. Generally speaking, the flight is restricted to angles of attack less than α_{max}. Hence, we have the constraint $C_L \leq C_{L_{max}}$ restricting the lift coefficient.

By eliminating α between the two equations 2.48 we obtain a relationship [1],

$$C_{Da} = C_{Da}(C_{La}, M, R_e) \tag{2.50}$$

For each prescribed set of values of M and R_e, the plot of the equation is called the drag polar. If we neglect the influence of the Reynolds number, the drag varies with the Mach number. For each value of M, the aerodynamic drag coefficient can be evaluated as a function of the lift aerodynamic coefficient, using Eq. 2.50. In our work, instead of the angle of attack α, we shall use the lift coefficient C_{La}, as the control variable for aerodynamic maneuvering and control. Hence it is necessary to have an explicit functional form for Eq. 2.50. for most vehicle aerodynamic configuration this can be expressed as follows [1]

$$C_{Da} = C_{Do}(M) + K_a(M)C_{La}^2 \tag{2.51}$$

where the zero-aerodynamic drag coefficient C_{Do} and the induced aerodynamic drag factor K_a are functions of the Mach number. In this form, the drag polar is referred to as the parabolic drag polar ([1],[2]-[20]).

Sometimes instead of the aerodynamic lift coefficient C_{La}, it is convenient to use the aerodynamic-lift-to-aerodynamic-drag-ratio as control variable. It is defined as [2]

$$E = \frac{C_{La}}{C_{Da}} \tag{2.52}$$

It seems that as C_{La} increases from 0 to $C_{L_{max}}$, E first increases to maximum value E^* and then decreases. If we use Eqs. 2.51 and 2.52,then

$$E(M) = \frac{C_{La}(M)}{C_{Da}(M)} = \frac{C_{La}(M)}{C_{Do}(M) + K_a(M)C_{La}^2(M)} = f(C_L(M)) \tag{2.53}$$

To find maximum E(M), we differentiate E(M) in Eq. 2.53 with respect to C_{La}(M) and equate to zero,

$$\frac{dE(M)}{dC_{La}(M)} = 0$$

$$C_{Do}(M) + K_a(M) \times C_{La}^2(M) - 2K_a(M)C_{La}^2(M) = 0$$

By solving for C_{La}^*(M), we get

$$C_{La}^*(M) = \sqrt{\frac{C_{Do}(M)}{K_a(M)}} \tag{2.54}$$

From Eqs. 2.51 and 2.54 we have $C_{Da}^*(M)$,

$$C_{Da}^* = 2C_{Do}(M) \tag{2.55}$$

Solving for $E^*(M)$ which is $E_{max}(M)$ from Eqs. 2.53, 2.54 and 2.55 we get,

$$E^*(M) = \frac{1}{2\sqrt{K_a(M)C_{Do}(M)}} \tag{2.56}$$

We thus have from Eqs. 2.54, 2.55 and 2.56 the classical solutions, where C^*_{La}(M), C^*_{Da}(M), and $E^*(M)$ are the functions of Mach number.

For the analysis of the optimal trajectories, it is assumed that the functions C_{Do}(M),K_a(M) and $C_{L_{max}}$(M) are known explicitly as functions of the Mach number. For any given vehicle this is done by modelling these functions, based on aerodynamic data obtained from wind tunnel measurements and flight tests or occasionally from theoretical estimates. For a supersonic aircraft, it is not advisable to use a single modelling of the function for a complete range of speed from low subsonic to high supersonic speeds.

In the hypersonic flight region, we can show that it has the Mach number independence principle ([1], [2], and [19]), where

$$C_{La}, C^*_{La}, C_{Da}, C^*_{Da}, C_{Do}, K_a, E, \text{and} E^*$$

become relatively independent of the Mach number, then Eqs. 2.52, 2.54, 2.55 and 2.56 become

$$C_{Da} = C_{Do} + K_a C_L^2 \tag{2.57}$$

$$E = \frac{C_{La}}{C_{Da}} \tag{2.58}$$

$$C_{La}^{*} = \sqrt{\frac{C_{Do}}{K_a}} \tag{2.59}$$

$$C_{Da}^{*} = 2C_{Do} \tag{2.60}$$

$$E^{*} = \left(\frac{C_{La}^{*}}{C_{Da}^{*}}\right) = \frac{1}{2\sqrt{K_a C_{Do}}} \tag{2.61}$$

Aerodynamic lift-to-drag-ratio

There are two methods for determining the lift–to–drag ratio; analytical and experimental. One of the means to obtain analytical results is to use Newtonian model for fluid flow [2]. It is observed that in hypersonic flow the stream lines are parallel and hence come close to matching the Newtonian model. Consider (Fig. 2.6) a flat plate inclined at an angle of α to the free stream velocity. For a Newtonian flow , the time rate of change of momentum due to particles striking the surface is equal to the product of mass flow rate and the change in normal component of velocity. This in turn is equal to the force on the surface from Newtons second law. Hence

$$A_R = \rho_\infty V_\infty^2 S \sin^2 \alpha \tag{2.62}$$

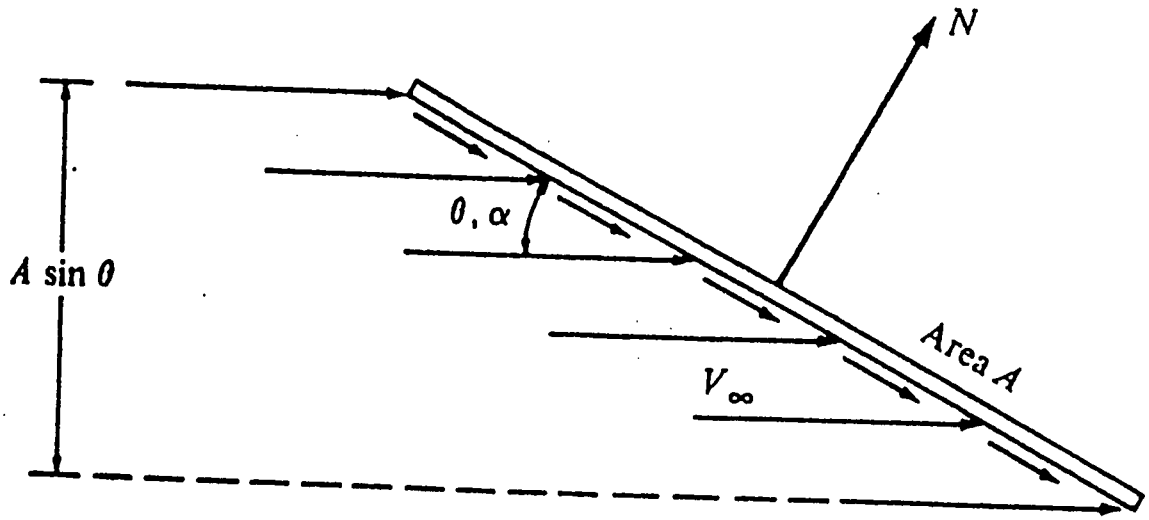

Figure 2.6: Model for the derivation of newtonian sine-squared law.

and

$$P - P_\infty = \frac{A_R}{S} = \rho_\infty V_\infty^2 \sin^2 \alpha \tag{2.63}$$

where $(P - P_\infty)$ is the differential pressure over the flat plate surface and ρ_∞ , V_∞ the density and velocity of the free stream respectively.

In terms of the definition of the pressure coefficient we may write.

$$C_p = \frac{P - P_\infty}{\frac{1}{2}\rho_\infty V_\infty^2} = 2 \sin^2 \alpha \tag{2.64}$$

This is the famous Sine-Squared law for the Pressure Coefficient. The above equation can be modified in a more general situation as ([2])

$$C_p = C_{p,max} \sin^2 \alpha \tag{2.65}$$

where

$$C_{pmax} = \frac{P_{0,2} - P_\infty}{\frac{1}{2}\rho_\infty V_\infty^2} \tag{2.66}$$

$C_{p,max}$ is the maximum pressure coefficient which occurs at the stagnation point, $P_{0,2}$ is the total pressure behind a normal shock wave.

From the geometry of the Fig. 2.6 we get

$$L_a = A_R \cos \alpha \tag{2.67}$$

$$D_a = A_R \sin \alpha \tag{2.68}$$

Substituting for A_R from Eq. 2.62 we get

$$L_a = \rho_\infty V_\infty^2 A \sin^2\alpha \cos\alpha \tag{2.69}$$

$$D_a = \rho_\infty V_\infty^2 A \sin^3\alpha \tag{2.70}$$

and thus the aerodynamic lift–to–drag ratio becomes

$$E = \frac{L_a}{D_a} = \cot\alpha. \tag{2.71}$$

The newtonian results for the lift and drag coefficients and lift - to -drag ratio for a flat plate as a function of angle of attack is shown in Fig. 2.7. From the figure we can observe the following important characteristics,

1. The lift coefficient increases gradually with angle of attack and the maximum occurs at $\alpha = 54.7°$, after which C_L decreases.

2. The lift coefficient varies non-linearly with the angle of attack α even at low values of α ranging between 0 deg to 15 deg. This is in direct contrast to the variation of C_L in subsonic flight.

3. It should be noted that $\frac{L}{D}$ increases monotonically as α is decreased. If we consider this trend at $\alpha \to 0$, $\frac{L}{D} \to \infty$, which is misleading. To do a correct analysis we should consider the effect of the skin friction, the result is shown by means of the dashed lines from this we see $\frac{L}{D}$ reaches a maximum at a small α and then decreases to zero at $\alpha = 0$.

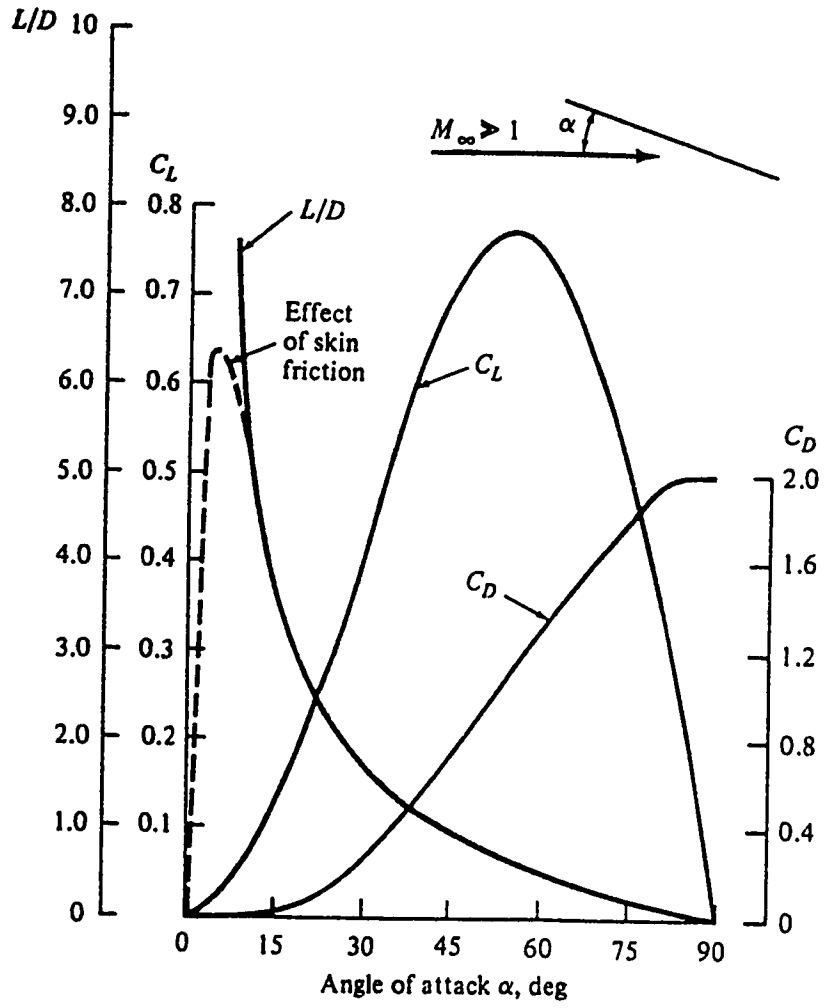

Figure 2.7: Newtonian results for lift and drag coefficients and Lift-to-drag ratio for a flat plate as a function of angle of attack [2].

The result from the flat plate are interesting from an academic point of view. Practically all vehicles should have certain volume to carry, fuel, payload, people, and etc. A more realistic configuration is shown in Fig. 2.8 from [3], which shows a 3-view drawing of a hypersonic vehicle. The wind tunnel data and the theoretical results for this configuration are shown in Fig. 2.9. It is seen that the lift coefficient varies non-linearly with α, a trend consistent with that for flat plate. We can also observe that C_L is very insensitive to the Reynolds number. The lift–to–drag ratio versus angle of attack is shown in Fig. 2.10. We observe from the figure that maximum $\frac{L}{D}$ occurs in the angle-of-attack range of 3 to 5 deg.The values of $\left(\frac{L}{D}\right)_{max}$ ranges from 4.5 to about 6, depending on the Reynolds number. Figure. 2.11 gives a drag polar (C_D versus C_L^2) for the configuration shown in Fig. 2.8. The figure shows that the experimental data are almost linear. Which indicates that the drag polar given by equation 2.57 is reasonable for the hypersonic vehicle. For, $M_\infty > 1$ there is a general correlation for $\left(\frac{L}{D}\right)_{max}$ based on actual flight vehicle data:

$$E^* = \left(\frac{L}{D}\right)_{max} = \frac{4(M_\infty + 3)}{M_\infty} \tag{2.72}$$

This equation is shown as a solid curve in the figure. The figure also shows open circle data points, corresponding to a variety of hypersonic vehicle designs. For more details see [21] and [22].

In [4] a generic aerodynamic model is presented. The geometry is built up of simple geometric shapes, see Fig. 2.12 . The data for $\frac{L}{D}$ of this configuration is shown

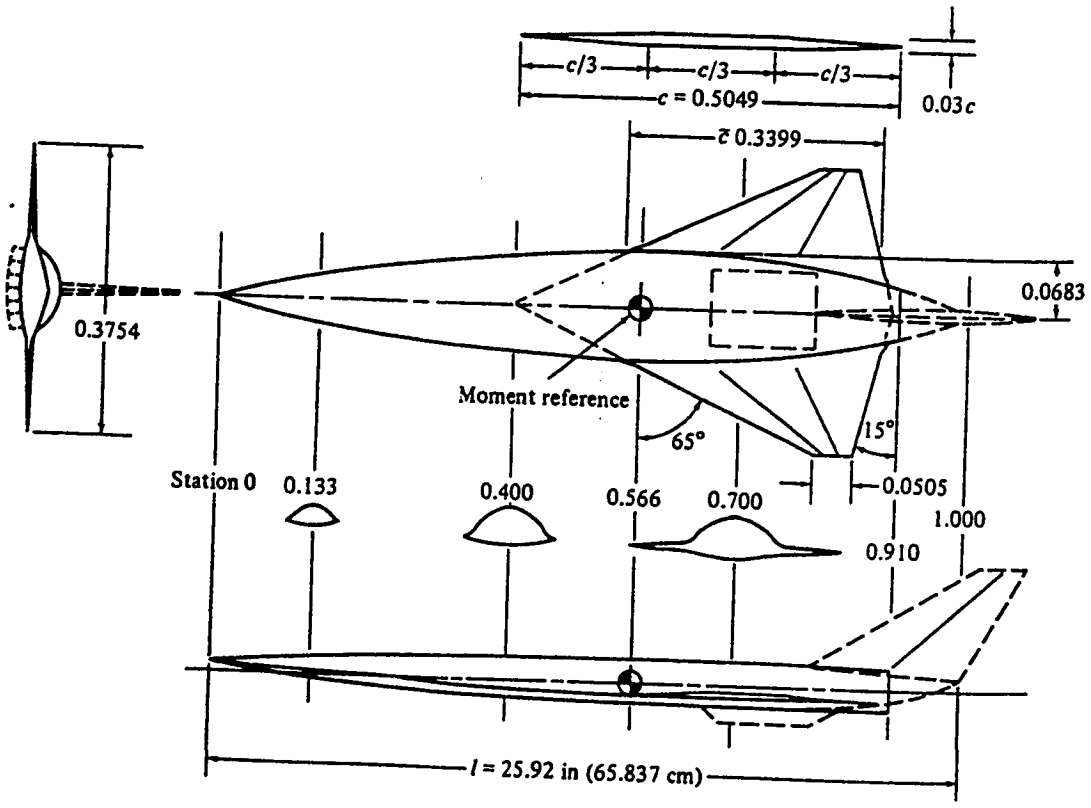

Figure 2.8: A generic hypersonic-transport configuration. [3]

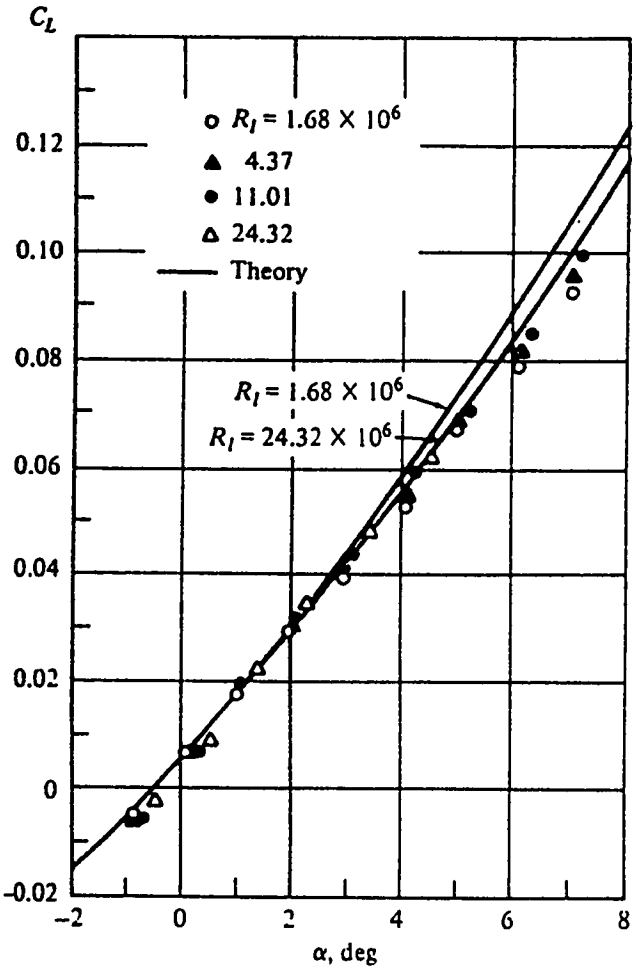

Figure 2.9: Lift curve for the hypersonic-transport configuration, $M_\infty = 8$ [3].

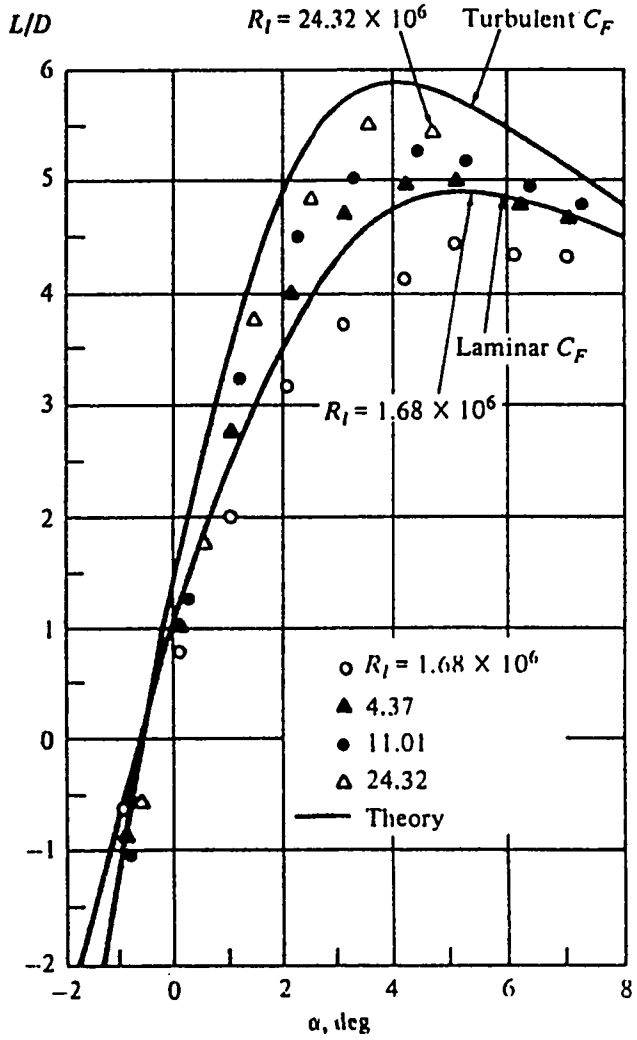

Figure 2.10: Lift-to-drag ratio for the hypersonic-transport configuration, $M_\infty = 8$ [3].

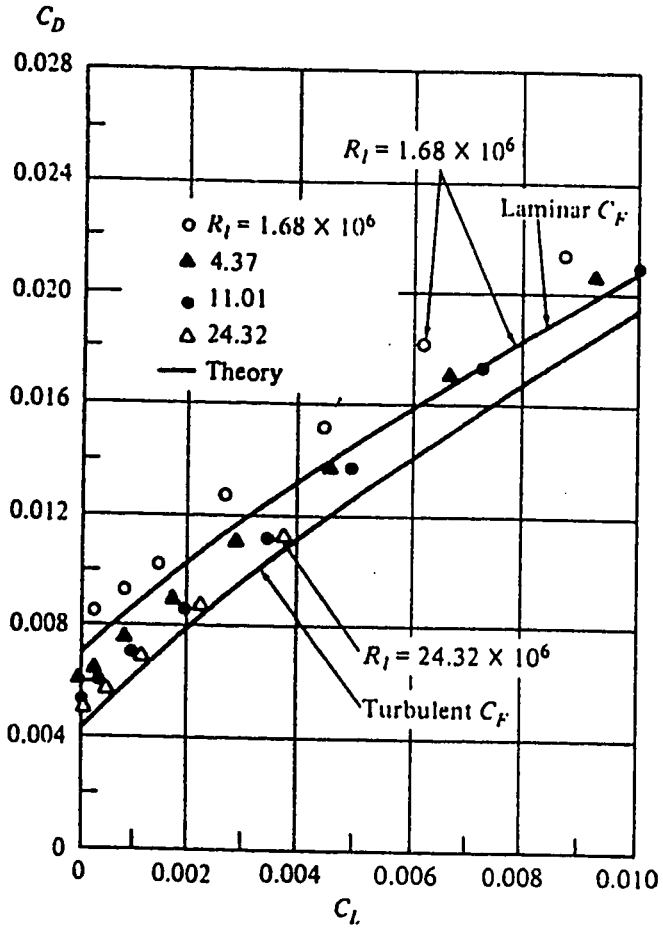

Figure 2.11: Drag polar for the hypersonic-transport configuration, $M_\infty = 8$ [3].

in figure. Figure 2.13,2.14 shows $\frac{L}{D}$ V.D Mach numbers for all α's. Figures. 2.15,2.16 are 3-D plots for the same data.

2.5 The propulsive force and engine model

The propulsive forces play a very important role in the overall performance and design of flight vehicles. The Propulsive forces generated are based on the fundamental laws of mechanics, (i.e.) force is exerted on a solid surface by means of surface pressure and shear stress distribution. In a jet propulsion system this is achieved by imparting a large change of momentum to gases. A jet engine is a device which takes in air at free stream velocity V_∞ Fig. 2.17, heats the air by combustion of fuel, and blasts the hot gases at a much higher velocity V_e. This creates a change in momentum, based on Newton's third law an equal and opposite reaction produces a thrust (Fig. 2.17.b). The true fundamental source of the thrust of a jet engine is the net force produced by the pressure and shear stress distribution exerted over the surface of the engine [2], see Fig. 2.17. From Fig. 2.17.b, let x denote the flight direction, the thrust of the engine in the direction is equal to the x-component of P_s integrated over the complete internal surface, plus that of P_∞ integrated over the external surface (i.e.),

$$T_n = \int (P_s dx)_x + \int (P_\infty ds)_x \tag{2.73}$$

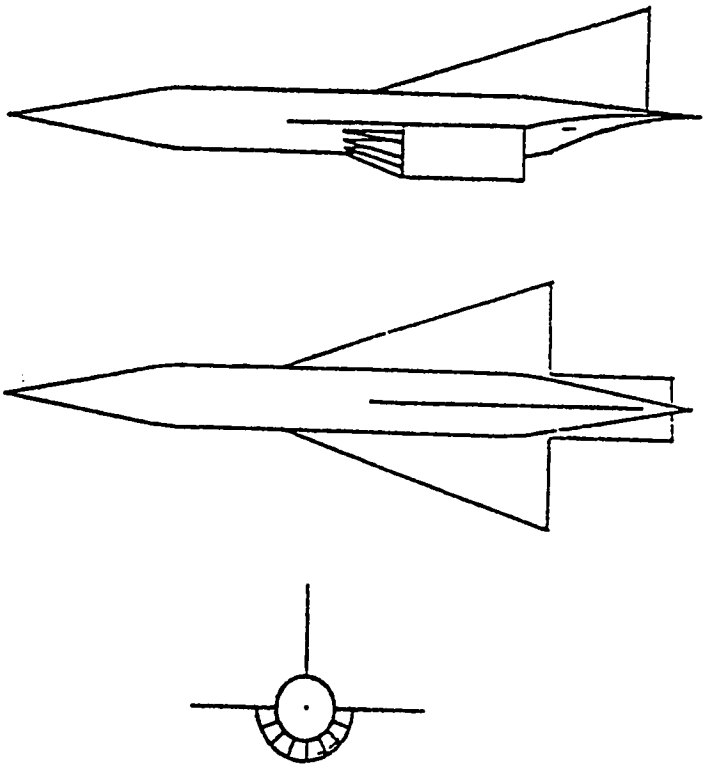

Figure 2.12: Aircraft configuration, three views [4].

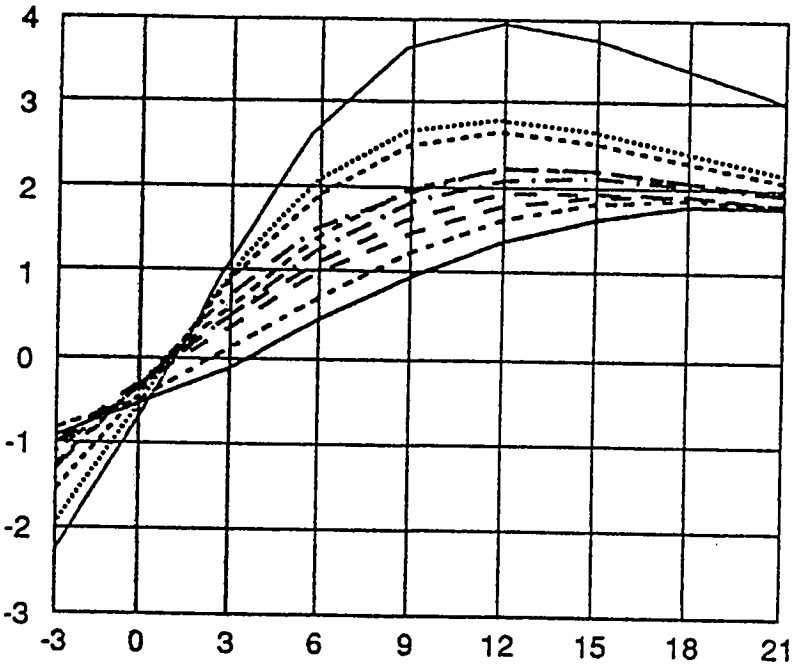

Figure 2.13: L/D vs α for all Mach numbers [4].

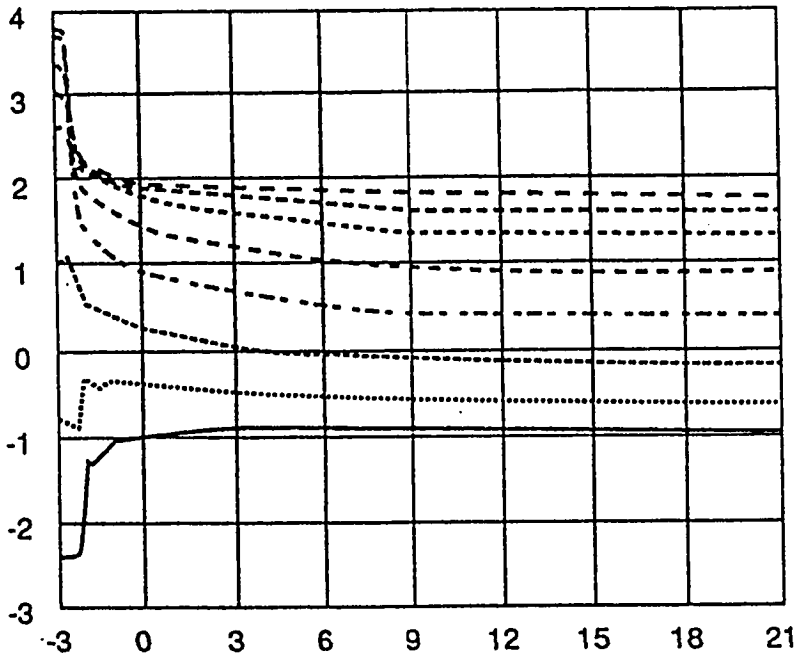

Figure 2.14: L/D vs Mach number for all α's [4].

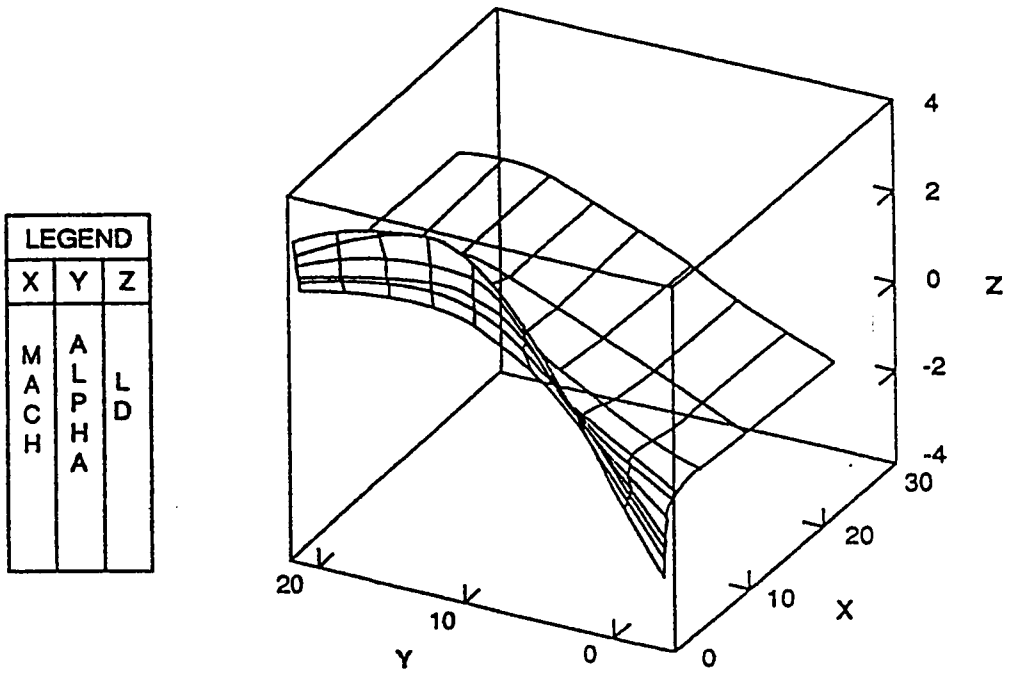

Figure 2.15: L/D vs Mach and α [4].

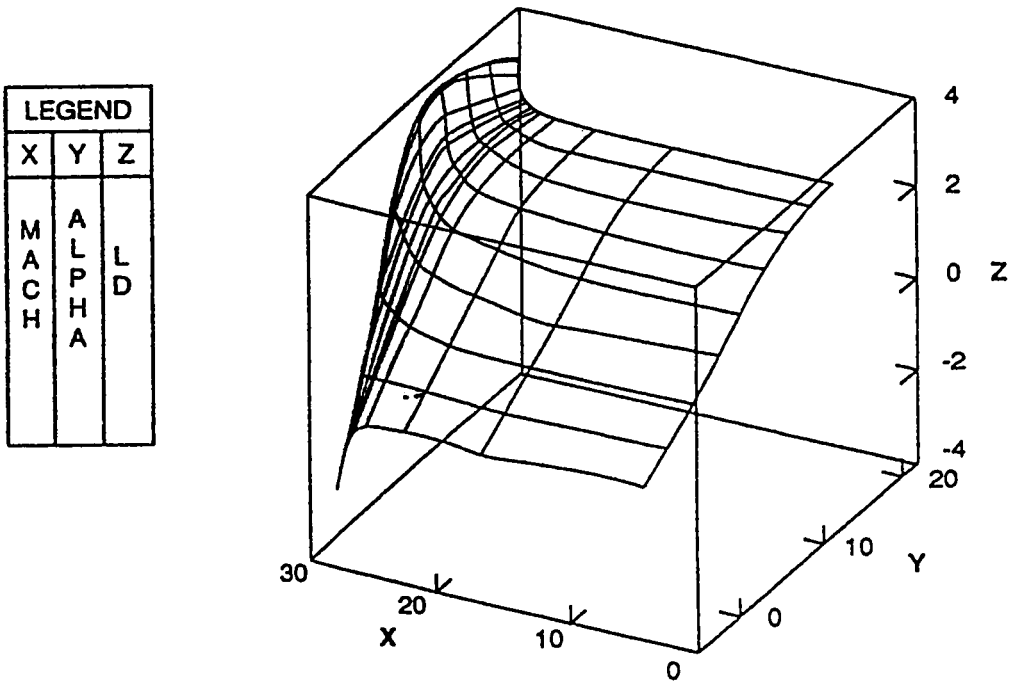

Figure 2.16: L/D vs Mach and α, (rotated from previous view) [4].

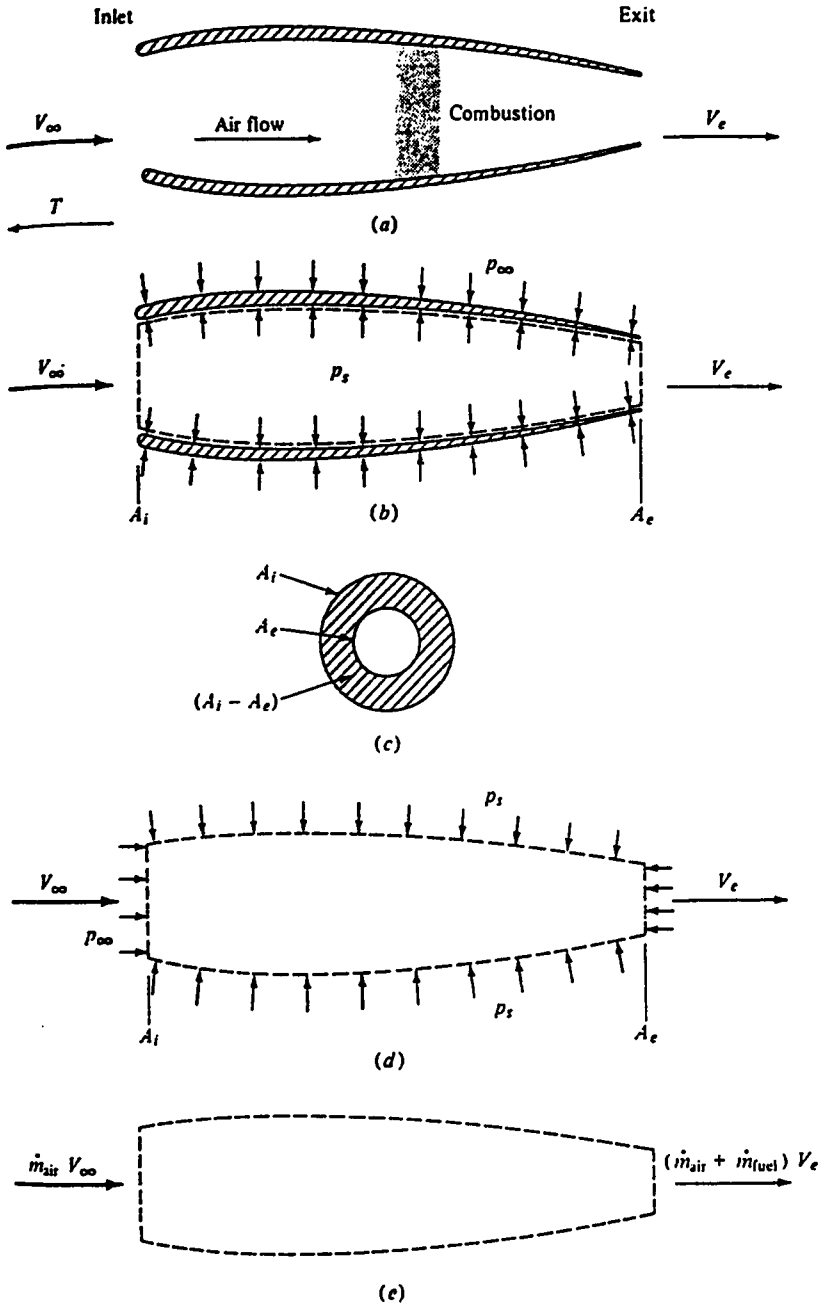

Figure 2.17: Illustration of the principle of jet propulsion. (a) Jet propulsion engine. (b) Surface pressure on inside and outside surfaces of duct. (c) Front view, illustrating inlet and outlet areas. (d) Control volume for flow through duct. (e) Change in momentum of the flow through the engine [2].

since P_∞ is a constant, the last term becomes,

$$\int (P_\infty ds)_x = P_\infty \int (ds)_x = P_\infty (A_i - A_e) \tag{2.74}$$

where A_i and A_e are inlet and outlet areas of the duct. Substituting in Eq. 2.73 we get

$$T_n = \int (P_s ds)_x + P_\infty (A_i - A_e) \tag{2.75}$$

The integral in the above equation is not easy to handle in the above form. It could be evaluated as follows. Consider Fig. 2.17.d the x-component of the force on the gas inside the control volume is.

$$F = P_\infty A_i + \int (P_s ds)_x - P_e A_e \tag{2.76}$$

This force is equal to the time rate of change of momentum. The time rate of change of momentum is given by $(\dot{m}_{air} + \dot{m}_{fuel})V_e - \dot{m}_{air} V_\infty$ therefore,

$$F_x = (\dot{m}_{air} + \dot{m}_{fuel})V_e - \dot{m}_{air} V_\infty \tag{2.77}$$

Substituting in Eq. 2.76 we get

$$(\dot{m}_{air} + \dot{m}_{fuel})V_e - \dot{m}_{air} V_\infty = P_\infty A_i + \int (P_s ds)_x - P_e A_e \tag{2.78}$$

Solving for the integral term we get

$$\int (P_s ds)_x = (\dot{m}_{air} + \dot{m}_{fuel})V_e - \dot{m}_{air}V_\infty + P_e A_e - P_\infty A_i \tag{2.79}$$

Thus the final result for the engine thrust is obtained by substituting the above equation in Eq. 2.75 which gives,

$$T_n = (\dot{m}_{air} + \dot{m}_{fuel})V_e - \dot{m}_{air}V_\infty + P_e A_e - P_\infty A_i + P_\infty(A_i - A_e) \tag{2.80}$$

Which on simplification yields

$$T_n = (\dot{m}_{air} + \dot{m}_{fuel})V_e - \dot{m}_{air}V_\infty + (P_e - P_\infty)A_e \tag{2.81}$$

Equation 2.81 is the fundamental thrust equation for jet Propulsion.

For Turbojet engine $m_{air} >> m_{fuel}$, then

$$T_n = \dot{m}_{air}(V_e - V_\infty) + (P_e - P_\infty)A_e. \tag{2.82}$$

Engine model

It is seen that the main performance characteristics of a propulsion system are the thrust and the specific fuel consumption. In the simplest form we can express the mass flow rate of the engine as

$$\frac{dm}{dt} = -\frac{T_n}{I_{sp}(M)\, g_o} \tag{2.83}$$

Where T_n is the net thrust and g_o is the acceleration due to gravity at sea level. It is observed that I_{sp} depends primarily on the Mach number and slightly on the thrust settings and altitude. For the analysis of optimal trajectories, the function $I_{sp}(M)$ should be modelled based on the engine performance characteristics.

In this study the I_{sp} has been modelled as a function of Mach number. The data for I_{sp} as a function of Mach number is given in [23] . Detailed values are given in [4] for different angles of attack and air fuel ratio. We have curve fitted this data with polynomials to obtain a functional relationship. These results are given in chapter 3.

The thrust generated by the turbojet engine is high, but they have a low efficiency. The efficiency of an engine is denoted by the thrust specific fuel consumption (C) (or TSFC); the lower the C the higher is the efficiency. To overcome this draw back turbo fan engines were developed. In these engines the concepts of pure turbojet and the propeller are combined. This concept was further extended by replacing the ducted fan with a propeller, with the turbine driving both the compressor and the propeller. Such a combination is called a turboprop. The turboprop engines have relatively higher efficiencies.

Another concept of a jet engine is a ramjet. In this type of engine all rotating machinery is eliminated. In a ramjet engine, air is inducted through the duct inlet at V_∞, decelerated in diffuser, burned in a region where fuel is injected, and then blasted out the exhaust nozzle at a very high velocity V_e. One disadvantage of a ramjet

engine is that, in order to start and operate, it should be already in motion. Another disadvantage of ramjet engines is there low efficiency at subsonic speeds. However at supersonic speed their efficiency improves. Figure 2.18 shows the comparison of the thrust specific fuel consumption of ramjet and turbojets. We can see that at supersonic speeds the efficiency of ramjet engine improves. For turbojet the curve in figure is terminated at Mach 3, this is due to the reason that at higher Mach number, the turbojets must increase the combustion temperature. However material limitations do not permit this. On the other hand ramjets have no turbine and hence can operate at much higher Mach numbers. This consideration makes it the only choice in the present day technology to fly at supersonic speeds. The ramjet engine also cannot operate beyond Mach 6, beyond which the walls of the ramjet tend to fail structurally [24].

Thus like turbojets, conventional ramjets are also limited by material problems, although at high Mach numbers. Moreover, if the temperature of the air entering the combustor is too high, when the fuel is injected, it will be decomposed by high temperatures rather than be burned. This means that the fuel will absorb energy instead of releasing energy. Thus the engine will become a drag machine, rather than a thrust producing machine. For hypersonic flight at very high Mach numbers, something different has to be done, to achieve the desired results. This led to the concept of a supersonic combustion ramjet, the SCRAM-jet. In a SCRAM-jet, the flow entering the diffuser is at a high Mach number. The diffuser decelerates the

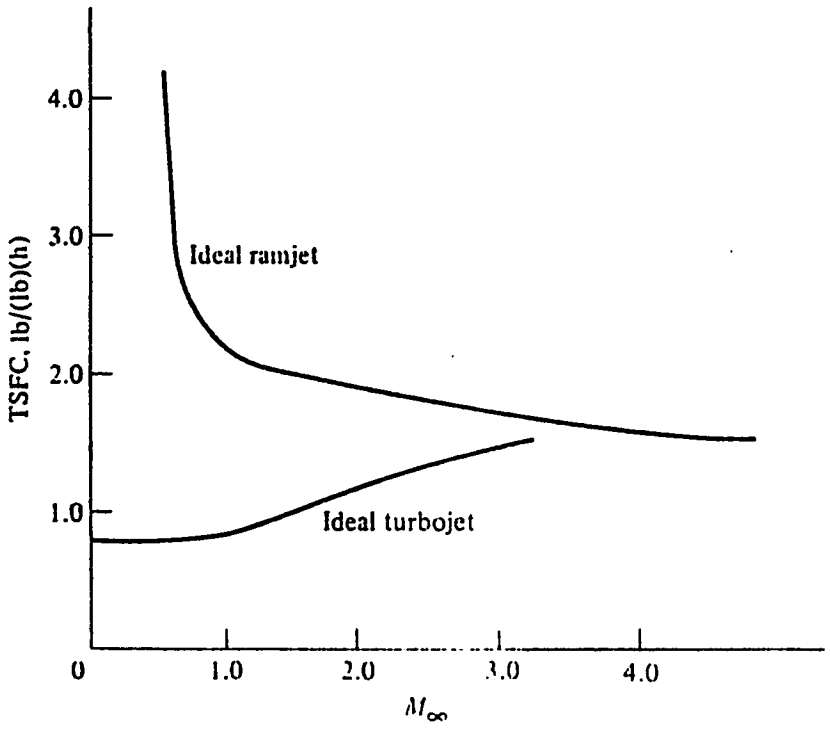

Figure 2.18: Comparison of thrust-specific fuel consumption for ideal ramjet and turbojet engine [2].

airflow only enough to obtain a reasonable pressure ratio. The flow is still supersonic upon entering the combustor, unlike the other engines discussed earlier. Fuel is added to the supersonic stream, where "supersonic combustion " takes place. In this way the flow field throughout the SCRAM-jet is completely supersonic. This keeps the static temperatures low, thus avoiding the problem of fuel decomposition and material failure. Therefore the power plant for a hypersonic transport in the future will most likely be a SCRAM-jet [2].

2.6 Hypersonic aerodynamic heating

In this section we introduce the hypersonic heating equation of viscous flow. From the practical aspect of the design of a hypersonic vehicle, we are concerned with the prediction of surface heat transfer and the skin friction. Of these two, surface heat transfer is usually the dominant aspect that derives the design characteristics of conventional hypersonic vehicles, although skin friction is very important in tailoring the aerodynamic efficiency of slender vehicles([25]). An aerospace plane (TAV) designed to takeoff horizontally from an airport and go into orbit using an air breathing propulsion, needs to acquire enough kinetic energy within the sensible atmosphere to coast into a low earth orbit. At such high speeds ($M > 10$) within the dense atmosphere, aerodynamic heating will be very severe and will form a dominant factor in the vehicle's design.

The Aerodynamic heating to the surface is described by [26]:

$$\dot{Q}_w = \rho_e u_e C_H (h'_{aw} - h'_w) = \rho_\infty V_\infty C_H (h'_{aw} - h'_w) \tag{2.84}$$

where $\dot{Q}_w$ is the local heat transfer rate (energy per second per unit area), $(h'_{aw} - h'_w)$ is the enthalpy difference, and where h'_{aw} is the enthalpy at the wall when $\dot{Q}_w = 0$. C_H is the Stanton number, ρ_e and u_e are density and velocity, respectively at the edge of the boundary layer, and they are functions of location x, and where ρ_∞ and V_∞ are free stream density and velocity, respectively. Also, we have

$$\dot{Q}_w \propto \frac{1}{\sqrt{R_N}} \tag{2.85}$$

which states that stagnation-point heating varies inversely with the square root of the nose radius ([25]); hence to reduce the heating, the nose radius should be increased. If we assume the approximation that $h'_{aw} \approx h'_o$, where h'_o is the total enthalpy, given as

$$h'_o = h'_\infty + \frac{V_\infty^2}{2} \tag{2.86}$$

At hypersonic speeds, $\frac{V_\infty^2}{2}$ is much larger than h'_∞ hence h'_o is given by

$$h'_o \approx \frac{V_\infty^2}{2} \tag{2.87}$$

Moreover, the surface temperature, although hot by normal standards, still must remain less than the melting or decomposition temperature of the surface material. Hence the surface enthalpy h'_w is usually much less than h'_o at hypersonic speed,

$$h'_o >> h'_w \tag{2.88}$$

Combining Eq. 2.84, 2.87 and 2.88 we obtain the approximate relationship

$$\dot{Q}_w \approx \frac{1}{2}\rho_\infty V_\infty^3 C_H \tag{2.89}$$

This shows that the aerodynamic heating increases with the cube of the velocity, and increases very rapidly in the hypersonic flight regime. Moreover, from Eq. 2.89, we can understand why the major aerodynamic heating for the transatmospheric vehicle (TAV) is encountered during ascent rather than during entry. A TAV will accelerate to orbital velocity within the sensible atmosphere(using air-breathing propulsion). The resulting high velocity will be combined with relatively high ρ_∞ to yield very high heating values. In contrast, on atmospheric entry, the transatmospheric vehicle will follow a gliding flight path where deceleration to lower velocities will take place at higher altitudes, resulting in lower heating rates than are encountered during ascent. For more practical engineering analysis and design, we can simplify and develop more approximate methods. The simplest may be to use generalized form of Eq. 2.89

$$\dot{Q}_w = C_Q \rho_\infty^{N'} V_\infty^{M'} \tag{2.90}$$

where the units for $\dot{Q}_w$, ρ_∞ and V_∞ are W/cm^3 , kg/m^2 and m/s, respectively. N', M' and C_Q are assumed to be constants. This equation applies in the flight regime for which boundary- layer theory is valid. It is a good approximation for both laminar [27] and turbulent [28] convection at a catalytic surface in the absence

of boundary layer mass additions. The numerical values used in this equation are taken from Marvin and Deiwert [28]-[29] for the stagnation point and turbulent flat-plate heating, respectively. For stagnation point:

$$M' = 3, \;\; N' = .5, \;\; C_Q = 1.83 \times 10^{-8} R_n^{-\frac{1}{2}} \left(1 - \frac{h'_w}{h'_o}\right) \tag{2.91}$$

where R_n is the nose radius in meters, and h'_w and h'_o are the wall and total enthalpy's, respectively.

For laminar flat plate:

$$M' = 3.2, \; N' = .5, \; C_Q = 2.53 \times 10^{-9} (\cos\phi')^{\frac{1}{2}} (\sin\phi') X'^{-\frac{1}{2}} \left(1 - \frac{h'_w}{h'_o}\right) \tag{2.92}$$

where ϕ' is the local body angle with respect to the free stream, and X' is the distance measured along the body surface in meters.

For turbulent flat plate:

$$\text{For} \quad V_\infty \leq 3962 m/s, \;\; N' = .8, \;\; M' = 3.37$$

$$C_Q = 3.89 \times 10^{-8} (\cos\phi')^{1.78} (\sin\phi')^{1.6} X_T'^{-\frac{1}{5}} \left(\frac{T'_w}{556}\right)^{-\frac{1}{4}} \left(1 - 1.11 \frac{h'_w}{h'_o}\right)$$

$$\text{For} \quad V_\infty > 3962 m/s, \;\; M' > 3.37$$

$$C_Q = 2.2 \times 10^{-9} (\cos\phi')^{2.08} (\sin\phi')^{1.6} X_T'^{-\frac{1}{5}} \left(1 - 1.11 \frac{h'_w}{h'_o}\right)$$

where X'_T is the distance measured along the body surface in turbulent boundary layer.

The validity of these correlations is reasonable as long as the flight conditions are such that boundary layer theory is valid. They are useful for preliminary analysis and are not recommended for more detailed work.

In this study we considered the stagnation point heat load since the maximum heat occurs there. Tauber et. al.,[5] have made an engineering estimate of the aerodynamic heating to an aerospace plane (TAV) for both ascent and re-entry. Their estimate gives both maximum heat transfer rate(in W/cm^2) and total heat transfer(in kJ/cm^2) at the stagnation point. Two important results are observed: (1) The TAV's stagnation point heating load is three times that of shuttle re-entry. Even more striking is the fact that the ascent heat load of TAV is about 9 times the heat load of shuttle re-entry. (2) The major aero-thermal heating of the hypersonic vehicle occur during ascent rather than during re-entry. This is because during the ascent, high velocities combined with high ambient density result in high heating values, in contrast to re-entry conditions (low heating rate), in which deceleration to lower velocities takes place at higher altitudes.

2.7 Neural networks: An introduction

Artificial neural networks (ANN) are biologically inspired tools, they perform functions analogous to the elementary functions of the biological neuron, Fig. 2.19. Artificial neural networks exhibit characteristics of the human brain such as, learning from previous experience, abstract essential characteristics from inputs containing irrelevant data etc. Despite these similarities they are no way near to the functioning capabilities of the brain. They draw comparison due to the fact that ANN's evolved as a result of human effort to study the organization of the human brain [30]. It is helpful to understand the functioning of the human nervous system to comprehend this analogy.

The human nervous system, built of cells called neurons, is of staggering complexity. An estimated 10^{11} neurons participate in perhaps 10^{15} interconnection over transmission paths that may extend to a meter or more.

Each neuron is an electrically active cell. They interact with one another through the flow of local ionic currents between them. These ionic currents are driven by a voltage difference across the neuron's cell membrane.

2.7.1 Artificial neuron

The artificial neuron was designed to mimic the characteristics of the biological neuron as understood by the human mind. In essence a set of inputs are applied to

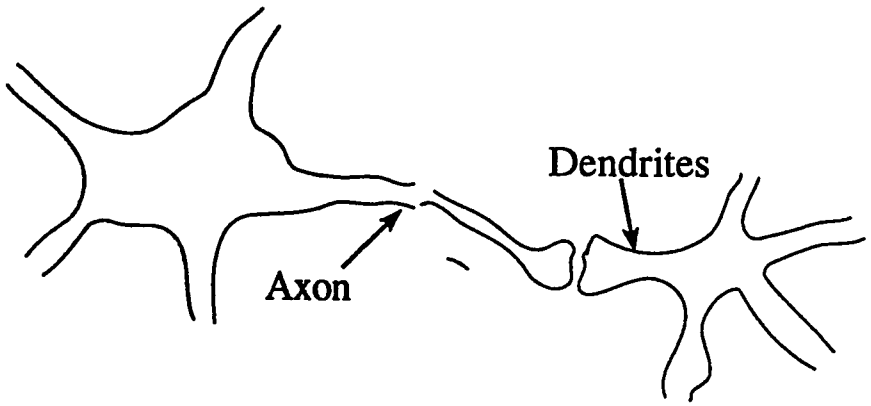

Figure 2.19: Biological neuron

each neuron. Each input is applied over a separate link as shown in Fig. 2.20. A weight is associated with each link. Each input is multiplied by the weight of the corresponding link through which it is applied. All the weighted inputs are then algebraically summed to determine the activation level of the neuron. A model that implements this idea is shown in Fig. 2.20. The different inputs $X_1, X_2, \ldots, X_n$ are applied to one link each. These are multiplied by the link weight and finally algebraically summed up.

Despite the diversity of network paradigms, nearly all are based on this configuration. A set of inputs labeled X_1, X_2,..., X_n is applied to the artificial neuron. Each signal in then multiplied by an associated weight w_1, w_2,... w_n. Finally it is applied to the summation block. The summation block algebraically adds up all the inputs and sends the resultant output which is denoted as $\sum$. In vector notation if X denotes a vector whose i^{th} component X_i and W is a weight vector whose i^{th}

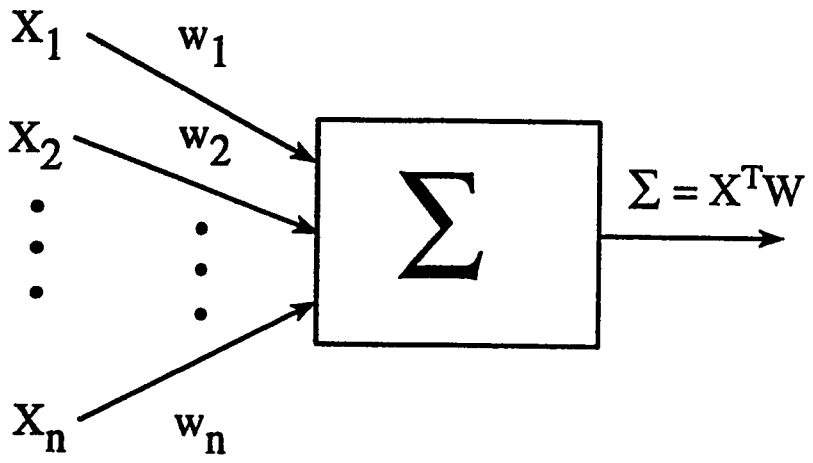

Figure 2.20: Artificial neuron

component is w_i, then, the resultant net can be expressed as

$$\Sigma = X^T W \tag{2.93}$$

2.7.2 Activation function

The signal Σ is usually further processed by an activation function f as shown in Fig.2.21 to produce the neuron's output signal Y. Generally the activation function used is the so-called " squashing function " expressed mathematically as

$$Y = F(\Sigma) \tag{2.94}$$

$$\text{where} \quad F(\Sigma) = \frac{1}{1 + e^{-\Sigma}} \tag{2.95}$$

Fig.2.22 depicts the sigmoidal logistic function. Another nonlinear activation

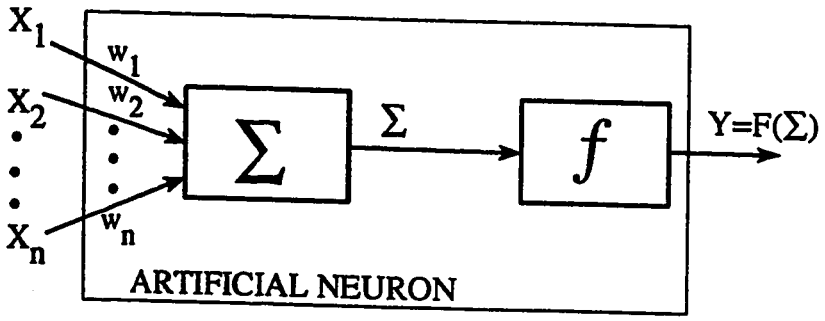

Figure 2.21: Artificial neuron with activation function

function which is commonly used is the hyperbolic tangent. It is shown in Fig.2.23. Mathematically it is expressed as

$$\begin{aligned} F(\Sigma) &= tanh(\Sigma) \\ &= \frac{1-e^{-\Sigma}}{1+e^{-\Sigma}} \end{aligned} \tag{2.96}$$

2.7.3 Single layered network

The power of neural computation comes from connecting the neurons into networks. The simplest network consists of a group of neurons arranged in a layer as shown in Fig.2.24. Neurons present in the same layer are not connected with each other. The circular nodes on the extreme left in Fig. 2.24 serve only to distribute the input. They perform no computation and hence they are also referred to as the zeroth layer. The set of inputs X has each of it's element connected to each neuron through a link each of which has a weight associated with it. Each neuron simply outputs the

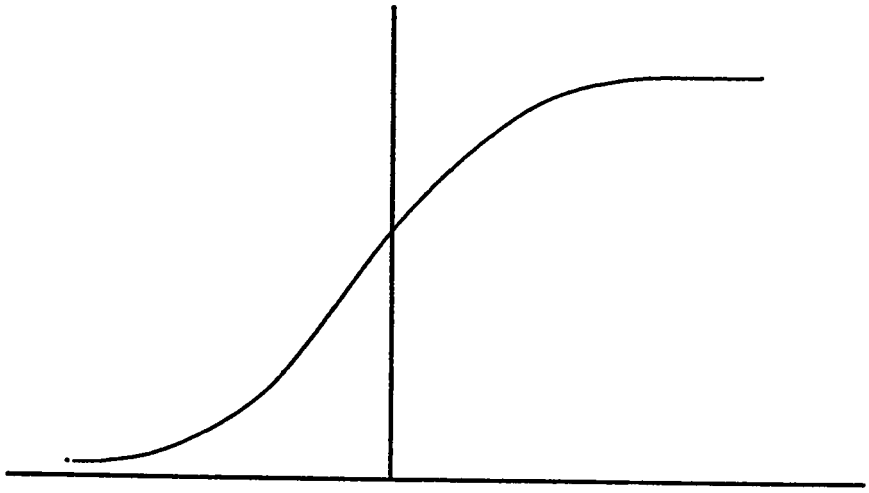

Figure 2.22: Sigmoidal logistic function

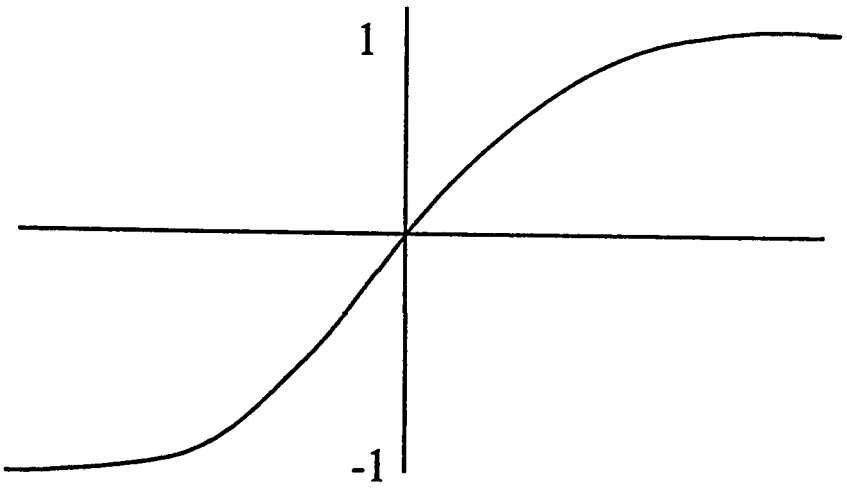

Figure 2.23: Hyperbolic tangent function

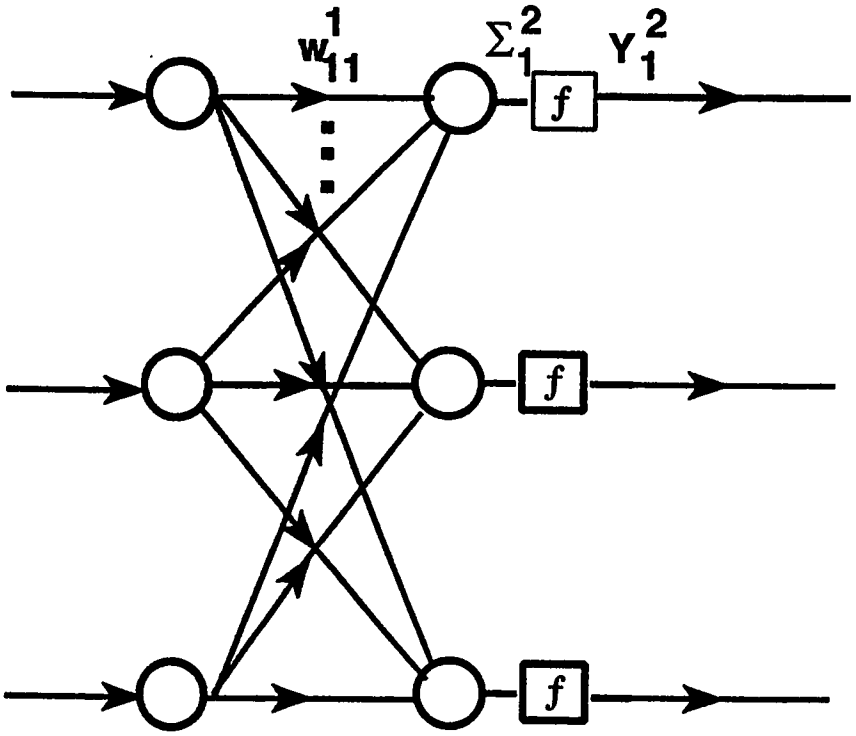

Figure 2.24: Single-layer neural network

algebraic weighted sum of the inputs to the network, acted upon by the activation function. Actual networks may also have many of the connections deleted.

2.7.4 Multilayer artificial neural networks

Greater computational capabilities are offered by large, more complex so-called multilayered networks as shown in Fig.2.25. Each neuron in a layer is completely connected with all the neurons in the next layer. Neurons in the same layer are not connected. This is the feedforward neural network architecture. Although networks

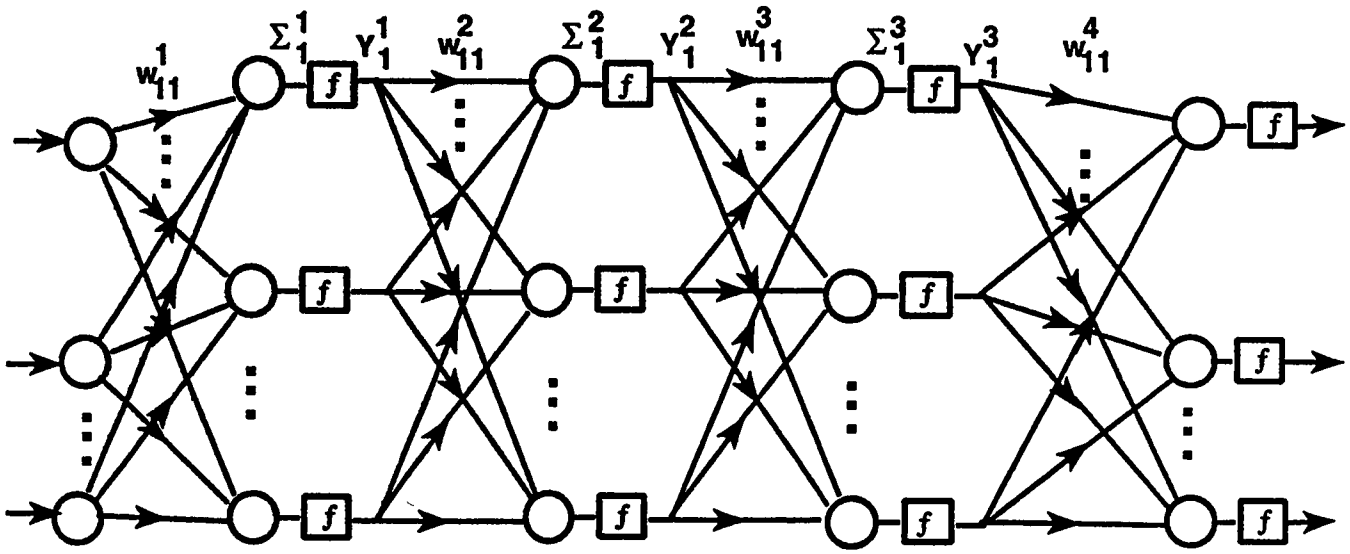

Figure 2.25: Multilayered neural network

have been constructed in every imaginable configuration, arranging neurons in layers mimics the layered structure of certain portions of the brain. Multilayered neural networks have been proven to have capabilities beyond those of single layer. But the nonlinear activation functions are vital to the expansion of the network's capabilities beyond that of the single-layer network since without these functions multilayered networks provide no advantage in flexibility over a single layered network [30].

Chapter 3

PROBLEM DEFINITION AND SOLUTION METHODOLOGY

3.1 Introduction

This chapter presents the problem definition and a solution methodology. We start with transforming the equations of motion presented in Chapter 2 into dimensionless form. This is done to make the study more general. The selection of trajectories and their constraints are discussed in Sec. 3.3. The problem definition is given in Sec. 3.4., Sec. 3.5 presents a general solution methodology, and discusses the proposed control laws.

3.2 The dimensionless system of equations

The equation of motion (Eqs. 2.24-2.26 and Eqs. 2.33-2.35) presented in Chapter 2 represents a general flight vehicle. In the present work, we are mainly concerned with the overall flight trajectories of TAV's. For simplification of the analysis we make the assumption of a non-rotating earth and of flight in the equatorial plane. (ie. $\omega = 0$ and $\sigma = 0$).It should be noted that ω is small hence the term $\omega^2 r$, which represents transport acceleration can be neglected. The term $2\omega V$ has an important effect in a high-speed,long range flight. However, in the present study we can neglect it since our objective is to do an overall analysis. It can be considered in a more specific problem in future studies. If we make the above assumptions the equation Eq. 2.24, Eqs. 2.26-2.33 and Eqs. 2.35-2.35 reduces to

$$m\frac{dV}{dt} = T_t - D_t - mg\sin\gamma \tag{3.1}$$

$$mV\frac{d\gamma}{dt} = L_t - mg\cos\gamma + \frac{mV^2}{r}\cos\gamma \tag{3.2}$$

Thus the equation of motion and all other relevant equations are given as

$$\frac{dr}{dt} = V\sin\gamma \tag{3.3}$$

$$\frac{d\rho}{dt} = -\rho\beta V\sin\gamma \tag{3.4}$$

$$\frac{dV}{dt} = \frac{T_t - D_t}{m} - g\sin\gamma \tag{3.5}$$

where $D_t = D_a + D_r$ and $T_t = T_n + D_r$

$$V\frac{d\gamma}{dt} = \frac{L_t}{m} - g\cos\gamma + \frac{V^2}{r}\cos\gamma \tag{3.6}$$

where $L_t = L_a + L_n$

$$\frac{d\theta}{dt} = \frac{V\cos\gamma}{r} \tag{3.7}$$

$$\frac{dm}{dt} = -\frac{C}{g_o}T_t = -\frac{T_t}{I_{sp}g_o} \tag{3.8}$$

$$\frac{dQ}{dt} = C_Q\rho^{0.5}V^3 \tag{3.9}$$

The dimensionless state variables are defined as.

The dimensionless position,

$$\hat{r} = \frac{r}{r_o} \tag{3.10}$$

where r_o is the earth radius at the equator, and r is the position of the vehicle with respect to the earth center.

The dimensionless density,

$$\eta = 1000 C_{La}^{*} \frac{\rho}{\rho_o} \tag{3.11}$$

where ρ_o is the air density at the sea level, and ρ is the density at r.

The dimensionless velocity,

$$u = \frac{V}{V_c} \tag{3.12}$$

where $V_c = \sqrt{g_o r_o}$ is the orbital velocity at the equatorial earth surface.

The dimensionless path angle,

$$\hat{\gamma} = \frac{\gamma}{\gamma_r} \tag{3.13}$$

where γ_r is any chosen reference. The dimensionless longitude,

$$\hat{\theta} = \frac{\theta}{\theta_r} \tag{3.14}$$

where θ_r is any chosen reference longitude.

The dimensionless mass ,

$$\mu = \frac{m}{m_o} \tag{3.15}$$

where m_o is the mass of the vehicle at the time of takeoff at earth surface and at Mach zero(M = 0).

The dimensionless time

$$\hat{t} = \frac{t}{t^*} \tag{3.16}$$

where $t^* = \sqrt{\frac{r_o}{g_o}}$ sec. Note that t^* is the time taken to reach circular orbit speed at constant acceleration g_o.

We also define the

$$C = \frac{1}{I_{sp}} \tag{3.17}$$

where C is the specific fuel consumption.

Using the above definitions, Eq. (3.3) to Eq. (3.9) can be written in the dimensionless form as

$$\frac{d\hat{r}}{d\hat{t}} = u \sin\gamma \tag{3.18}$$

$$\frac{d\eta}{d\hat{t}} = -\beta r_o \eta u \sin\gamma \tag{3.19}$$

$$\frac{du}{d\hat{t}} = \left[\frac{\tau_n}{\mu} - C_4\left(\frac{r_o}{2C_1C_2}\right)(f_a)\left(\frac{\eta u^2}{\mu}\right) - \frac{sin\gamma}{\hat{r}^2}\right] \tag{3.20}$$

$$\frac{d\hat{\gamma}}{d\hat{t}} = \left\{C_4\left(\frac{r_o}{2C_1C_2}\right)(\lambda_l)\left(\frac{\eta u}{\mu}\right) - \left(\frac{1}{\hat{r}^2 u}\cos\gamma\right) + \left(\frac{u}{\hat{r}}\cos\gamma\right)\right\}/\gamma_{re} \tag{3.21}$$

$$\frac{d\hat{\theta}}{d\hat{t}} = \left(\frac{u}{\hat{r}}\cos\gamma\right)/\theta_{re} \tag{3.22}$$

$$\frac{d\mu}{d\hat{t}} = -t_c \frac{\tau_t}{I_{sp}} \tag{3.23}$$

$$\frac{d\hat{Q}}{d\hat{t}} = \frac{\left(C_Q C_5 {V_C}^2 r_o \eta^{0.5} u^3\right)}{Q_{re}} \tag{3.24}$$

where λ_t the dimensionless aerodynamic control, τ_t is the dimensionless thrust control, and f_a is given by

$$f_a \equiv \frac{C_{Da}}{C_{La}^{=}} = \frac{1 + {\lambda_a}^2}{2E^*} \tag{3.25}$$

and

$C_1 =$ 1000

$C_2 =$ characteristic length of the vehicle

$C_4 = (\rho S c_2)/m_o$

$C_5 = \sqrt{\rho_o/(C_1 C_{La}^{=})}$

3.3 Trajectories and their constraints

The selection of the trajectories is affected to a large extent by the constraints. The constraints could be due to the physical limitations of the vehicle or they might be mission dependent(mission constraints). As an example, the performance of RAM-jet and SCRAM-jet engines improves with increase in flight dynamic pressure. This is due to the increase in engine mass flow and the improvement in combustion characteristics at higher static pressure. But there are structural limitations that restrict

the maximum static pressure in the combustion chamber. On the other hand the combustion process sets a lower limit on the static pressure, below which combustion cannot be sustained [24]. Hence the dynamic pressure forms an important physical constraint.

Similarly examples for mission constraints are the final height that is to be reached, the velocity of the vehicle, rate of climb etc.In the present study we have given consideration to most of the important constraints. These constraints have been suggested in various works [25], [31], [3], [22], [32], [33], [34] and are presented below.

$$0 \leq \tau_t = \frac{T_t}{W_o} \leq 5$$

$$0 \leq \tau_n = \frac{T_n}{W_o} \leq 1.5$$

$$0 \leq \frac{T_t - D_t}{D_t} \leq 0.7$$

$$\frac{T_n}{D_a}(t) \geq 3$$

$$500 \leq I_{sp}(M) \leq 3000 sec.$$

$$-1.0 \leq \lambda_a \leq 1.0$$

$$-1.1 \leq \lambda_t \leq 1.1$$

$$0.05 \leq C_{La}^{*} \leq 0.1$$

$$0.001 \leq C_{D_a} \leq 0.04$$

The above design values are for an angle of attack in the range of 0.5° to 3.0°. For the atmospheric data ρ, T', and P, we can use the data given in [18] (US standard atmosphere). The data is taken for the trajectories in the range $20km \leq h \leq 65km$. The earth radius is given as $r_o = 6375400m$. This leads to the following trajectory constraints:

The final state and time constraints:

$$1 \leq u_f \leq 1.414$$

$$60 \leq h_f \leq 75km$$

$$0.5 \leq \theta_f \leq 1.0\, rad$$

$$0.25 \leq \mu_f \leq 0.43$$

$$500 \leq t_f \leq 1500sec$$

The functional constraints:

$$u_i \leq u(t) \leq 1.414$$

$$h_i \leq h(t) \leq 75km$$

$$\gamma_i \leq \gamma(t) \leq 0.1rad$$

$$\theta_i \leq \theta(t) \leq 0.1rad$$

$$0.25 \leq \mu(t) \leq (\mu_i = .94)$$

$$0.0 \leq \left(rc(t) = \frac{dr}{dt}\right) \leq 200m/sec$$

$$0.02 \leq q(t) \leq 1.5atm.$$

$$0 \leq a(t)/g_o \leq 2.0$$

$$0.1 \leq (D_r/D_a)(t) \leq 300$$

$$500 \leq \left(\frac{m}{C_{D_a}S}\right)(t) \leq 70000\,Kg/m^2$$

$$100 \leq \left(\frac{m}{C_{D_t}S}\right)(t) \leq 15000\,Kg/m^2$$

$$100 \leq \left(\frac{m}{C_{L_t} S}\right)(t) \leq 15000\, Kg/m^2$$

$$0 \leq \left(\frac{T_t - D_t}{D_t}\right)(t) \leq 0.7$$

$$0 \leq \left(\frac{L_r}{L_a}\right)(t) \leq (\sin 5.7 = 0.1)$$

$$\frac{T_n}{D_a(t)} \geq 3$$

The functional objective constraint:

$$\dot{Q}(t) \leq 0.5\, KW/cm^2$$

and the final objective constraint:

$$Q_f \leq 500\, kJ/cm^2$$

In the above equations we have summarized the trajectory constraints that are essential. We have included most of the constraints that affect the design of the vehicle critically.

3.4 Problem definition

The problem at hand is defined as follows:

Minimize the heat load

$$J = Q(\bar{x}, t) \tag{3.26}$$

Subject to the constraints

$$C_i(\bar{x}, t) \leq 0 \qquad i = 1 \ldots m \tag{3.27}$$

where, $\bar{x}$ is the state vector, Q is the heat load, given by the equation (3.24) and $C_i's$ are the constraints given in the previous section, and t is the time. The form of control laws used to transform the problem into a finite dimensional optimization problem are discussed in the next section.

It should be noted that the heat load Q is not an explicit function of the controls τ and λ, see Eq. 3.24. Whereas, it is an explicit function of the density η and the velocity u. These in turn are functions of the controls τ and λ. Thus Q is implicitly a function of the controls. To evaluate the objective value and the constraints a complete simulation (integration) of the system of equations 3.18–3.24 for given controls is needed.

3.5 Solution methodology

3.5.1 The controls

As discussed previously, the objective of this study is to transfer the TAV from a specified initial state to a final state, while minimizing the heat load. This objective is achieved through the two controls, namely thrust control τ_t and aerodynamic control λ_t. The controls τ_t and λ_t are yet to be specified.

In this study we have considered two different forms of control laws.

Polynomial controller

The first is a feedback control law which is function of velocity and density [14], [15],[35] expressed as.

$$\tau_t = a_1 + a_2\, u^2 + a_3\, \eta \tag{3.28}$$

$$\lambda_t = b_1 + b_2\, u^2 + b_3\, \eta \tag{3.29}$$

where $a_i, b_i, i = 1, \ldots 3$ are the parameters which specify the functional relationship. The states u and η have been chosen for feedback since they are most representative of the TAV's behavior.

Neural controller

In the second case a two layered feedforward neural network is used as a controller. The form of the neural network used is shown in the figure 3.1, [30], [4]. The two inputs to the neural network are u, η and the outputs are the thrust control τ_t and aerodynamic control λ_t. The weight matrices $[W]$ and $[X]$ define the outputs of the neural network. Thus the problem becomes of a parametric nature where $[W], [X]$ are to be determined such that the constraints are satisfied and the objective is achieved.

Mathematically the controls using the neural controller are expressed as,

output at the first layer

$$\left\{ \begin{array}{c} O_1 \\ O_2 \\ O_3 \end{array} \right\} = f1(\{I\}[W])^T = \left\{ \begin{array}{c} f1(uw_{11} + \rho w_{12}) \\ f1(uw_{12} + \rho w_{22}) \\ f1(uw_{13} + \rho w_{23}) \end{array} \right\}$$

and thus the controls become

$$\left\{ \begin{array}{c} \tau_t \\ \lambda_t \end{array} \right\} = f2(\{O\}^T[X])^T = \left\{ \begin{array}{c} f2(O_1X_{11} + O_2X_{21} + O_3X_31) \\ f2(O_1X_{12} + O_2X_{22} + O_3X_32) \end{array} \right\}$$

It should be noted that in the hidden layer a tangent hyperbolic function (f1 in Fig.3.1) was used as a activation function and in the output layer a sigmoidal function (f2) was used.

In recent years a lot of research activity has been centered around the neural

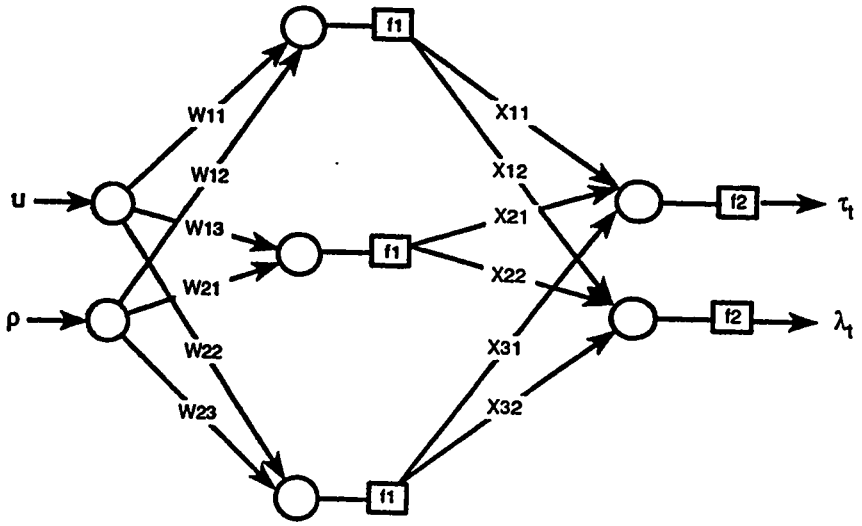

Figure 3.1: The neural controller for aerodynamic and thrust controls.

networks. They are being applied in many areas of engineering and sciences. Neural networks have a remarkable learning ability, they can be viewed as a class of functional representations. Thus they are considered to be dense in the space of continuous functions and hence can be used for representing any general nonlinear function. In fact it has been shown by Cybenko[36] and Hornik et. al. [37]that any continuous mapping over a compact domain can be approximated as accurately as necessary by a feedforward neural network, even with only one hidden layer. This implies that given any $\epsilon > 0$ a neural network NN with sufficiently large number of nodes can be determined such that

$$||f(x) - NN(x)|| < \epsilon \qquad \text{for all } x \in D$$

where f is the function to be approximated, NN the neural network and D is

a compact domain of a finite dimensional normed vector space. This provides the basis for using the neural network as a controller for the TAV.

After the above definitions of controls we write the equations for lift, drag thrust etc., as follows.

The thrust,

$$T_n = T_t - D_r \tag{3.30}$$

where $T_t = m_o g_o \tau_t$ and $T_n = m_o g_o \tau_n$.

Introducing,

$$D_r = (d_1 + d_2 u^2)\tau_t \tag{3.31}$$

where d_1 and d_2 are design coefficients for ram drag, to be calculated during the computational study. The value of $(d_1 + d_2 u^2) < 1.0$ for positive net thrust.

The lift,

$$\lambda_t = \lambda_a + \lambda_r \tag{3.32}$$

where

$$\lambda_a = \frac{C_{La}}{C_{La}^*} \tag{3.33}$$

and we define $\lambda_r = d_3 \lambda_a$, where d_3 is a design parameter to be computed.

From the above we can write,

$$L_a = \frac{1}{2}\rho V^2 S C_{La} = qSC^{\alpha}_{La}\lambda_a \tag{3.34}$$

$$L_r = \frac{1}{2}\rho V^2 S C_{Lr} = d_3 qSC^{\alpha}_{La}\lambda_t \tag{3.35}$$

3.5.2 The optimization procedure

Once the control laws are defined the problem reduces to finding the parameters a_i, b_i (for the first type) or the matrices $[W], [X]$ (for the second type). The parameters are to be found such that the objective is achieved while satisfying the constraints. The above problem is solved by doing an extensive simulation and optimization study. The numerical computations are performed using a simulation and optimization package [38]. The computations consists of two distinct phases namely simulation and optimization. The package uses the IMSL[39] routines in the simulator and the " Feasible Sequential Quadratic Programming (FSQP) " [40] for optimization.

Simulation

The simulation in this study consists of solving the initial value problem (IVP). Given the values of the dependent variable y at time $t = 0$, and the controls the values for $t > 0$ are computed. We have made use of the IMSL routine DIVPAG, [39]. This routine solves an IVP for ordinary differential equations using either

Adams-Moulton or Gear method. We have used Gear method since the system of equation in this study are stiff.

Optimization

Optimization was performed using the optimization software FSQP [40]. It consists of a set of FORTRAN subroutines for the minimization of smooth objective functions subject to nonlinear equality and inequality constraints, linear equality and inequality constraints, and simple bounds on the variables. If the initial guess provided by the user is infeasible for the constraints, FSQP first generates a point satisfying all these constraints. Subsequently, the iterates generated by FSQP all satisfy the constraints.

The algorithm is based on a sequential quadratic programming (SQP) iteration modified so as to generate feasible iterates. The merit function is the objective function. An Arminjo–type line search is used to generate an initial feasible point when required. After obtaining feasibility, either (i) an Arminjo–type line search may be used, yielding monotone decrease of the objective function at each iteration, or (ii) a nonmonotone line search may be selected, forcing a decrease of the objective function within at most four iterations.

Figure 3.2 shows the flow chart of the program that was used for the study. The parameters for the optimization are either a_i, b_i or $[W], [X]$. An initial guess is to be provided by the user to start the optimization process. We assigned random values

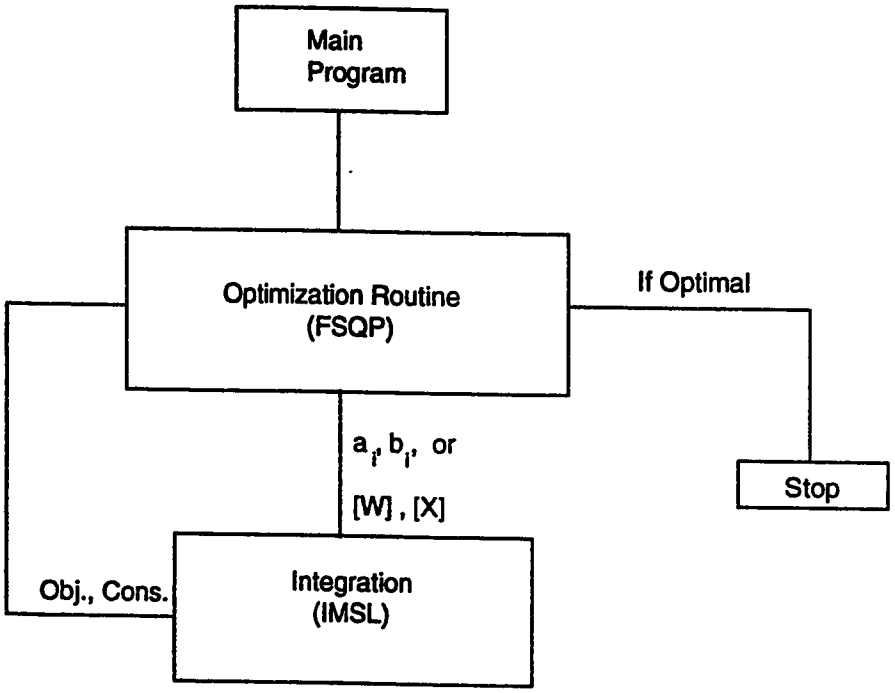

Figure 3.2: Flow chart of program used for the study.

to the parameters at the start. Most of the times these values produce trajectories which do not satisfy the constraints. In this case the optimization program searches for a feasible point and then proceeds from this newly generated point.

The parameters generated by the optimization program are fed to the simulation package which integrates the nonlinear differential equations. It also computes all the constraint values. The objective and the constraints are then fed back to the optimization routines, based on which the search proceeds.

Chapter 4

OPTIMIZATION AND SIMULATION RESULTS

4.1 Introduction

In this chapter the optimization and simulation results using the methodology discussed in chapter 3. are presented. In section 4.2. are presented the parameters. constants and the initial conditions used for this study. The data has been collected from different references. In section 4.3. the correlations of I_{sp} as a function of Mach number are presented. Section 4.4 presents the simulation results for the four cases. CASE1a-b to CASE4a-b. The CASE1a, is same as CASE 1, presented in [10],[11]. It is presented for both validation and comparison.

4.2 Design parameters of the vehicle and initial conditions

To perform a simulation and optimization study we need to specify certain vehicle design parameters and the initial conditions. The design parameters are taken from [32], [33], [34], [41].

4.2.1 Vehicle model parameters

The following weight and sizes of the vehicle are considered.

$$445000 \leq W_o \leq 4450000.N$$

$$20 \leq length - C_3 \leq 60m$$

$$10 \leq span \leq 30m$$

$$0.025 \leq (\rho_o S C_3 / m_o) \leq 0.15$$

($(\rho_o S C_3 / m_o)$ is the mass ration parameter for longitudinal stability.)

4.2.2 Initial conditions

The initial condition are given in this section, the are same as in [10], [11]. They are as follows:

$$\begin{aligned} r_i &= 6395400km \quad \text{or} \quad 6385400km \\ \rho_i &= 0.082kg/m^3 \\ u_i &= 0.2 \\ \gamma_i &= 0.175rad \\ \theta_i &= 0.0rad \\ \mu_i &= 0.94 \\ Q_i &= 5.0kJ/cm^2 \end{aligned} \tag{4.1}$$

4.3 The Specific Impulse I_{sp}

In this work we have considered two different cases. namely that of constant I_{sp} and the other of variable I_{sp}. In general the I_{sp} is dependent primarily on the Mach Number and the air to fuel ratio. and slightly on thrust setting and altitude. For the analysis of optimal trajectories, I_{sp} should be modeled on the basis of engine performance characteristic. In this work we have modeled I_{sp} as a function of Mach Number($I_{sp}(M)$) using the engine data given in [22]. The Fig.4.1 shows the plot for the data, the plot is of I_sp vs Mach number, for different specific fuel ratios. We have done a polynomial fit to the data.

The equation obtained is given as,

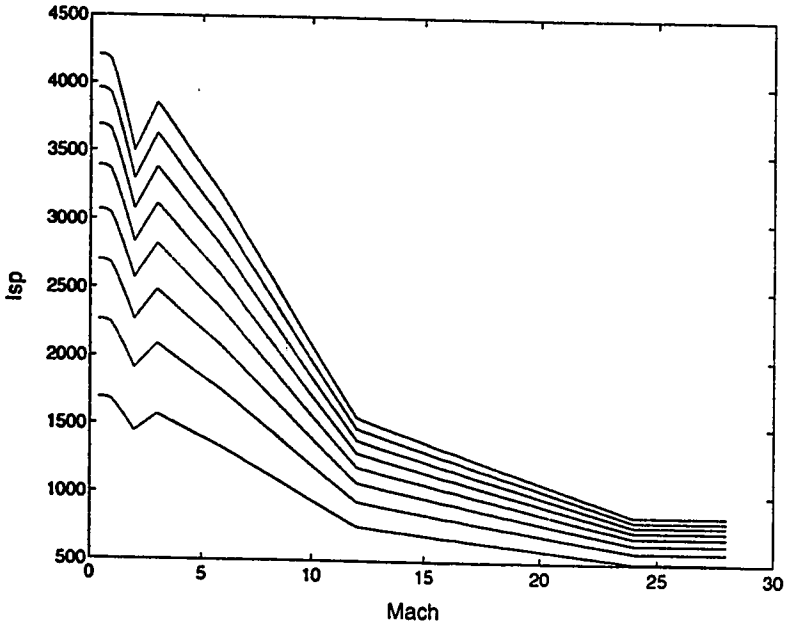

Figure 4.1: Specific impulse vs Mach number for different specific fuel ratios.

$$I_{sp}(M) = 7.41E-4M^6 - 5.45E-2M^5 + 1.48M^4 \qquad (4.2)$$
$$-18.1M^3 + 97.6M^2 - 322.2M + 3059.23$$

4.4 Optimization and Simulation results

Extensive optimization and simulation study was performed using the methodology presented in Chapter 3. For the optimization procedure the objective was to minimize the heat load (Eq. 3.25) while satisfying the constraints. We have presented results for four cases. we differentiate between the cases based on the initial and final conditions, and/or the specific Impulse used for the Engine modeled. The Figure 4.2 shows the classification of the different cases. Each case is further divided into two sub-cases for example CASE 1 is further divided as CASE1-a and CASE1-b. CASE1-a uses the polynomial type controller and CASE1-b uses the neural controllers. Similarly we have CASE2-a. CASE2-b. CASE3-a. CASE3-b. CASE4-a. and CASE4-b. Both cases *a* and *b* use the same initial conditions and parameter values.

4.4.1 Results validation

To validate the results obtained in this study, a comparison was performed. with the work of Al-Garni[10], Al-Garni et. al[11]. The initial conditions, vehicle design

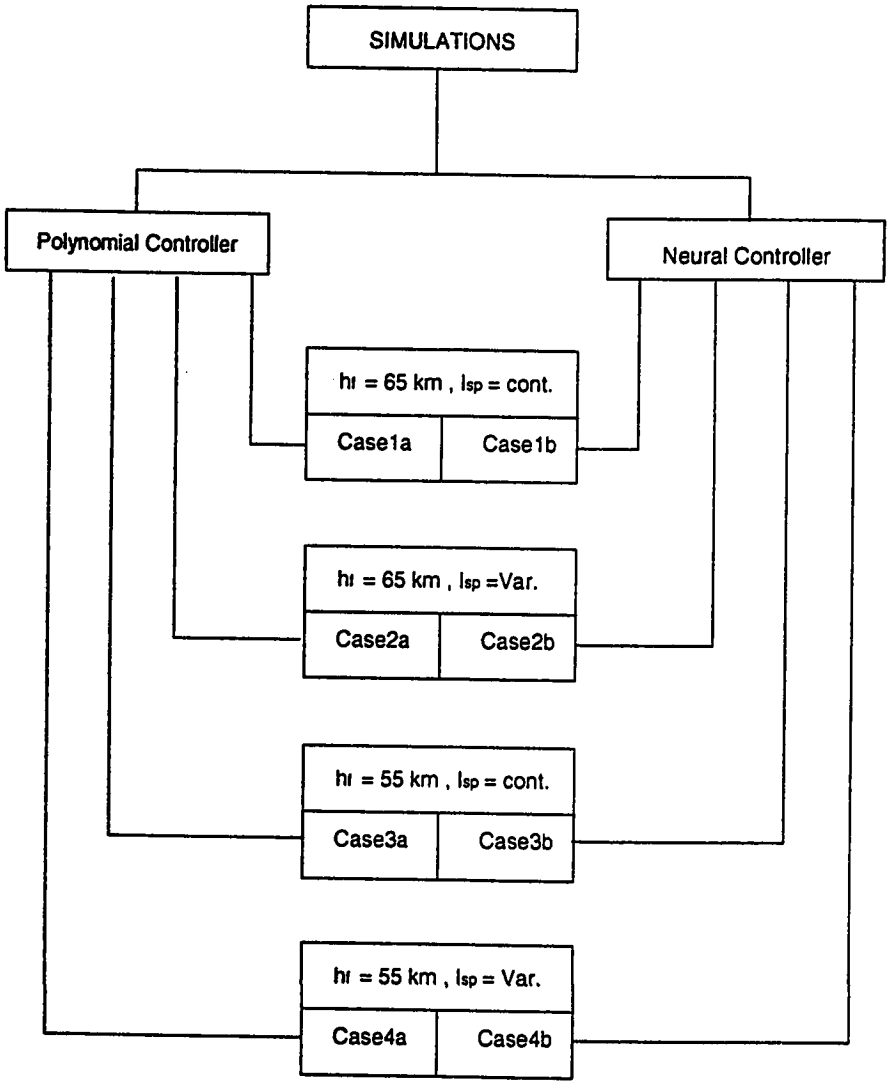

Figure 4.2: Overview of the simulation study.

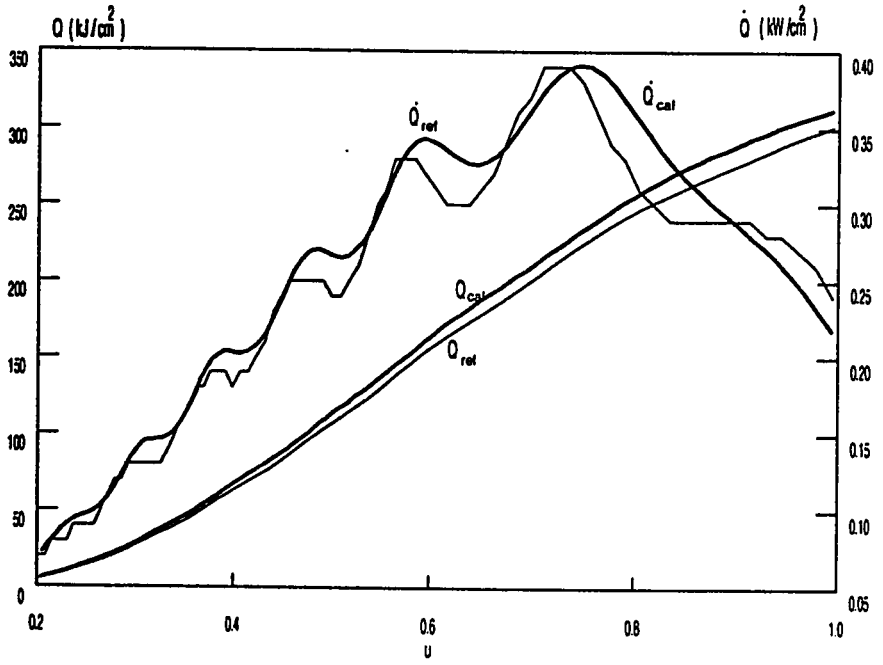

Figure 4.3: Heat rate per unit area and heat load per unit area vs the dimensional speed.

parameters, and constraints are assumed same as those in the study by Al-Garni [10].

In [10] two approaches were adopted, numerical and analytical. The results obtained by these two approaches were then compared. In the present study a comparison of the results obtained is made with both the numerical and analytical approaches of Al-Garni[10]. Figure 4.3 shows a comparison of the heating, the thicker lines are from this study. It can be seen that the results obtained are fairly close. Similarly the results for aerodynamic and thrust controls are shown in Fig. 4.4 and Fig. 4.5 respectively. The results are seen to be very close. Thus, this comparison validates the results obtained by the proposed computational method.

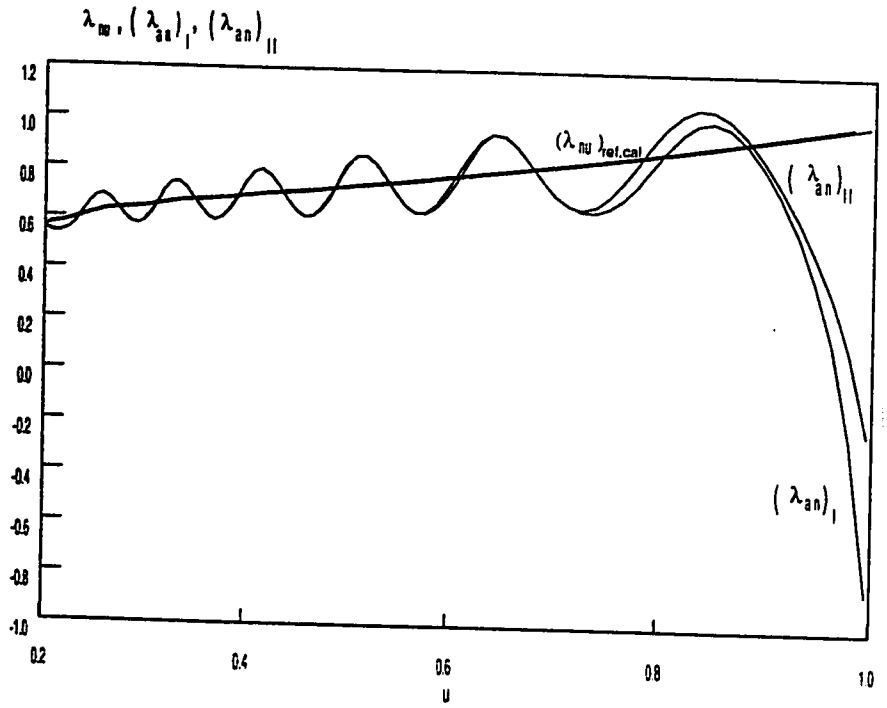

Figure 4.4: Aerodynamic controls vs the dimensionless speed.

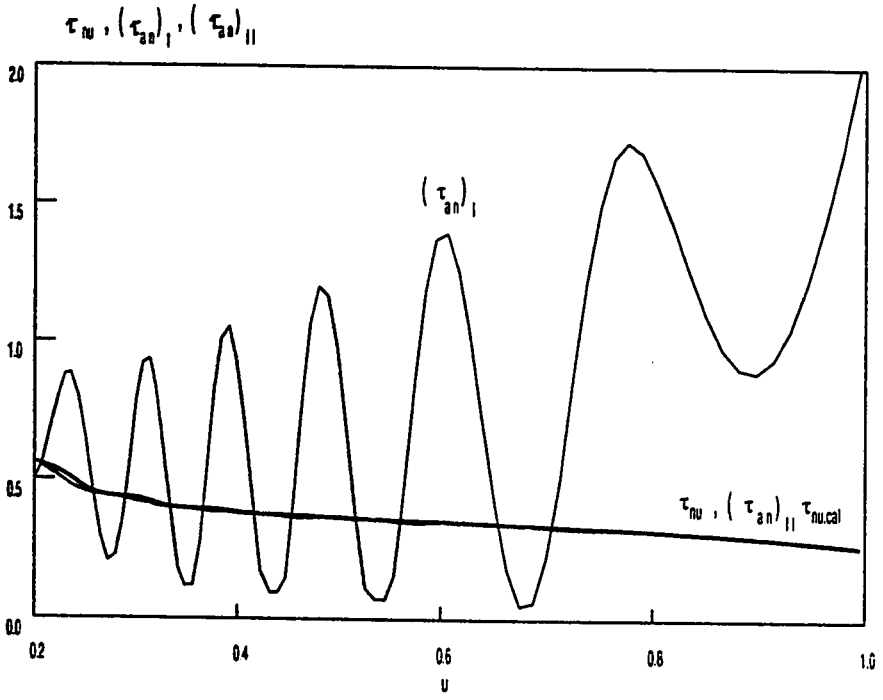

Figure 4.5: Thrust controls vs the dimensionless speed.

4.4.2 CASE 1a-b

CASE 1-a presents the trajectory obtained using the polynomial feed back controller and CASE 1-b uses a neural controller. For both cases trajectories start at an initial altitude of 20 Km and reach a final height of ≈65Km. We used constant specific Impulse I_{sp} value of 2400 for both the cases. It should be noted that CASE 1a is the same as CASE 1 in [10]. The optimized parameter values for the two controllers are given in the Appendix. The results are presented in Fig 4.6 to Fig 4.18.

Figure 4.6.a shows h vs u and Fig 4.6.b shows u vs t. The trajectory shown starts from $t_i = 0$, $h_i \approx 20Km$ and $u_i \approx .2$ and finishes at $t_f \approx 1275sec$. $h_f \approx 70Km$ and $u_f = 1$. The figure shows that the trajectory satisfies the constraints on h, u and t. It is also observed that the trajectory obtained using a neural controller is much smother than the polynomial controller.This is a favorable characteristic that reflects in all the cases presented here.

Figures 4.7.a and 4.7.b show $\dot{\gamma}$ vs u and γ vs u respectively. The plots show that $\dot{\gamma}$ and γ both satisfy the functional constraints.

Figures 4.8.a and 4.8.b show ρ vs u and θ vs u respectively. The plot of ρ shows that the approximation made for the density is reasonable and the values obtained are close to the data in U.S. standard atmosphere. Also ρ is plotted because it is one of the most important factors that affects the heating. The plot of θ vs u shows that the final constraint on θ is satisfied.

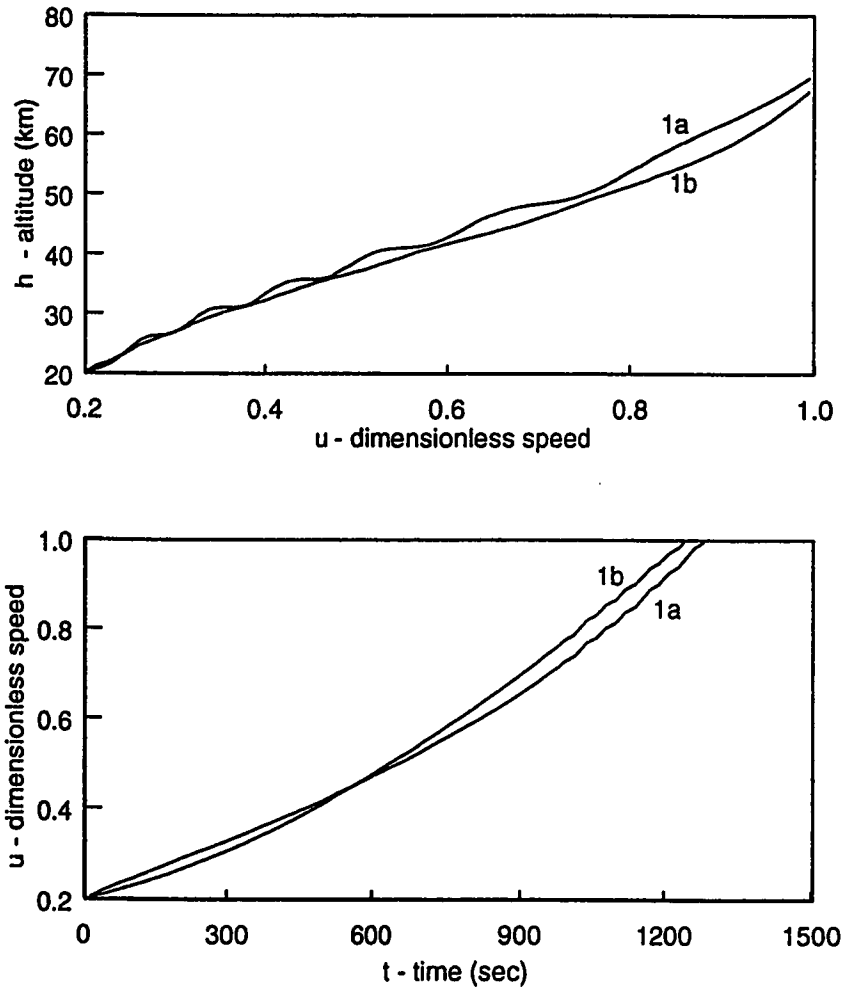

Figure 4.6: (a) h - altitude (km) vs u - dimensionless velocity. (b) u - dimensionless velocity vs t - time (sec).

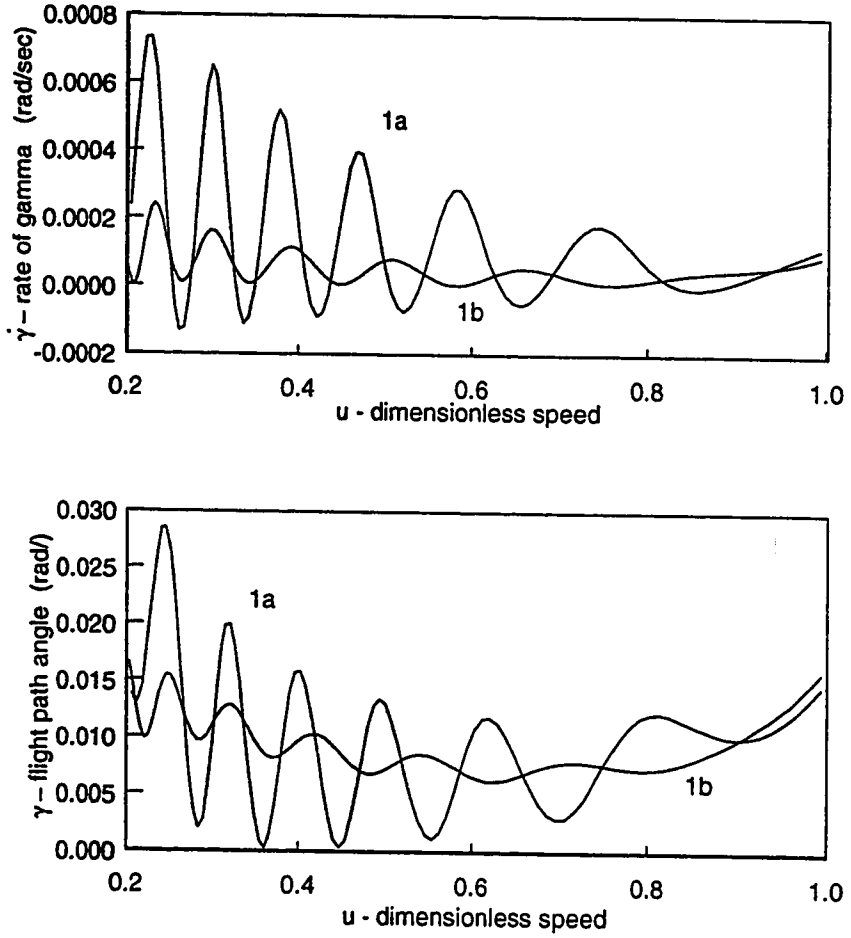

Figure 4.7: (a) $\dot{\gamma}$ - rate of change of flight path angle (rad/sec) vs u - dimensionless velocity. (b) γ - flight path angle (rad) vs u - dimensionless velocity.

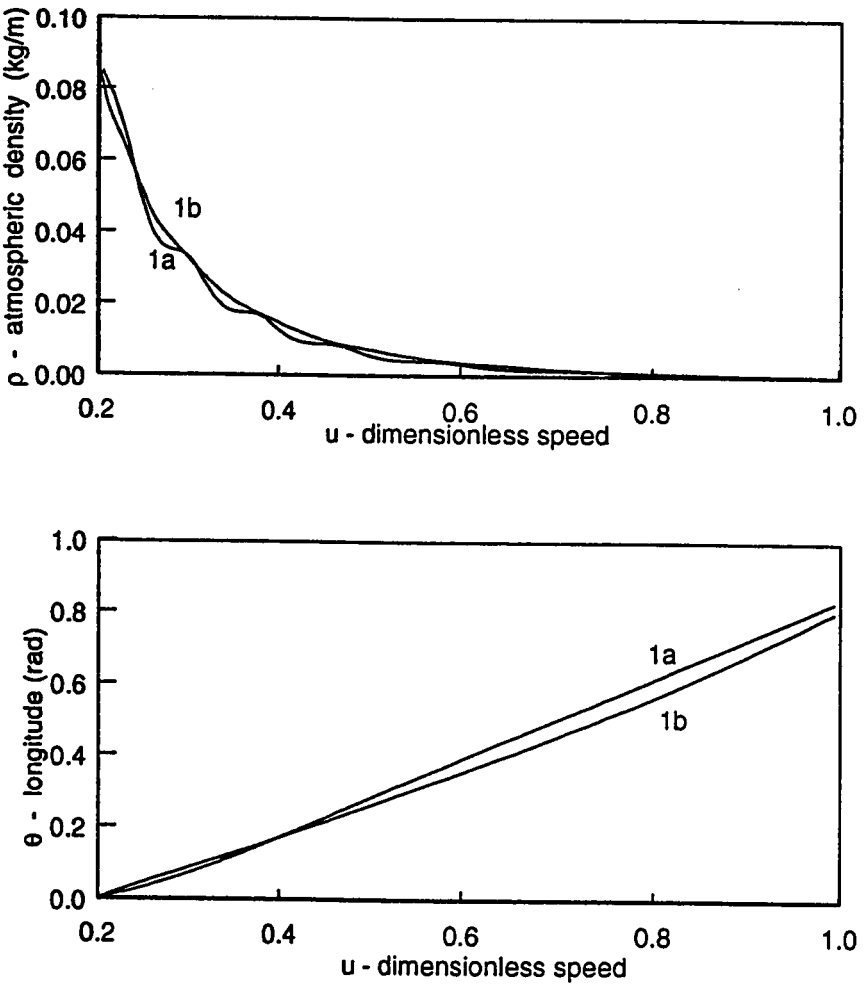

Figure 4.8: (a) ρ - atmospheric density (kg/m^3) vs u - dimensionless velocity. (b) θ - longitude (rad) vs u - dimensionless velocity.

Figures 4.9.a and Fig. 4.9.b show $\dot{Q}$ vs u and Q vs u. Both Q and $\dot{Q}$ satisfy the constraints. It is seen that Q obtained using polynomial controller is $\approx 310 kJ/cm^2$, whereas Q obtained using neural controller is higher and is $\approx 335 kJ/cm^2$. This is due to the fact that the trajectory using neural controller is lower (see Fig. 4.6.a). The above results are promising, since the heat loads are not as high as obtained in [1]. With this kind of heat loads cooling system could most probably be designed.

Figures 4.10.a and 4.10.b show rc vs u and q vs u respectively. It is seen that both rc and q satisfy the constraints. It is also clear from Fig. 4.10.a that the trajectory obtained using a neural controller is smoother. Figure 4.10.b shows that the dynamic pressure is higher for trajectory using neural controller, this is desirable, since higher dynamic pressures are usually related to better engine performance.

Figures 4.11.a and 4.11.b show (a/g_o) vs u and μ vs u respectively. The dimensionless acceleration is within the reasonable limits given in the literature. The dimensionless mass μ is shown in Fig. 4.11.b. it satisfies the final constraints.

Figures 4.12.a and 4.12.b shows the thrust and aerodynamic controls plotted vs u respectively. The controls values are within the specified range. It is interesting to note that the aerodynamic control using the neural controller stays almost constant.

Figures 4.13 to 4.18 shows the drags, thrust, lift, coefficients of lift, and coefficient of drags. All these variables lie within reasonable limits and satisfy the constraints.

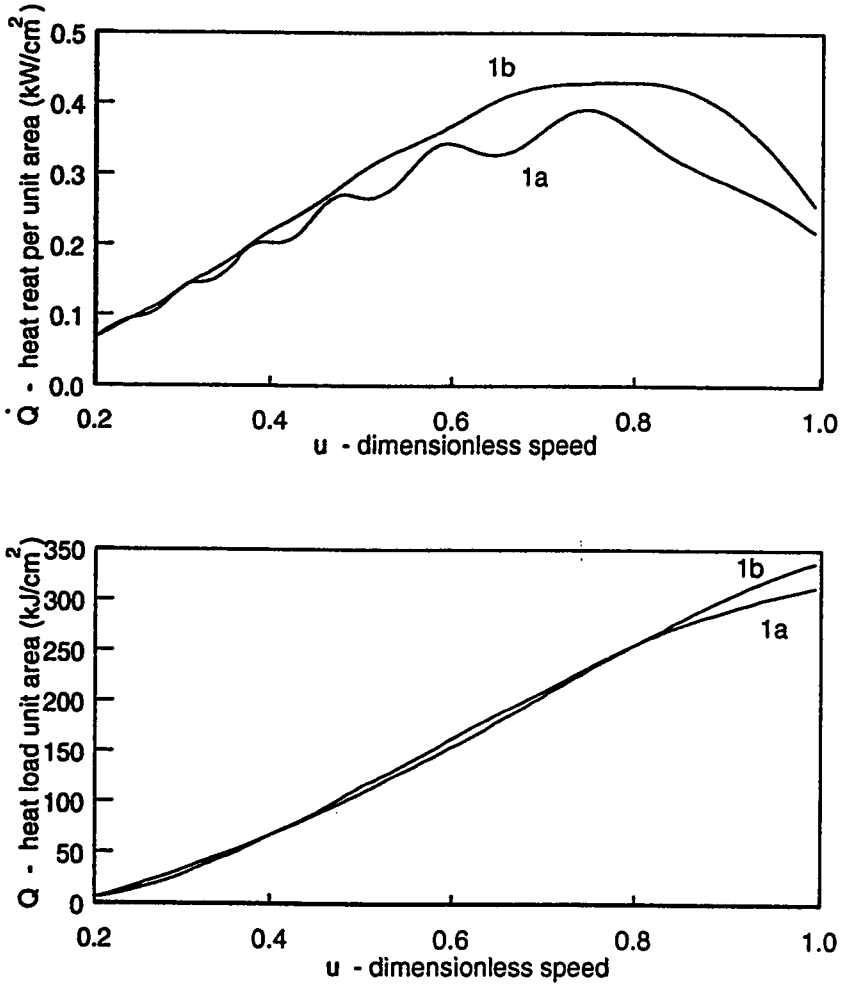

Figure 4.9: (a) $\dot{Q}$ - heat rate per unit area (kW/cm^2) vs u - dimensionless velocity. (b) Q - heat load per unit area (kJ/cm^2) vs u - dimensionless velocity.

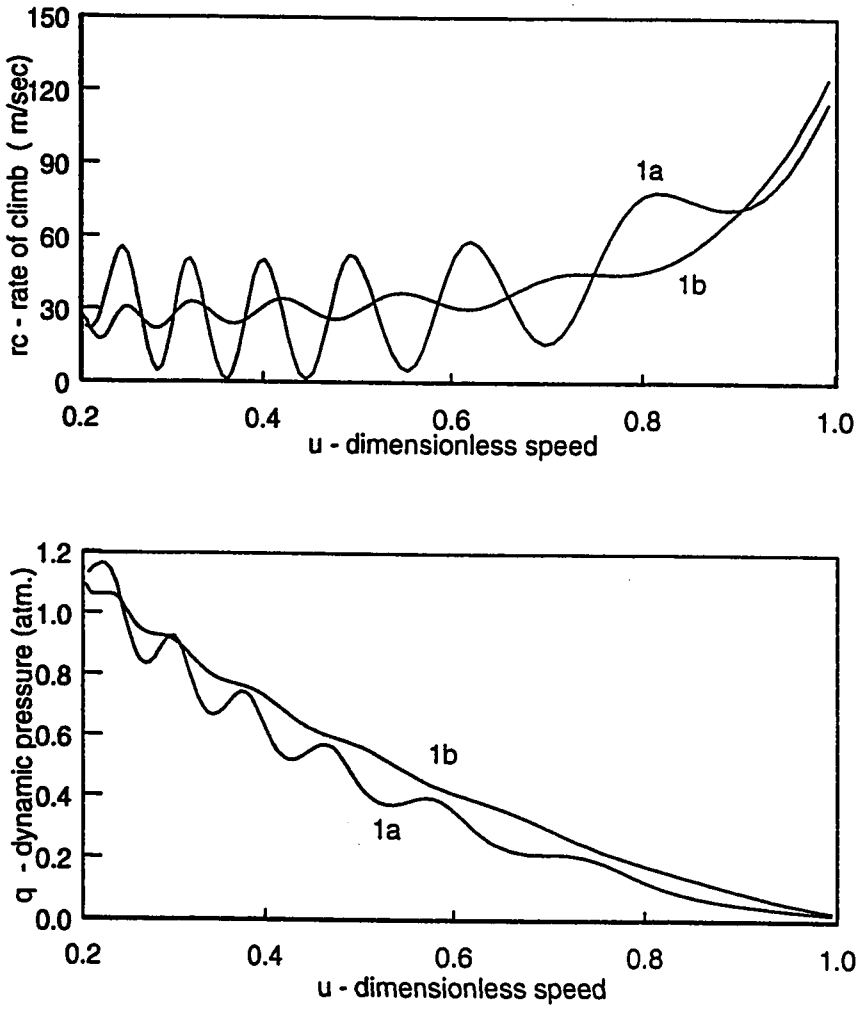

Figure 4.10: (a) rc - rate of climb (m/sec) vs u - dimensionless velocity. (b) q - dynamic pressure $(atm.)$ vs u - dimensionless velocity.

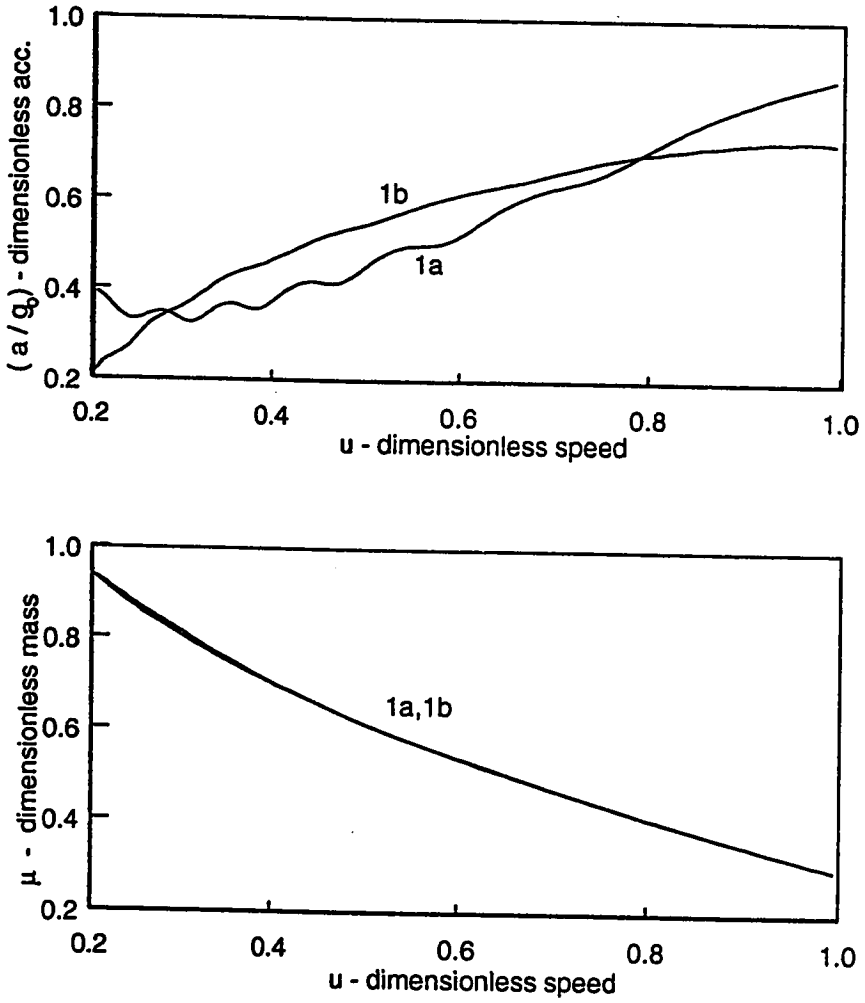

Figure 4.11: (a) (a/g_o) - dimensionless acceleration vs u - dimensionless velocity. (b) μ - dimensionless mass vs u - dimensionless velocity.

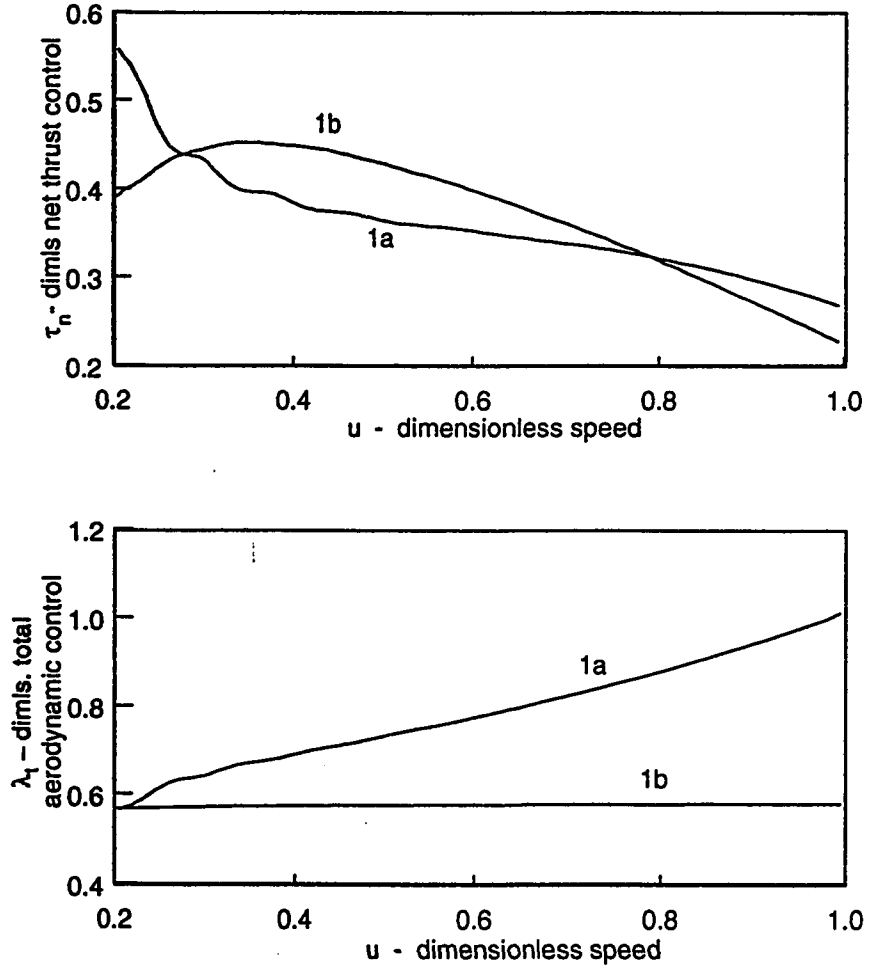

Figure 4.12: (a) τ_n - dimensionless net thrust control vs u - dimensionless velocity. (b) λ_t - dimensionless total aerodynamic control vs u - dimensionless velocity.

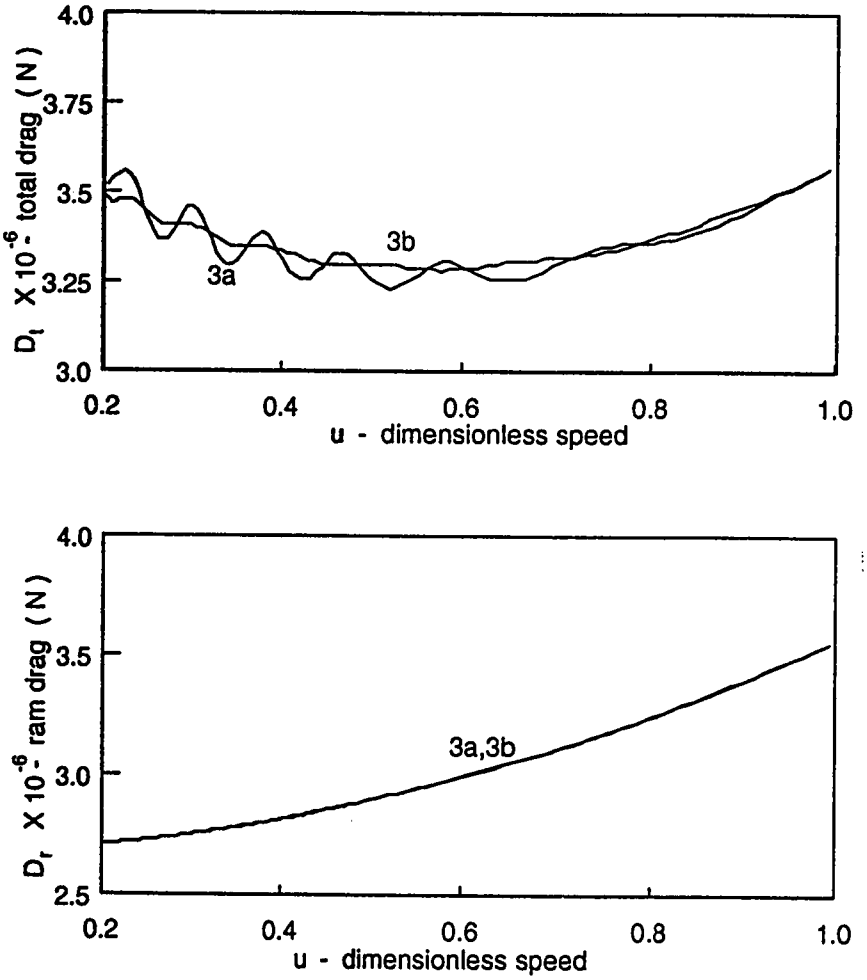

Figure 4.13: (a) D_t - total drag (N) vs u - dimensionless velocity. (b) D_r - ram drag (N) vs u - dimensionless velocity.

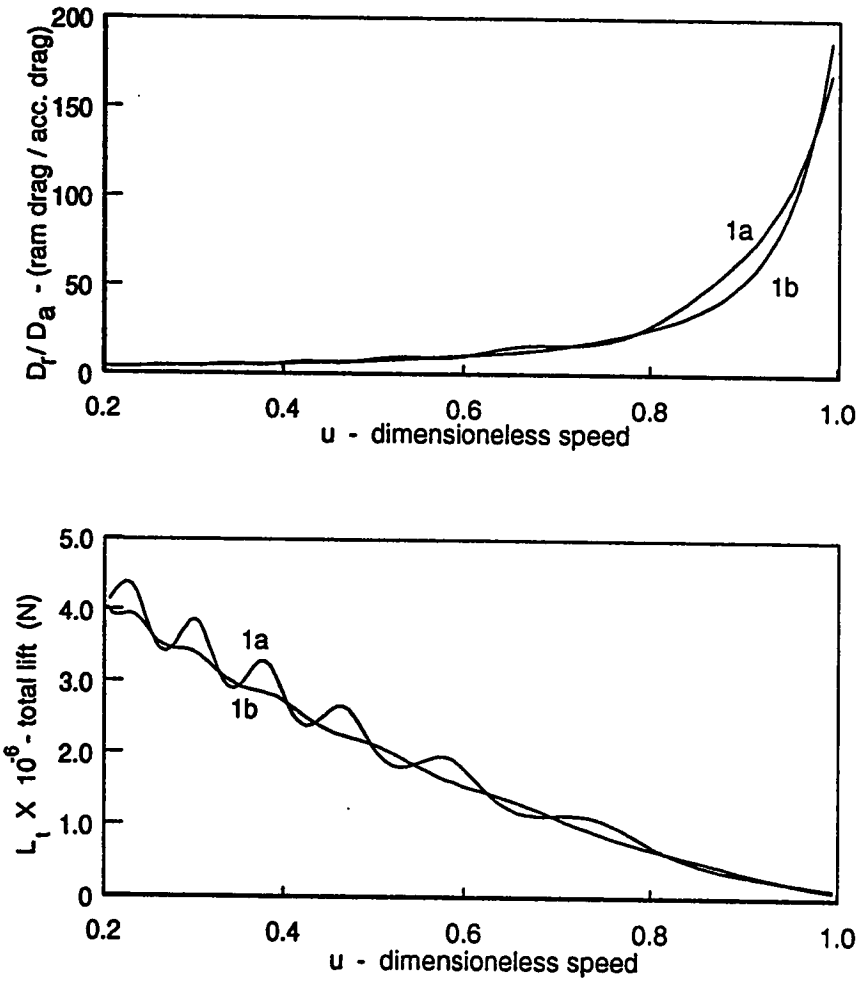

Figure 4.14: (a) D_r/D_a - (ram drag / aerodynamic drag) vs u - dimensionless velocity. (b) L_t - total lift (N) vs u - dimensionless velocity.

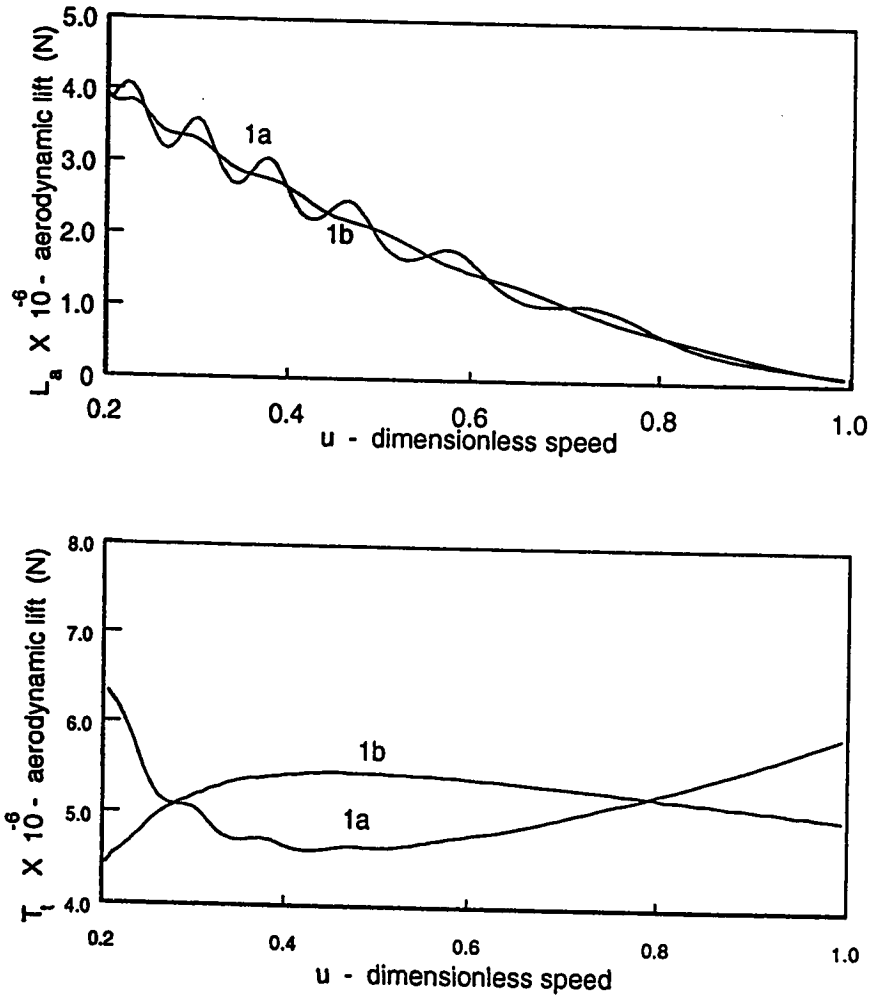

Figure 4.15: (a) L_a - aerodynamic lift (N) vs u - dimensionless velocity. (b) T_t - total thrust (N) vs u - dimensionless velocity.

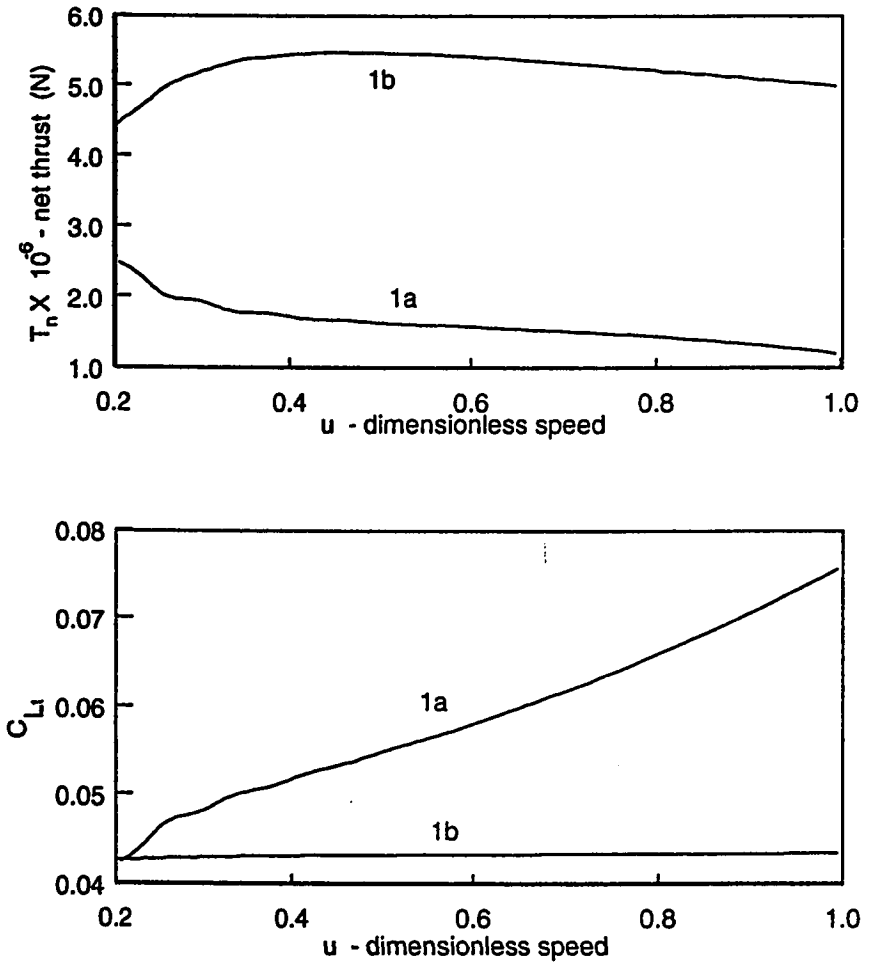

Figure 4.16: (a) T_n - net thrust (N) vs u - dimensionless velocity. (b) C_{Li} - coefficient of total lift vs u - dimensionless velocity.

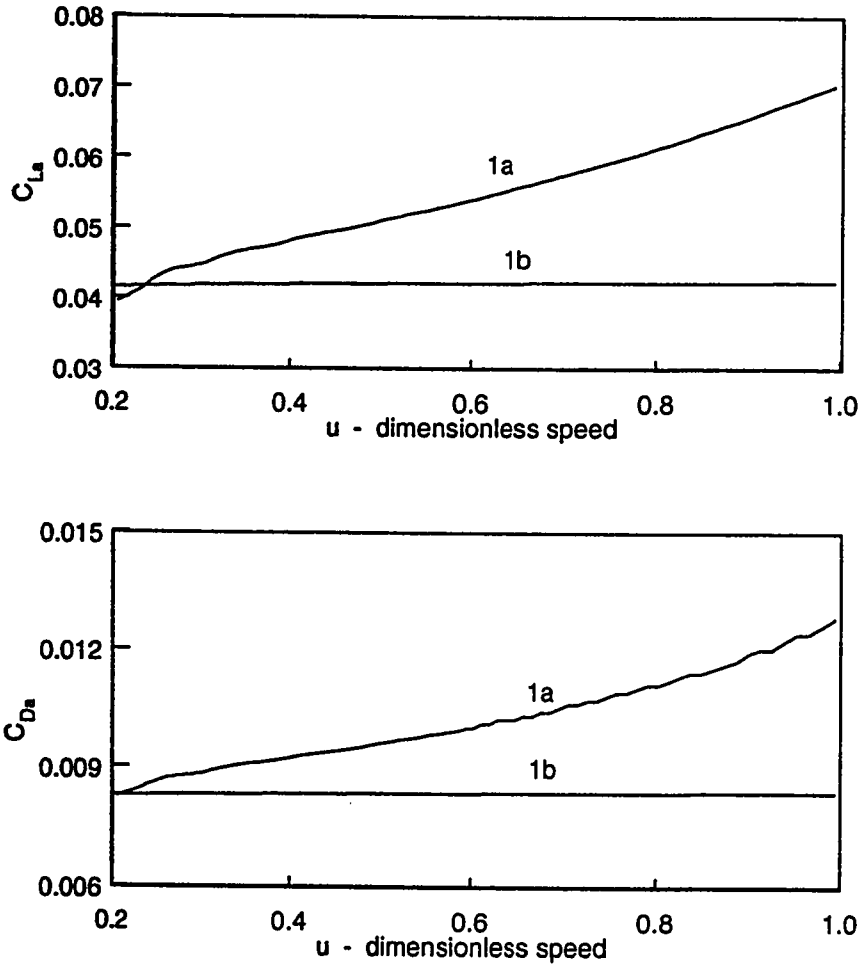

Figure 4.17: (a) C_{La} - coefficient of aerodynamic lift vs u - dimensionless velocity. (b) C_{Da} - coefficient of aerodynamic drag vs u - dimensionless velocity.

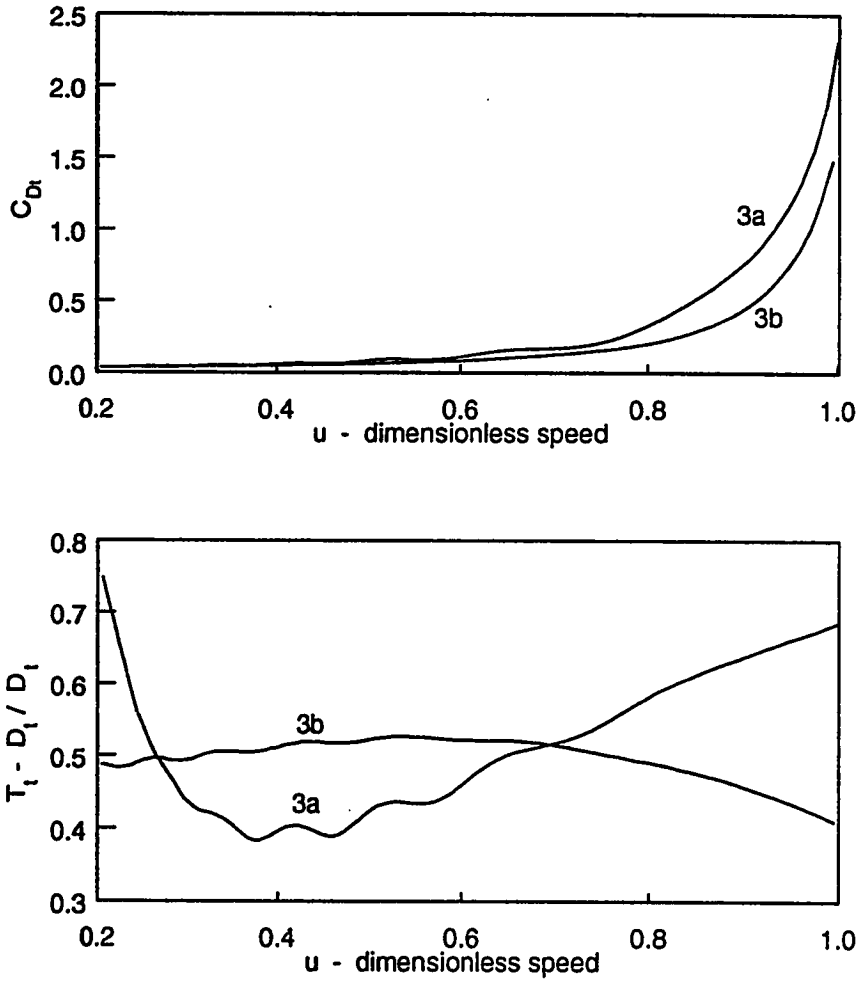

Figure 4.18: (a) C_{Dt} - coefficient of total drag vs u - dimensionless velocity. (b) $T_t - D_t/D_t$ vs u - dimensionless velocity.

4.4.3 CASE 2a-b

The CASE 2a-b are variants of CASE 1a-b. respectively with I_{sp} considered as variable ($I_{sp}(M)$). For both the cases the trajectories start at an altitude of $20km$ and the final altitude is approximately $65km$. The optimized parameter values for the controllers are given in the appendix. The results are presented in Fig. 4.19,4.31. They are mostly comparable with those of CASE 1a-b except for the following differences.

- $\dot{\gamma}$ and γ (Fig. 4.20) are smaller than those of CASE 1a-b. This means that the trajectories obtained are smoother.

- The heat load obtained using the neural controller is higher. $340kJ/cm^2$ (Fig. 4.22) as compared with $300kJ/cm^2$ using polynomial controller. This is because the trajectory obtained using the neural controller is lower. This is favorable from the engine performance view point. Since this will lead to higher overall dynamic pressure.

- The final mass (Fig. 4.24) is lower ($\mu \approx 0.2$) than the CASE 1a-b. This is because the average I_{sp} value when using variable I_{sp} is lower than the constant I_{sp}. This is not a problem because $\mu = 0.2$ implies $m \approx 90800kg$ for a typical configuration of hypersonic vehicle, which is good enough for the vehicle without fuel and payload.

- The thrust control τ_n in CASE 2b is different than that of CASE 1a. This is in contrast to the similar trends of τ_n for CASE 2a and CASE 2b. We attribute this to the capability of neural networks to model a vast range of nonlinear functions.

- The total drag and ram drag (Fig. 4.26) are lower using neural controller as compared to that of polynomial controller. This is in contrast to CASE 1a-b.

4.4.4 CASE 3a-b

This case and CASE 4a-b are studied to see the effect of altitude on the optimized heat load and in general the trajectories. The trajectory starts at an initial height of $10km$, and ends at a height of approximately $60km$. The other parameters remain the same as in CASE 1a. The results are presented in Fig. 4.32 to 4.43.

Figures 4.32 shows h vs u and u vs t. It is seen that the trajectories using neural controller is on an average lower than that using a polynomial controller. This will off course lead to higher heat loads, however this also has an advantage in terms of dynamic pressure.

Figures 4.33 shows $\dot{\gamma}$ vs u and γ vs u, as was seen in CASE 1 and CASE 2, γ and $\dot{\gamma}$ are very small when using a neural controller. This gives a very smooth trajectory.

Figures 4.34 shows ρ vs u and θ vs u, the density of CASE 3b stays higher than CASE 3a since the trajectory of CASE 3b is lower.

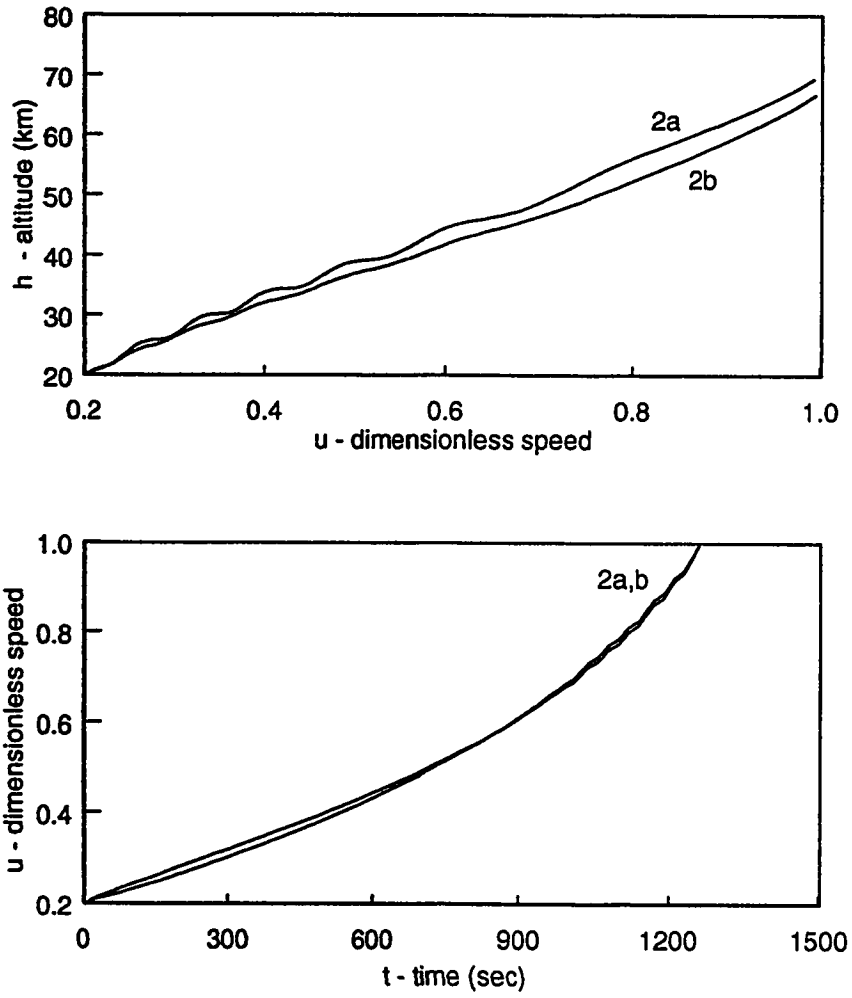

Figure 4.19: (a) h - altitude (km) vs u - dimensionless velocity. (b) u - dimensionless velocity vs t - time (sec).

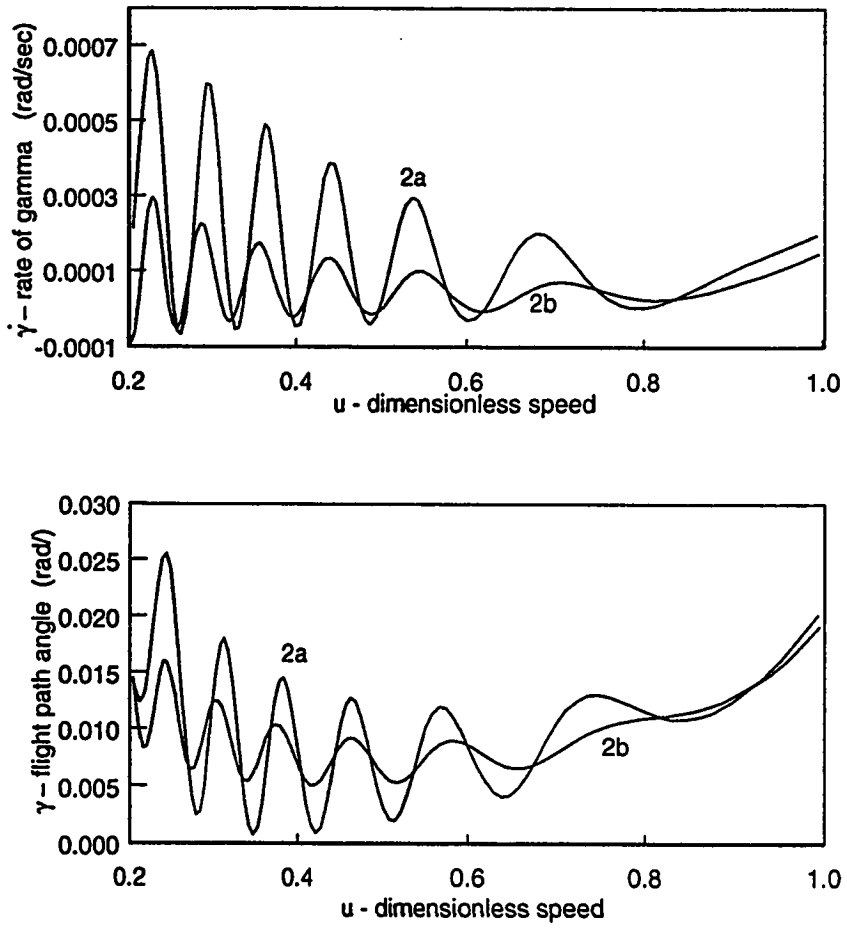

Figure 4.20: (a) $\dot{\gamma}$ - rate of change of flight path angle (rad/sec) vs u - dimensionless velocity. (b) γ - flight path angle (rad) vs u - dimensionless velocity.

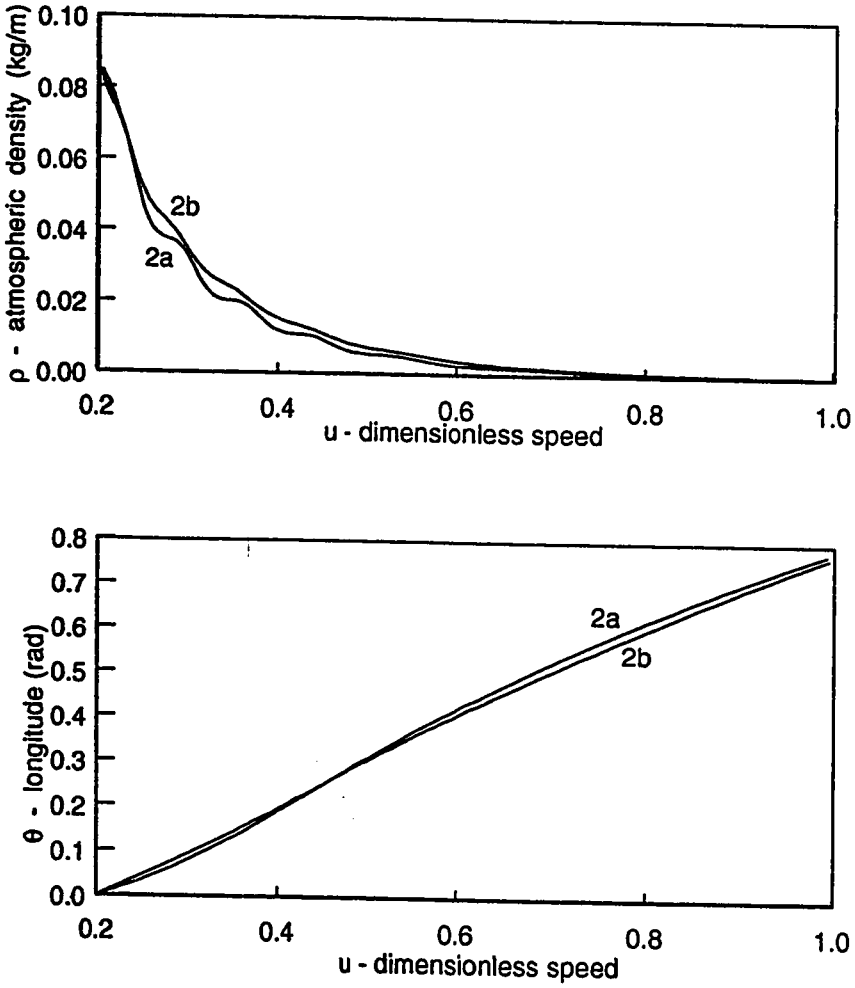

Figure 4.21: (a) ρ - atmospheric density (kg/m^3) vs u - dimensionless velocity. (b) θ - longitude (rad) vs u - dimensionless velocity.

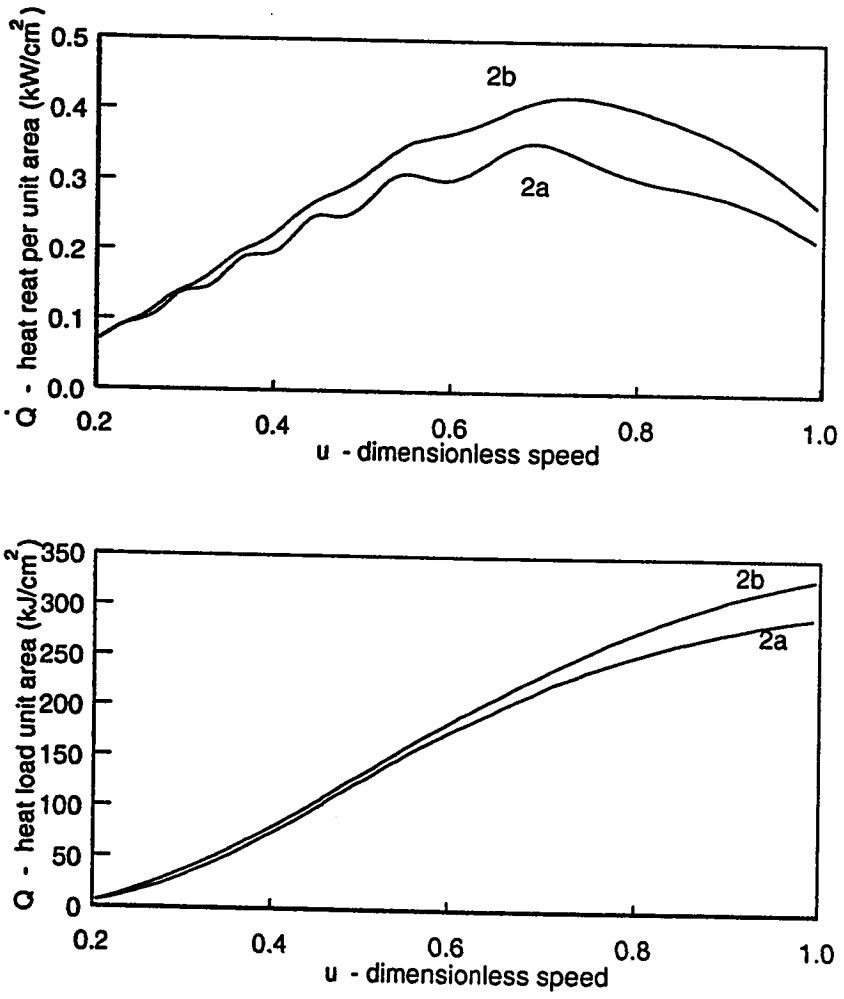

Figure 4.22: (a) $\dot{Q}$ - heat rate per unit area (kW/cm^2) vs u - dimensionless velocity. (b) Q - heat load per unit area (kJ/cm^2) vs u - dimensionless velocity.

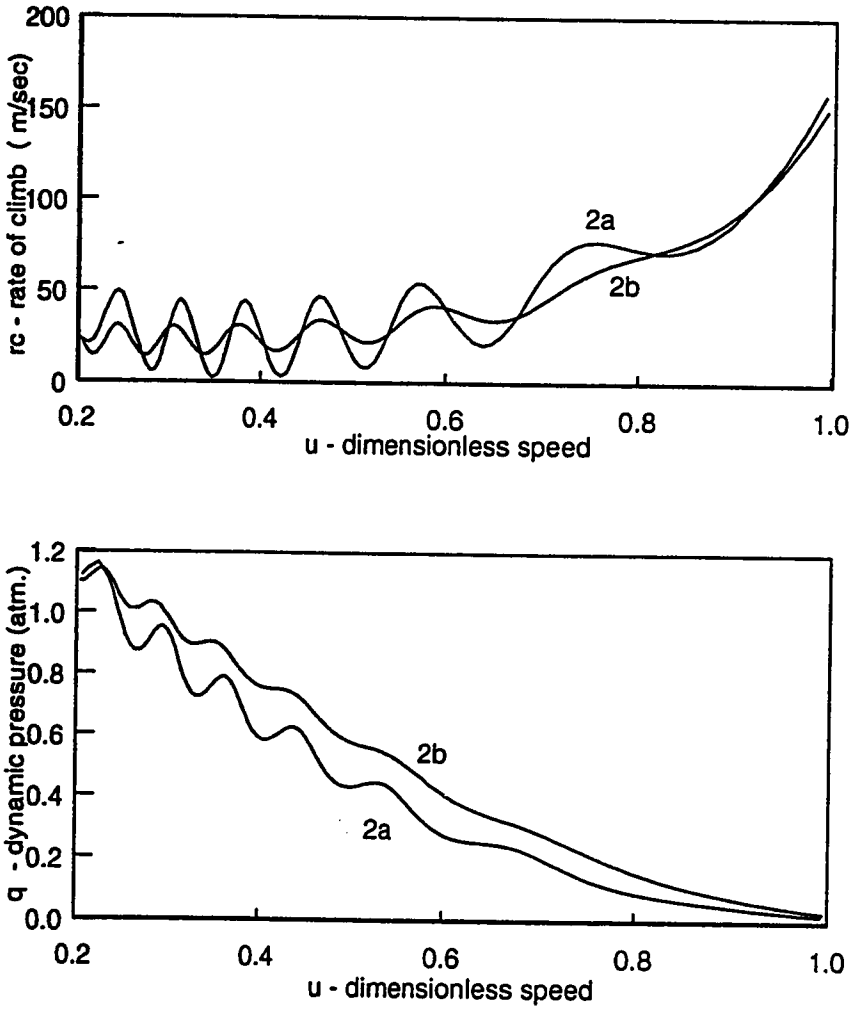

Figure 4.23: (a) rc - rate of climb (m/sec) vs u - dimensionless velocity. (b) q - dynamic pressure $(atm.)$ vs u - dimensionless velocity.

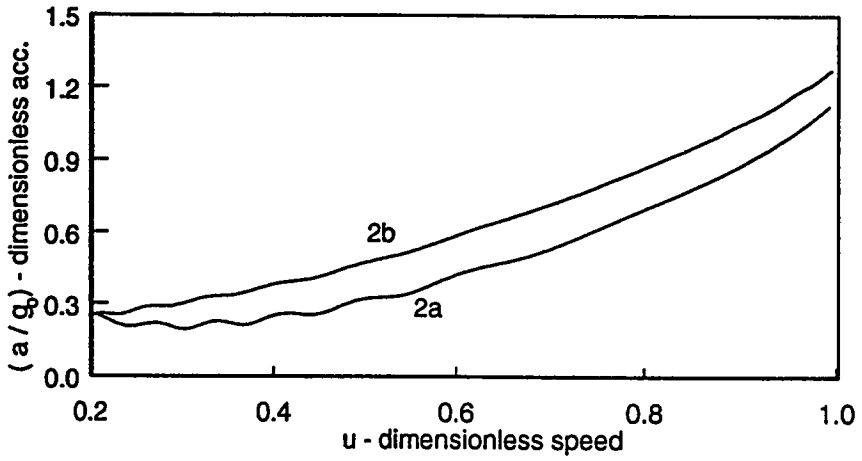

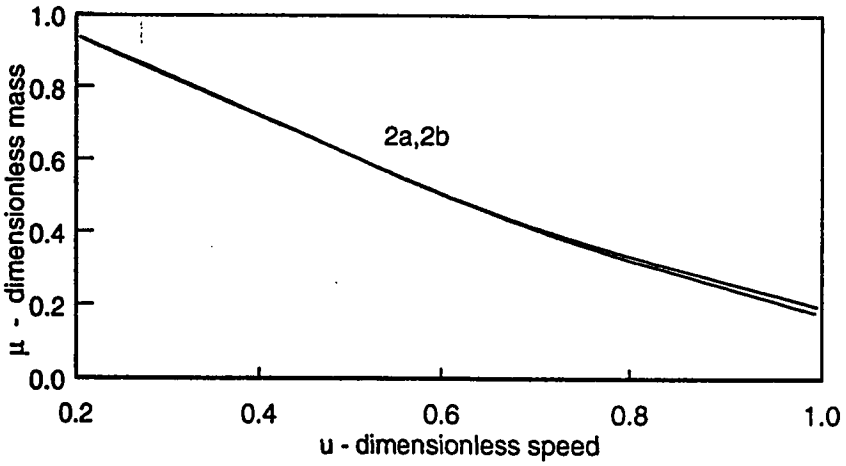

Figure 4.24: (a) (a/g_o) - dimensionless acceleration vs u - dimensionless velocity. (b) μ - dimensionless mass vs u - dimensionless velocity.

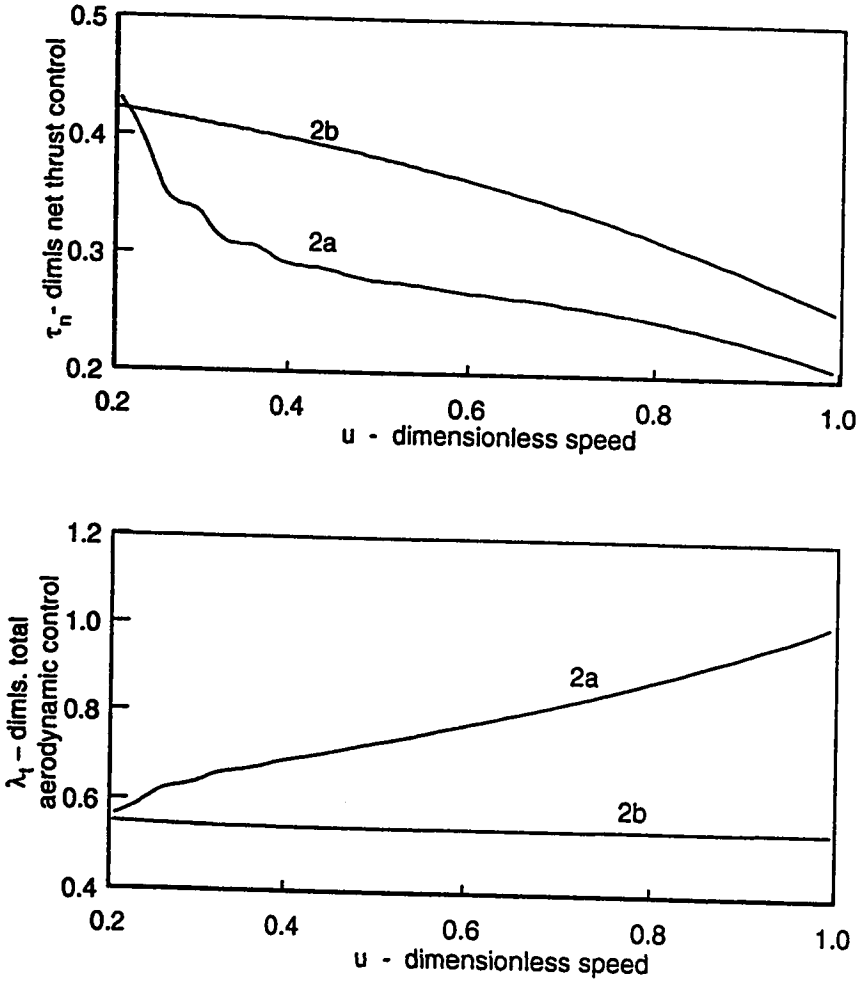

Figure 4.25: (a) τ_n - dimensionless net thrust control vs u - dimensionless velocity. (b) λ_t - dimensionless total aerodynamic control vs u - dimensionless velocity.

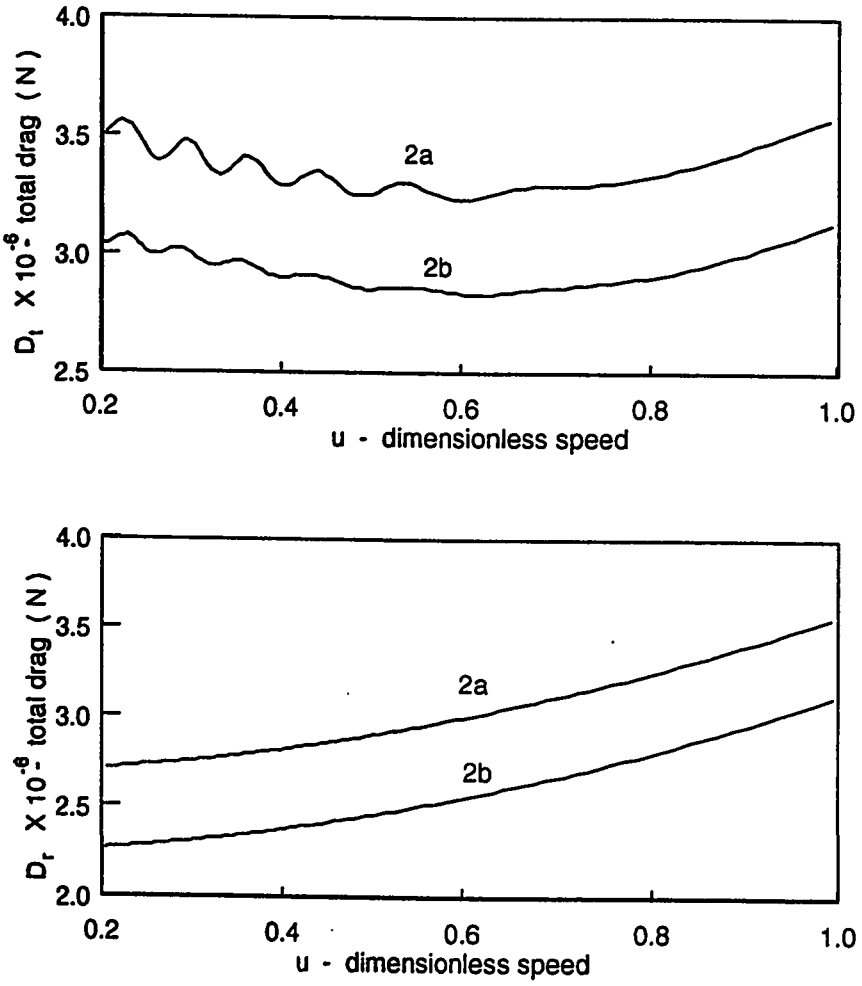

Figure 4.26: (a) D_t - total drag (N) vs u - dimensionless velocity. (b) D_r - ram drag (N) vs u - dimensionless velocity.

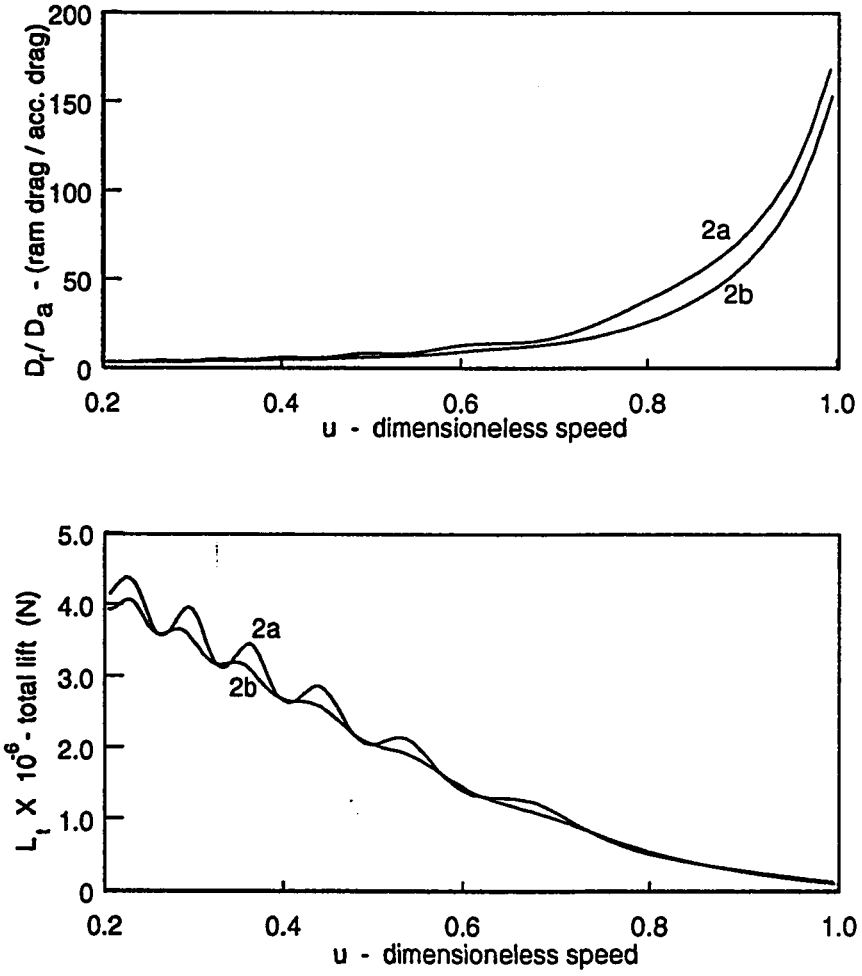

Figure 4.27: (a) D_r/D_a - (ram drag / aerodynamic drag) vs u - dimensionless velocity. (b) L_t - total lift (N) vs u - dimensionless velocity.

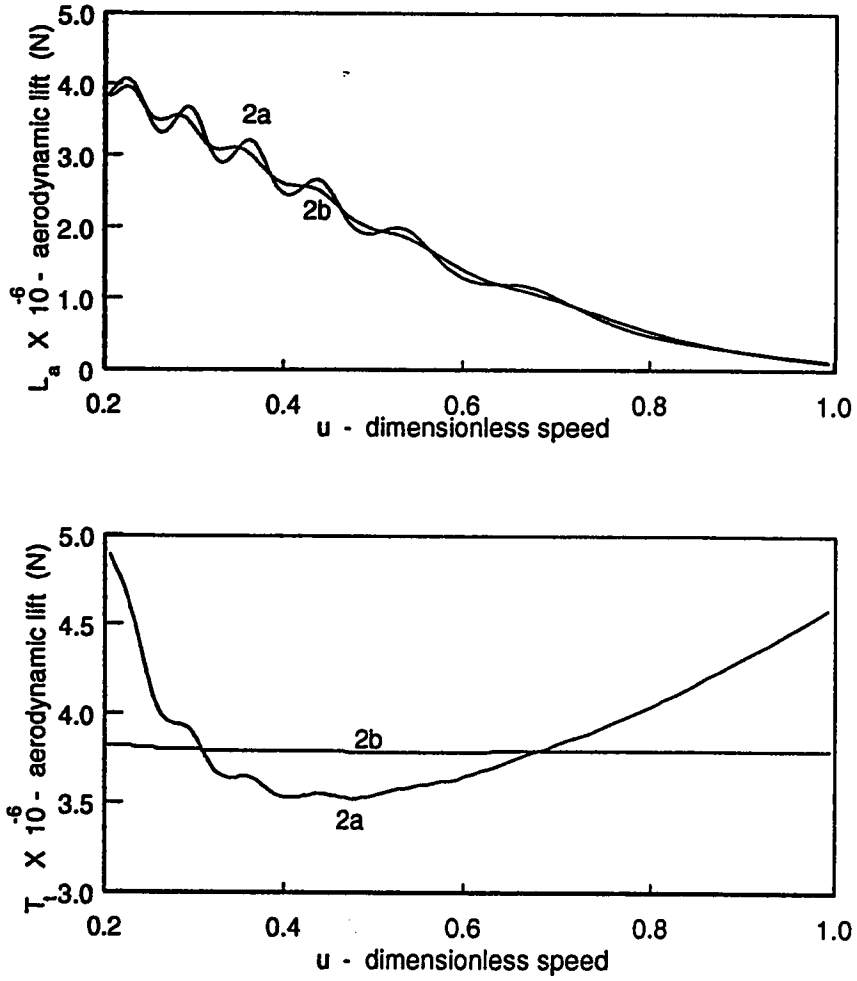

Figure 4.28: (a) L_a - aerodynamic lift (N) vs u - dimensionless velocity. (b) T_l - total thrust (N) vs u - dimensionless velocity.

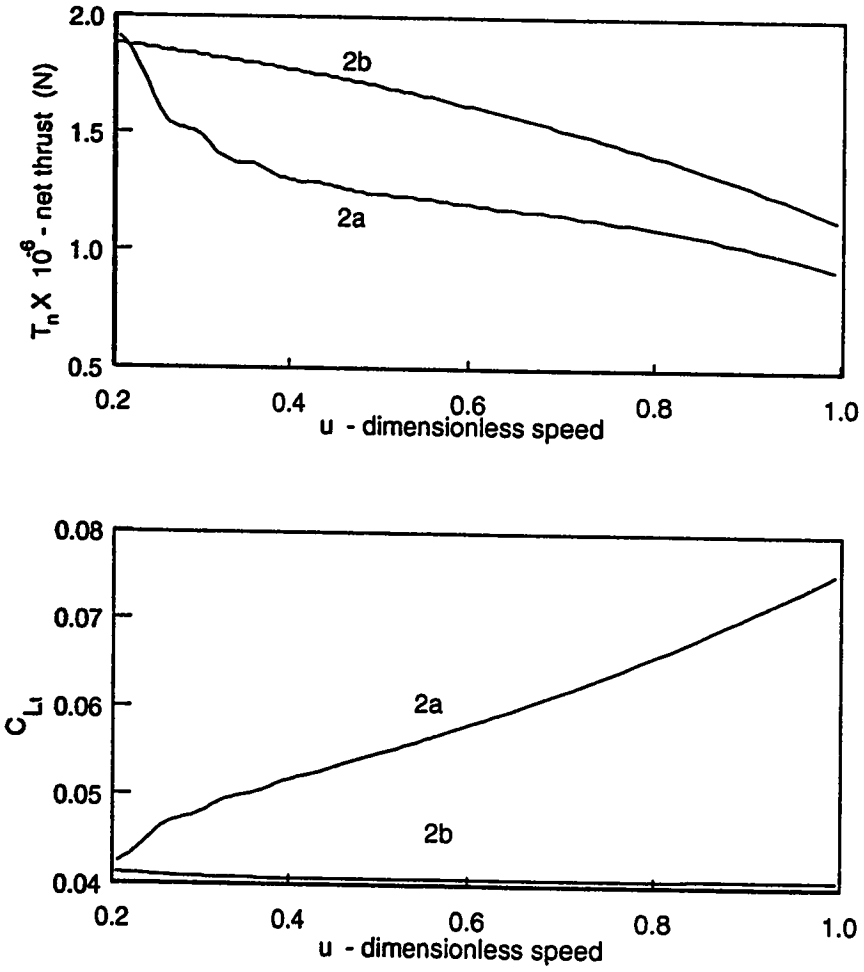

Figure 4.29: (a) T_n - net thrust (N) vs u - dimensionless velocity. (b) C_{Li} - coefficient of total lift vs u - dimensionless velocity.

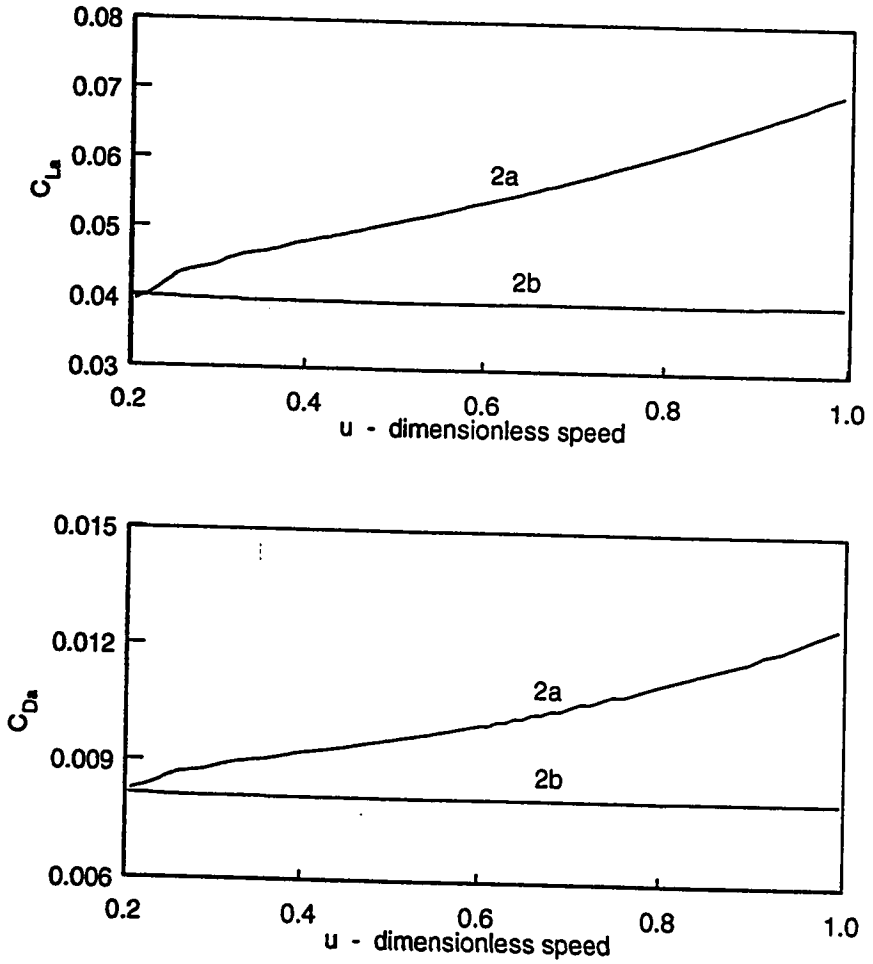

Figure 4.30: (a) C_{La} - coefficient of aerodynamic lift vs u - dimensionless velocity. (b) C_{Da} - coefficient of aerodynamic drag vs u - dimensionless velocity.

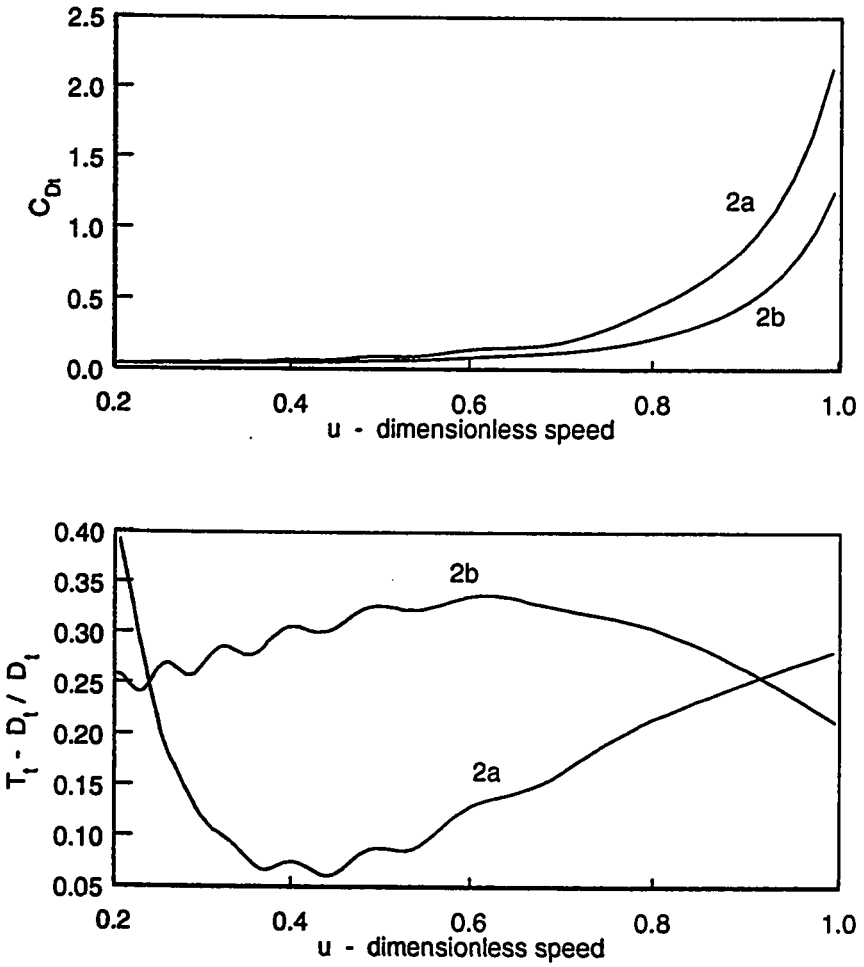

Figure 4.31: (a) C_{Dt} - coefficient of total drag vs u - dimensionless velocity. (b) $T_t - D_t/D_t$ vs u - dimensionless velocity.

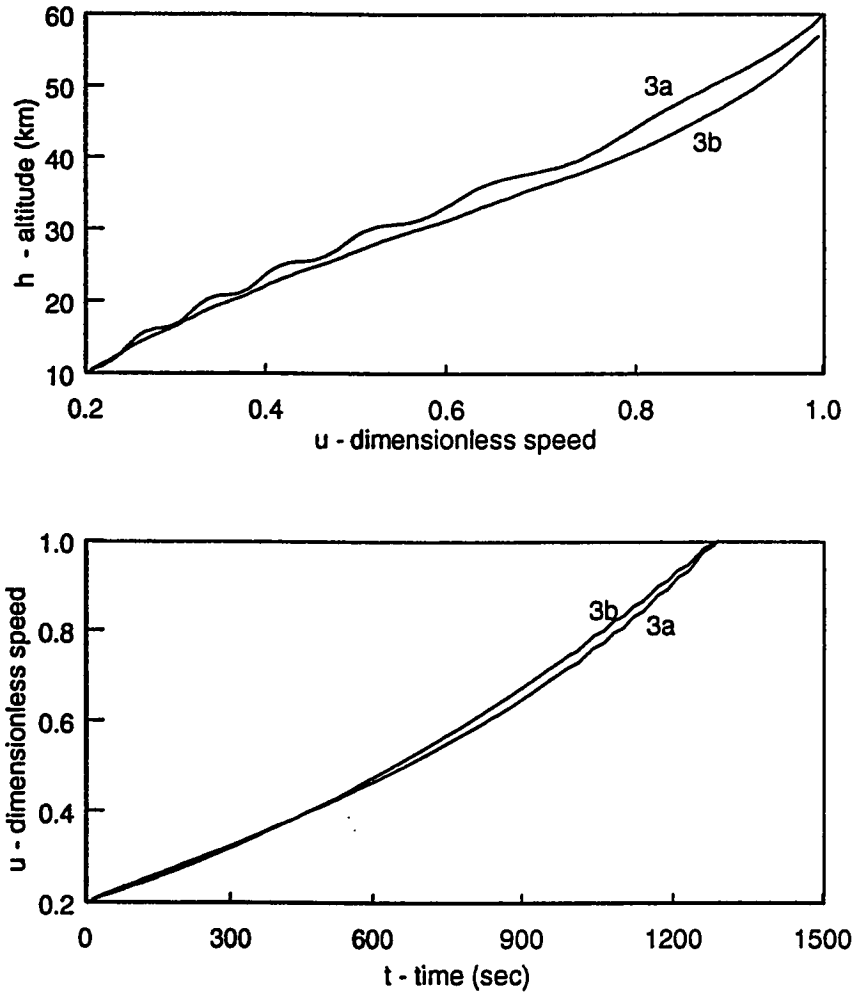

Figure 4.32: (a) h - altitude (km) vs u - dimensionless velocity. (b) u - dimensionless velocity vs t - time (sec).

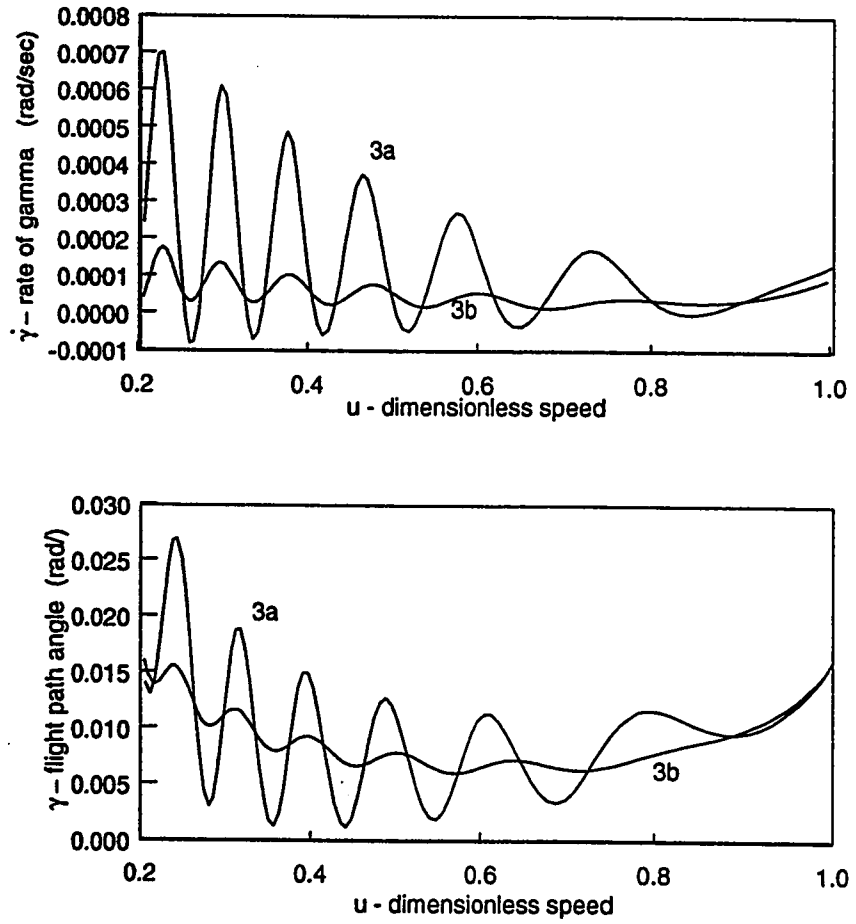

Figure 4.33: (a) $\dot{\gamma}$ - rate of change of flight path angle (rad/sec) vs u - dimensionless velocity. (b) γ - flight path angle (rad) vs u - dimensionless velocity.

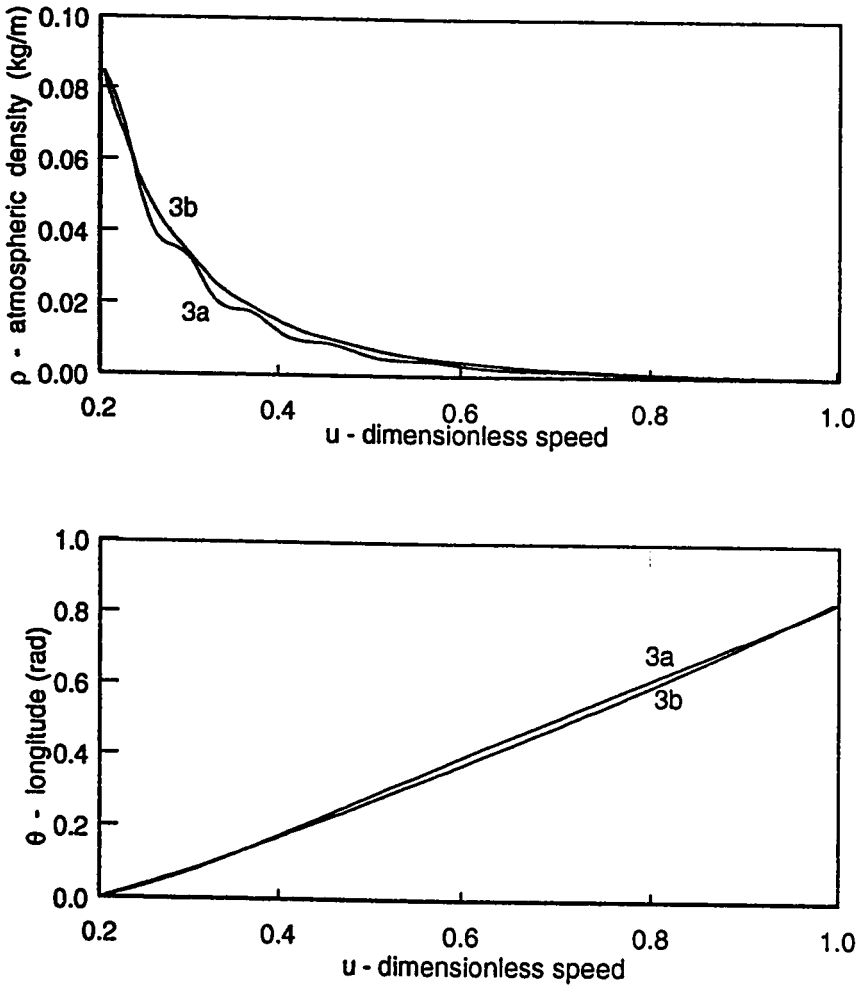

Figure 4.34: (a) ρ - atmospheric density (kg/m^3) vs u - dimensionless velocity. (b) θ - longitude (rad) vs u - dimensionless velocity.

Figures 4.35 shows $\dot{Q}$ vs u and Q vs u, we can see that the heat load and the heat rate for trajectories of CASE 3b is higher than that of CASE 3a. This again is attributed to the lower overall trajectory of CASE 3b. The heat loads are approximately $300kJ/cm^2$ and $350kJ/cm^2$ for CASE 3a and CASE 3b respectively. Inspite of the fact that the heat load in CASE 3b is higher, the trajectory may be still preferable when we consider the overall characteristics.

Figures 4.36 shows rc vs u and q vs u, the variation of rate of climb is very smooth in CASE 3b as compared to that of CASE 3a. This corresponds to the observations made for γ and $\dot{\gamma}$. The dynamic pressure q is on an average higher for CASE 3b. This is a favorable trend also seen in all the previous cases using a neural controller.

Figures 4.37 shows a/g_o vs u and μ vs u for the two cases. The dimensionless acceleration stays within reasonable limits. The final dimensionless mass is around 0.3 which is pretty good.

Figures 4.38 shows τ_n vs u and λ_t vs u. The aerodynamic control and the thrust control satisfy the constraints. The aerodynamic control using neural controller stays almost constant throughout the flight trajectory.

Figures 4.39 to 4.44 present the results for the drags, lift, coefficients of lift and drag, etc. All these are seen to satisfy the constraints and are in reasonable limits.

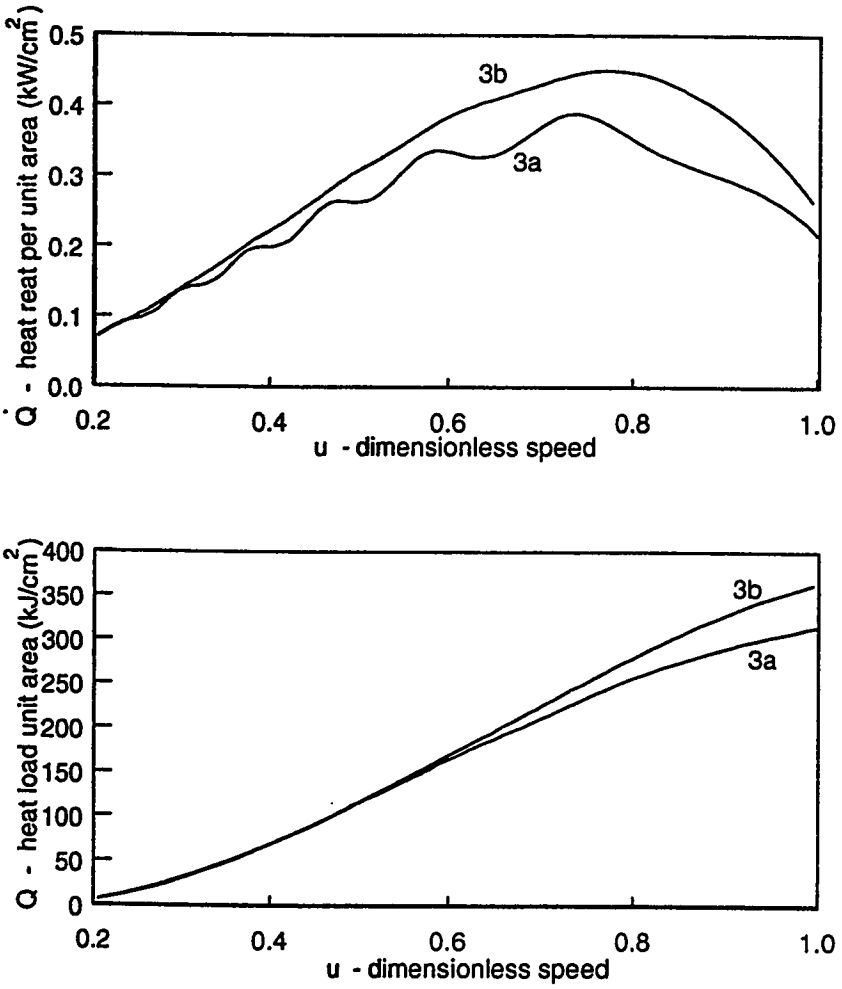

Figure 4.35: (a) $\dot{Q}$ - heat rate per unit area (kW/cm^2) vs u - dimensionless velocity. (b) Q - heat load per unit area (kJ/cm^2) vs u - dimensionless velocity.

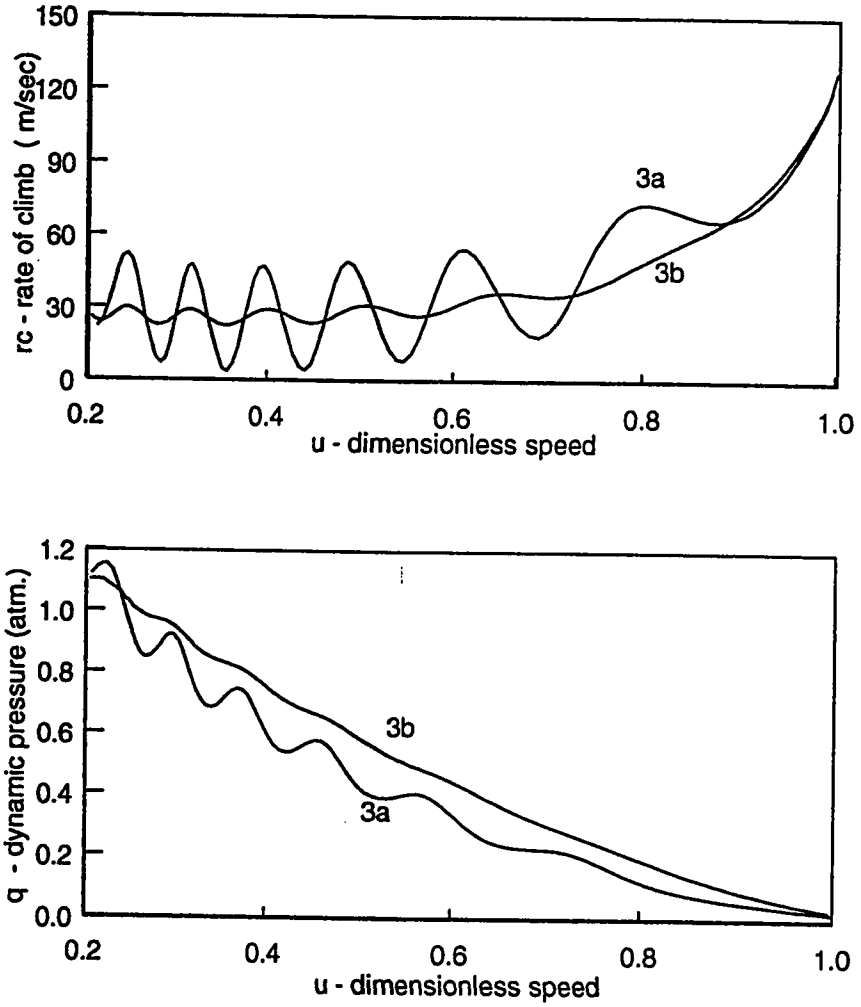

Figure 4.36: (a) rc - rate of climb (m/sec) vs u - dimensionless velocity. (b) q - dynamic pressure $(atm.)$ vs u - dimensionless velocity.

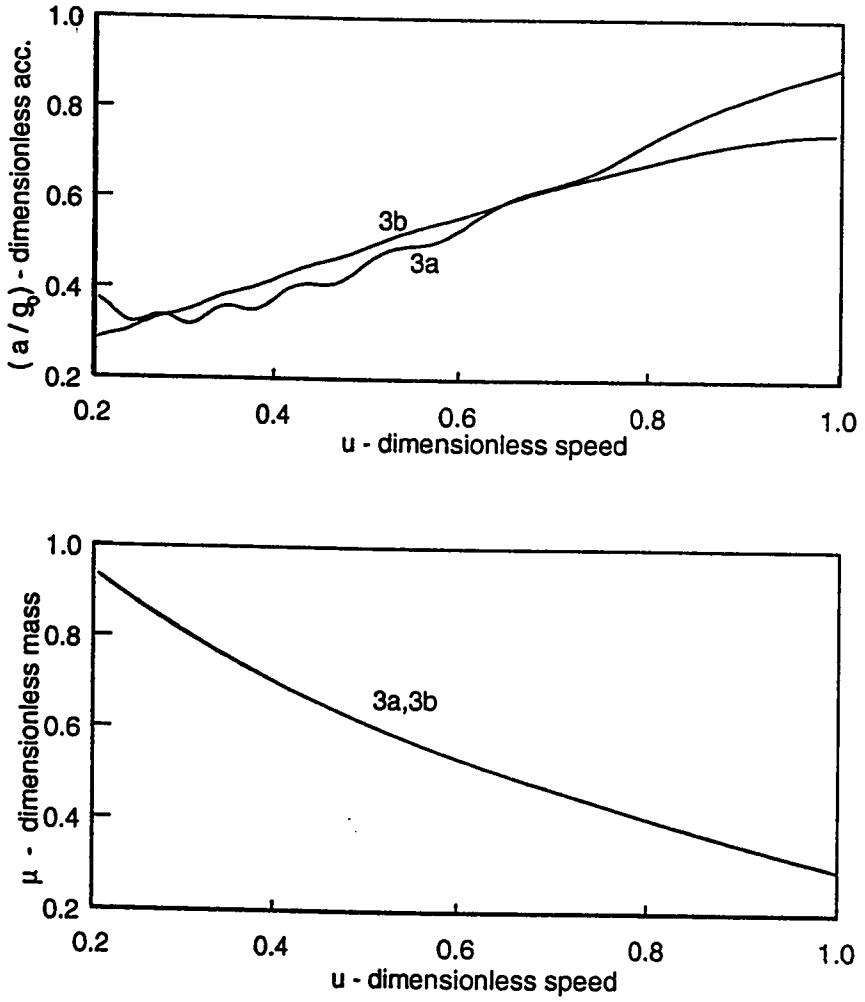

Figure 4.37: (a) (a/g_o) - dimensionless acceleration vs u - dimensionless velocity. (b) μ - dimensionless mass vs u - dimensionless velocity.

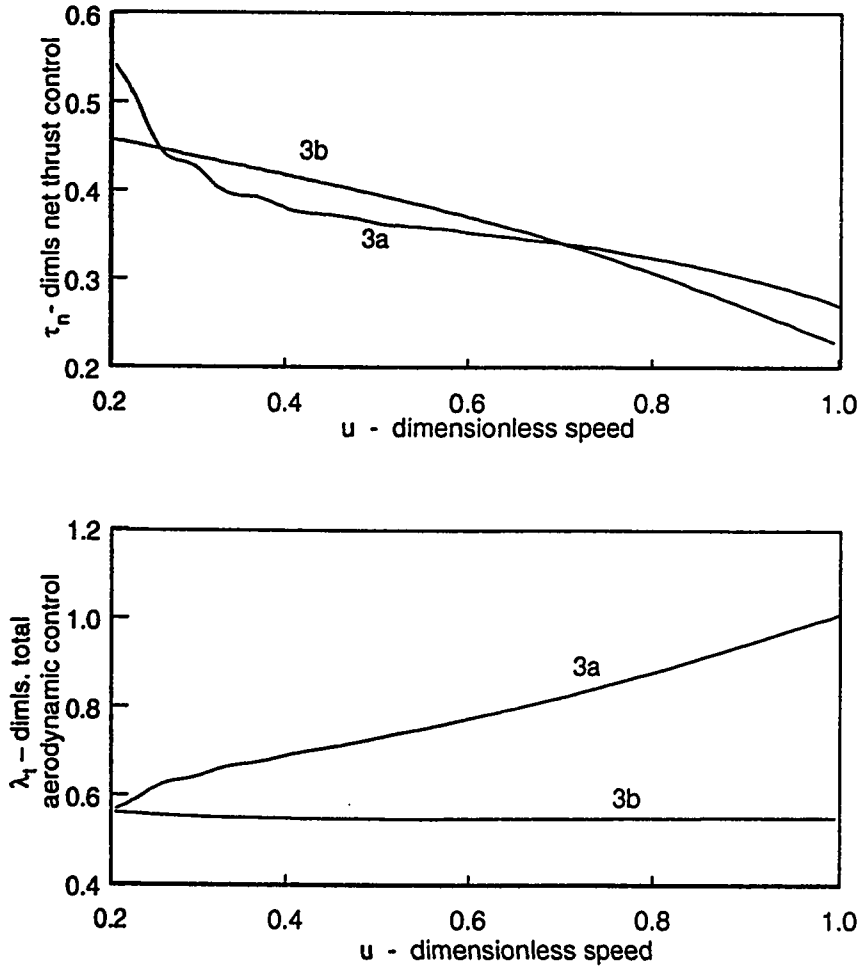

Figure 4.38: (a) τ_n - dimensionless net thrust control vs u - dimensionless velocity. (b) λ_t - dimensionless total aerodynamic control vs u - dimensionless velocity.

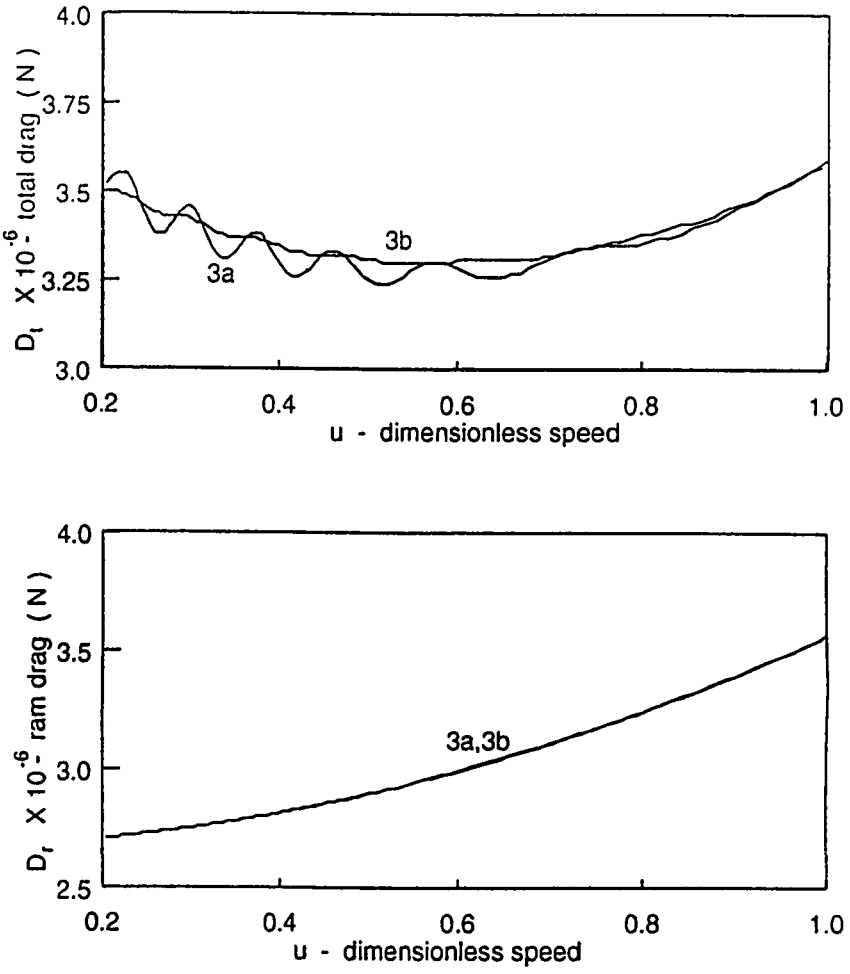

Figure 4.39: (a) D_t - total drag (N) vs u - dimensionless velocity. (b) D_r - ram drag (N) vs u - dimensionless velocity.

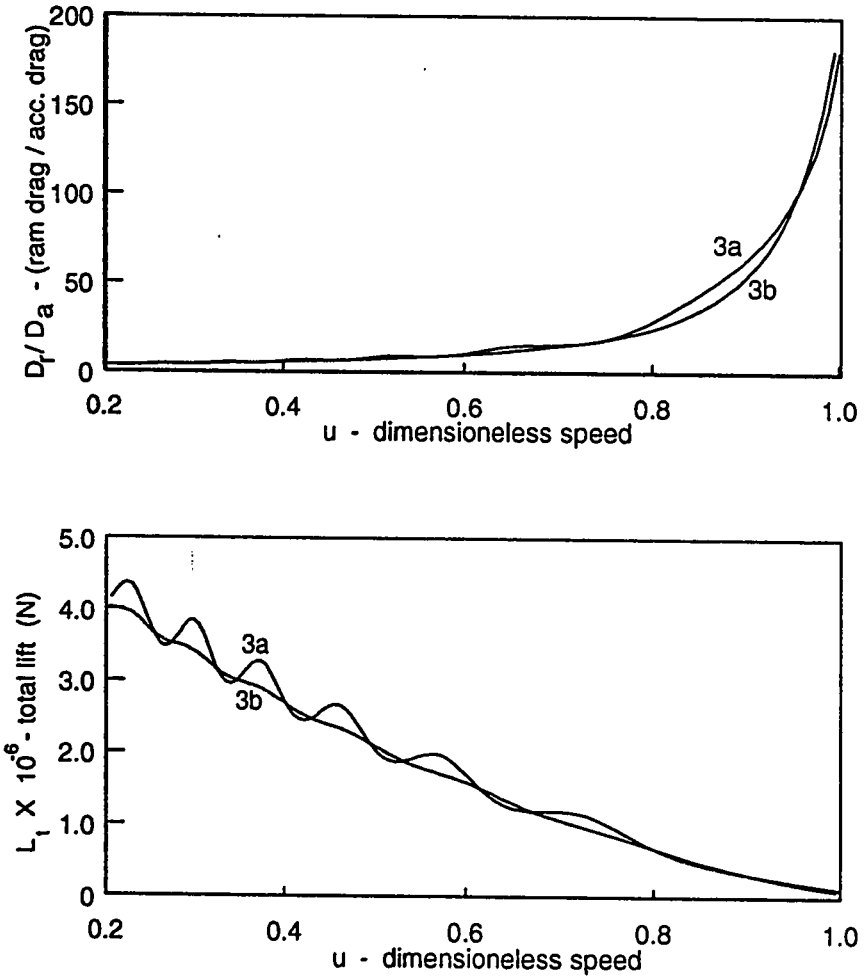

Figure 4.40: (a) D_r/D_a - (ram drag / aerodynamic drag) vs u - dimensionless velocity. (b) L_t - total lift (N) vs u - dimensionless velocity.

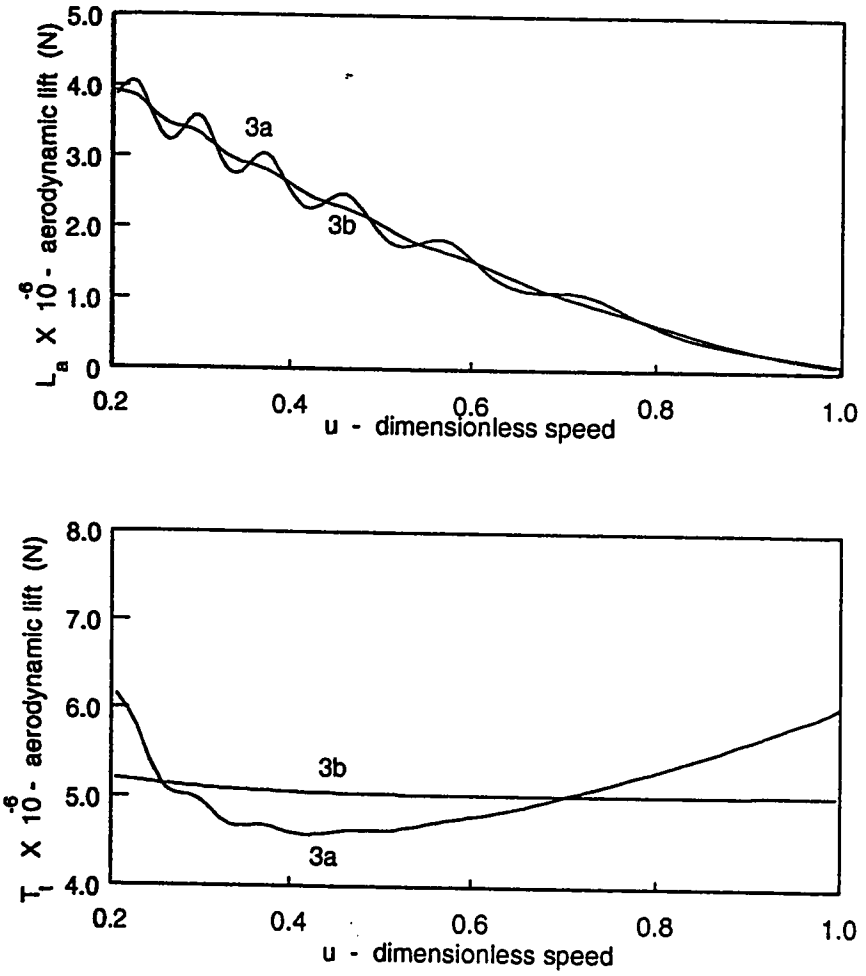

Figure 4.41: (a) L_a - aerodynamic lift (N) vs u - dimensionless velocity. (b) T_l - total thrust (N) vs u - dimensionless velocity.

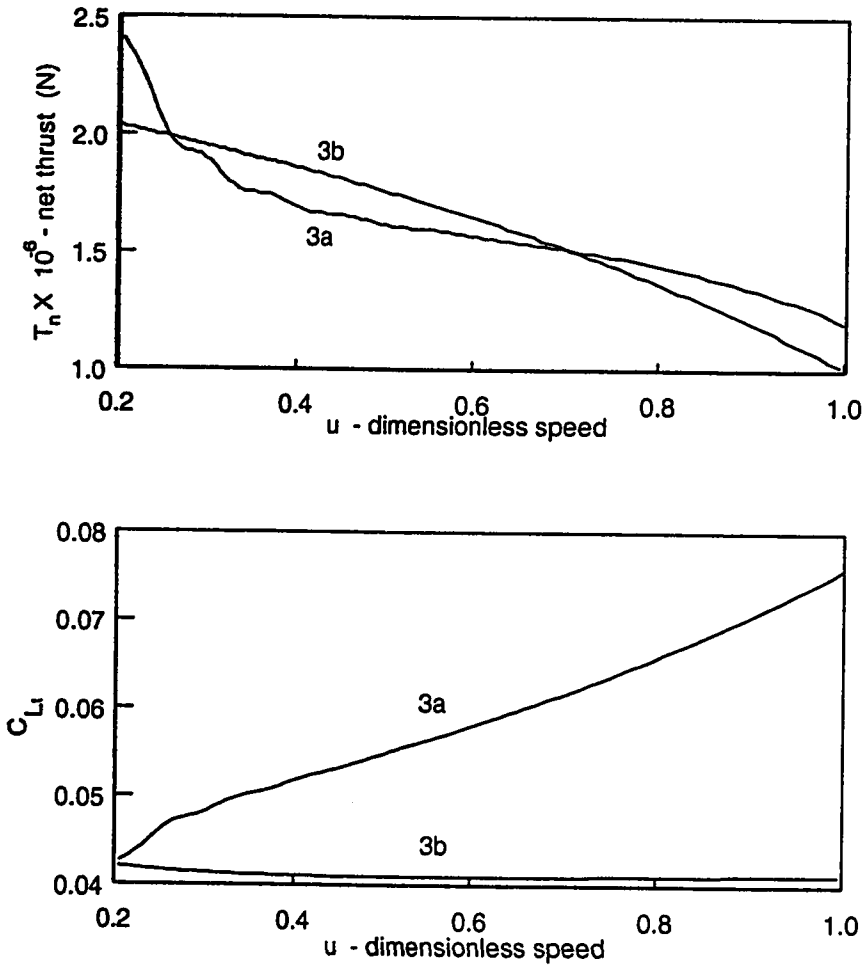

Figure 4.42: (a) T_n - net thrust (N) vs u - dimensionless velocity. (b) C_{Lt} - coefficient of total lift vs u - dimensionless velocity.

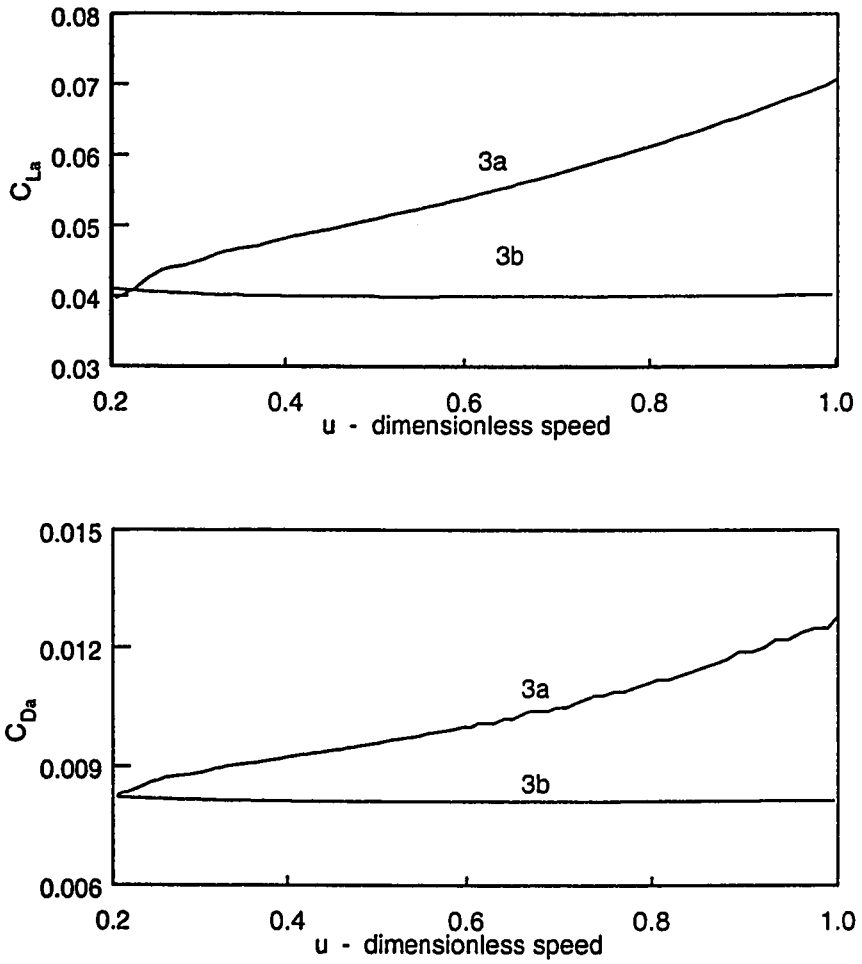

Figure 4.43: (a) C_{La} - coefficient of aerodynamic lift vs u - dimensionless velocity. (b) C_{Da} - coefficient of aerodynamic drag vs u - dimensionless velocity.

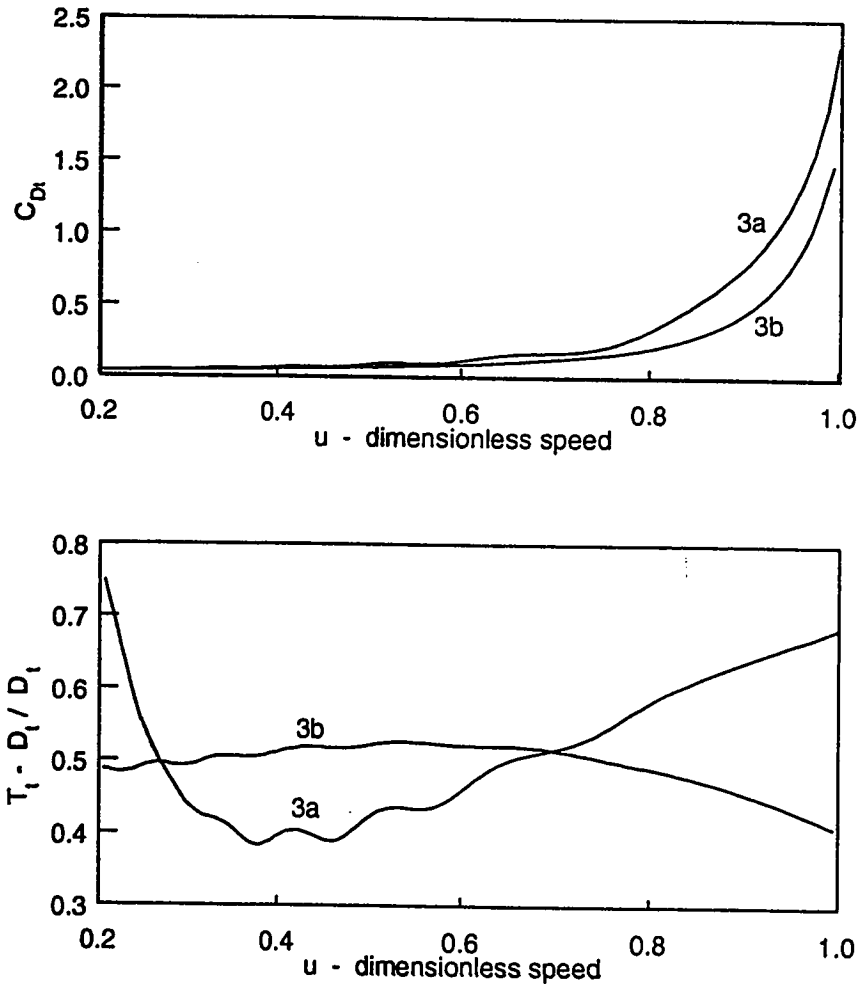

Figure 4.44: (a) C_{Dt} - coefficient of total drag vs u - dimensionless velocity. (b) $T_t - D_t/D_t$ vs u - dimensionless velocity.

4.4.5 CASE 4a-b

The CASE 4a-b are variants of CASE 3a-b respectively with I_{sp} considered as variable ($I_{sp}(M)$). For both the cases the trajectories start at an altitude of $10km$ and the final altitude is approximately $65km$. The optimized parameter values for the controllers are given in the appendix. The results are presented in Fig. 4.45,4.57. They are mostly comparable with those of CASE 3a-b except for the following differences.

- Unlike CASE 3a-b the values of γ and $\dot{\gamma}$ are comparable. Fig. 4.46.
- The heat rate and heat load using the neural controller are lower than that obtained using polynomial controller. This is in contrast to the previous case. Fig. 4.48. This might seem as a contradiction, but this type of results are expected, because of the sub-optimal nature of the solutions.
- The dynamic pressure in CASE 4b is in general lower than the dynamic pressure of CASE 4a. This is consistent with the fact that the trajectory of CASE 4a is higher, Fig. 4.49. Since a lower trajectory results in higher densities and thus higher dynamic pressures.
- The final mass for both the cases is less than 0.2. Fig. 4.50. This is of concern since this will leave smaller payload. The lower final mass is due to two reasons. (i) we are using a low average I_{sp} value. The final mass will improve

with higher average I_{sp} values. (ii) Since the average trajectory height is low the drag increases. Hence more fuel is spent.

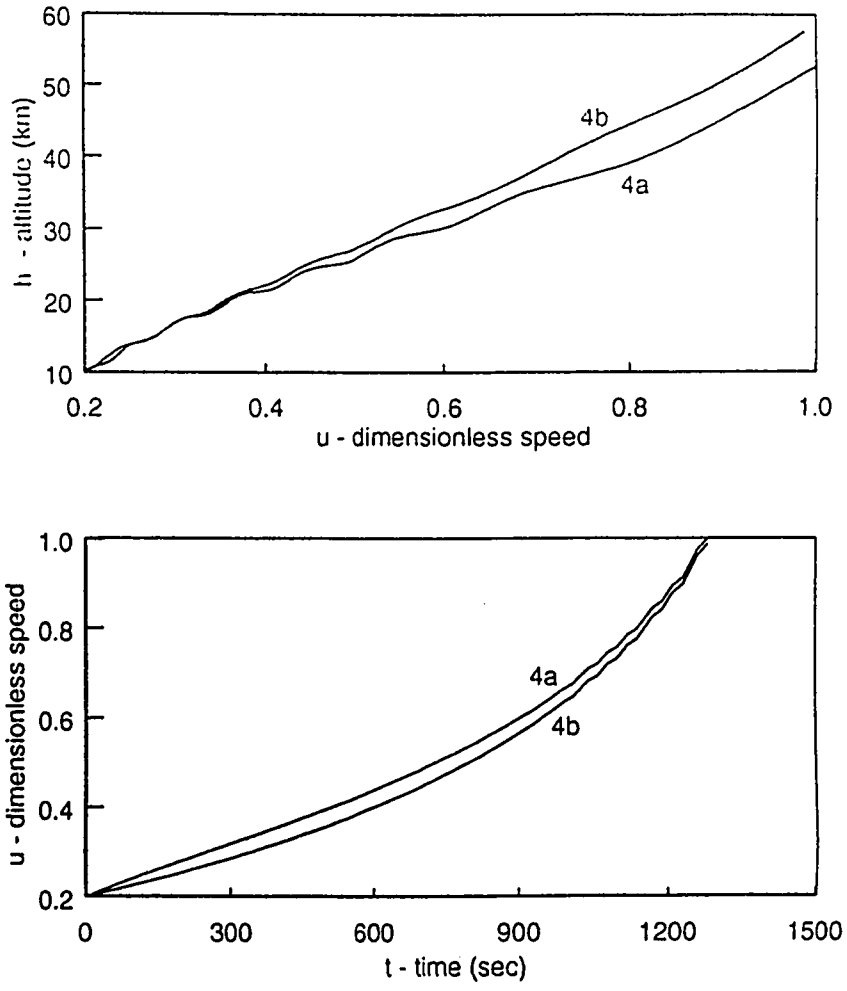

Figure 4.45: (a) h - altitude (km) vs u - dimensionless velocity. (b) u - dimensionless velocity vs t - time (sec).

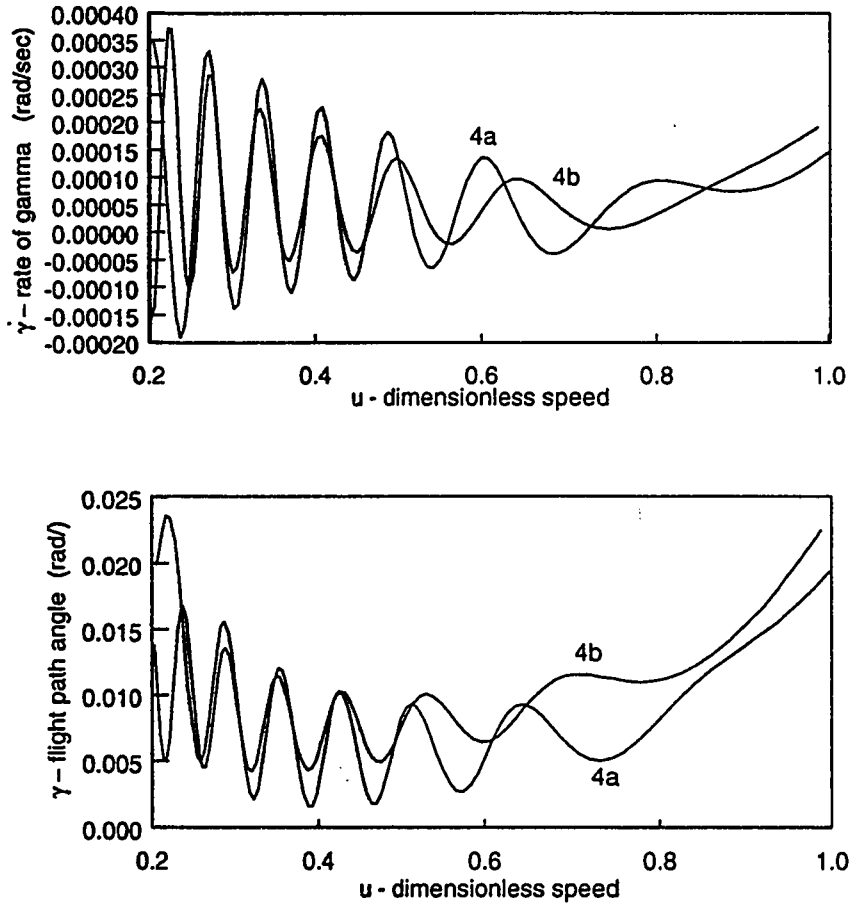

Figure 4.46: (a) $\dot{\gamma}$ - rate of change of flight path angle (rad/sec) vs u - dimensionless velocity. (b) γ - flight path angle (rad) vs u - dimensionless velocity.

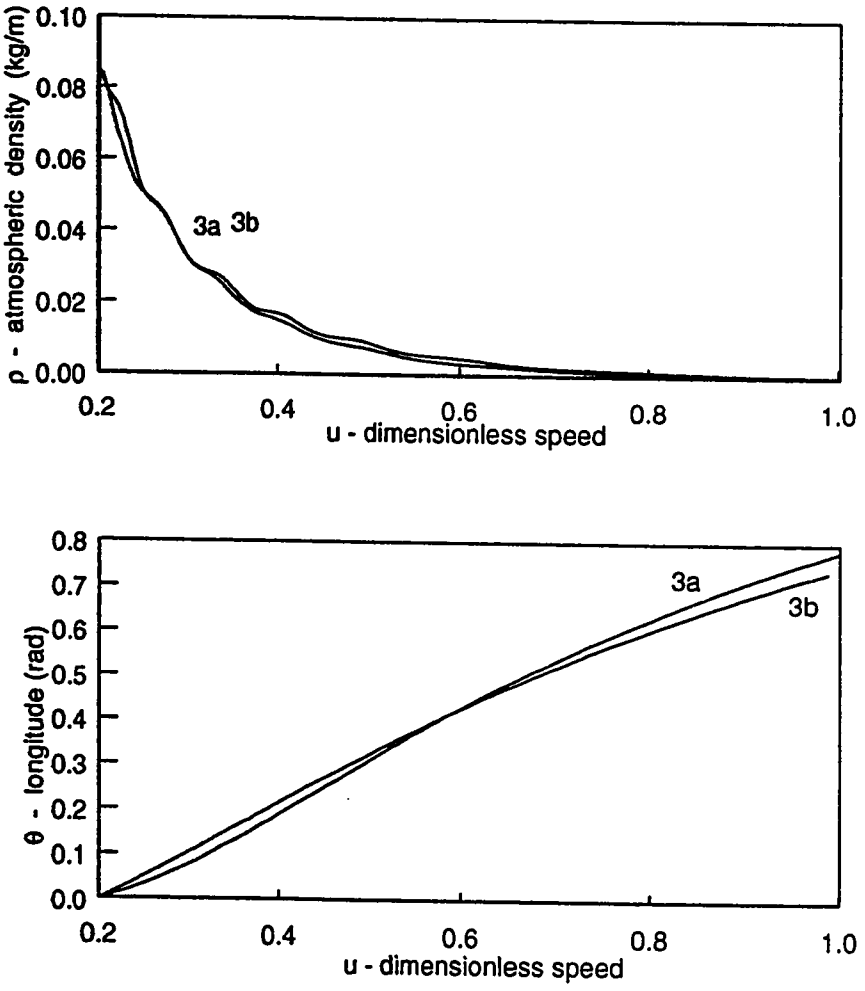

Figure 4.47: (a) ρ - atmospheric density (kg/m^3) vs u - dimensionless velocity. (b) θ - longitude (rad) vs u - dimensionless velocity.

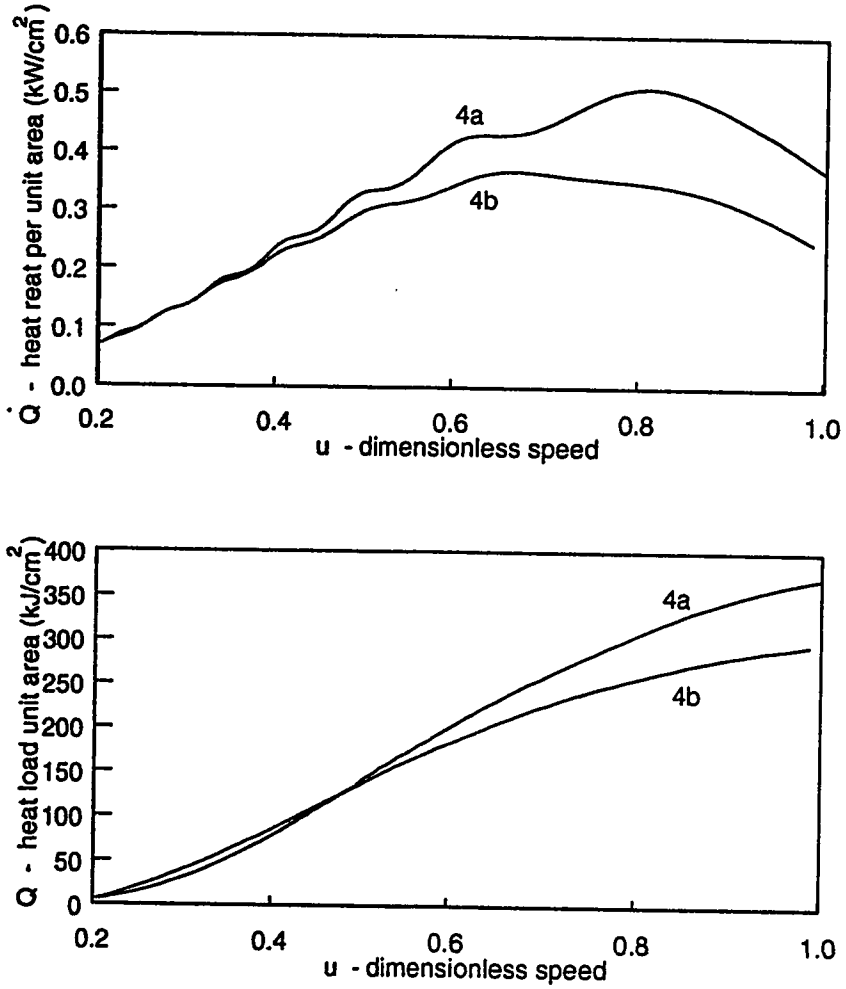

Figure 4.48: (a) $\dot{Q}$ - heat rate per unit area (kW/cm^2) vs u - dimensionless velocity. (b) Q - heat load per unit area (kJ/cm^2) vs u - dimensionless velocity.

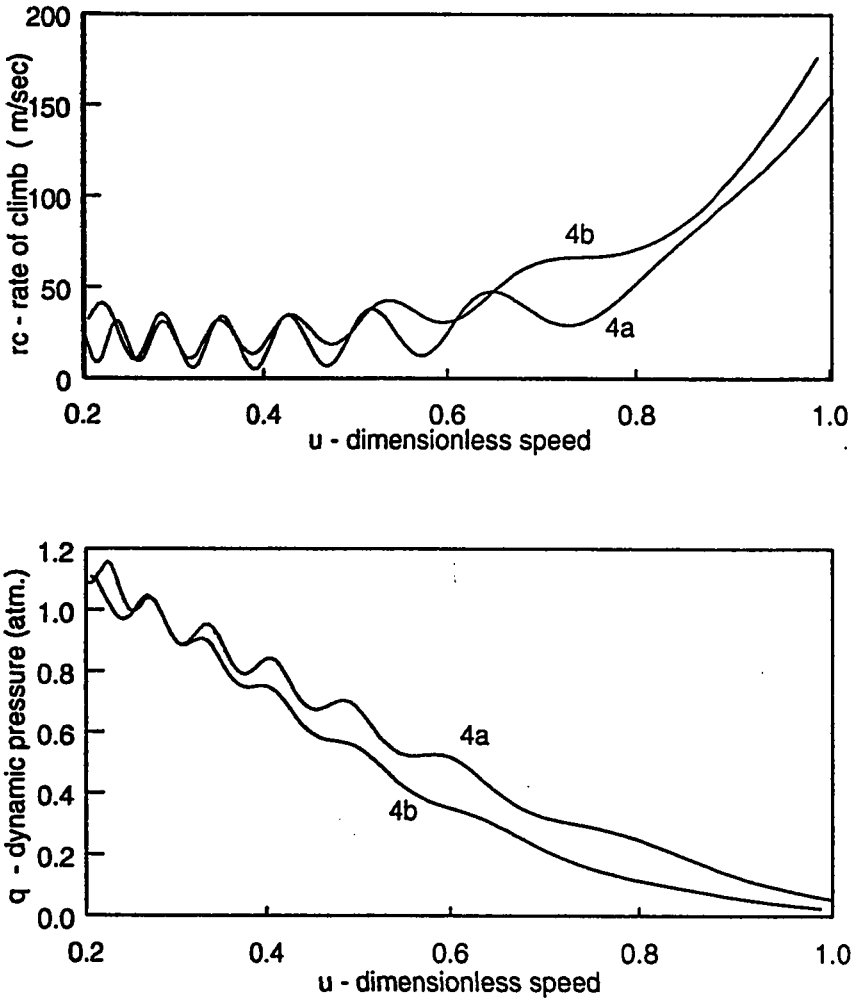

Figure 4.49: (a) rc - rate of climb (m/sec) vs u - dimensionless velocity. (b) q - dynamic pressure ($atm.$) vs u - dimensionless velocity.

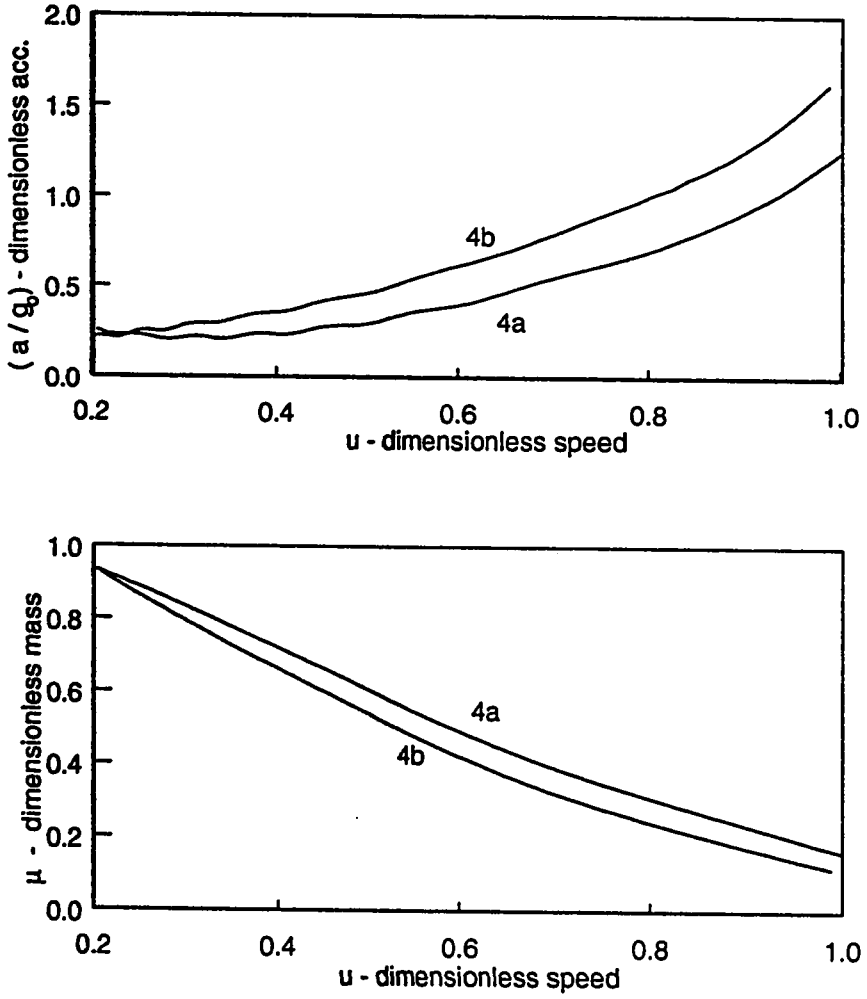

Figure 4.50: (a) (a/g_o) - dimensionless acceleration vs u - dimensionless velocity. (b) μ - dimensionless mass vs u - dimensionless velocity.

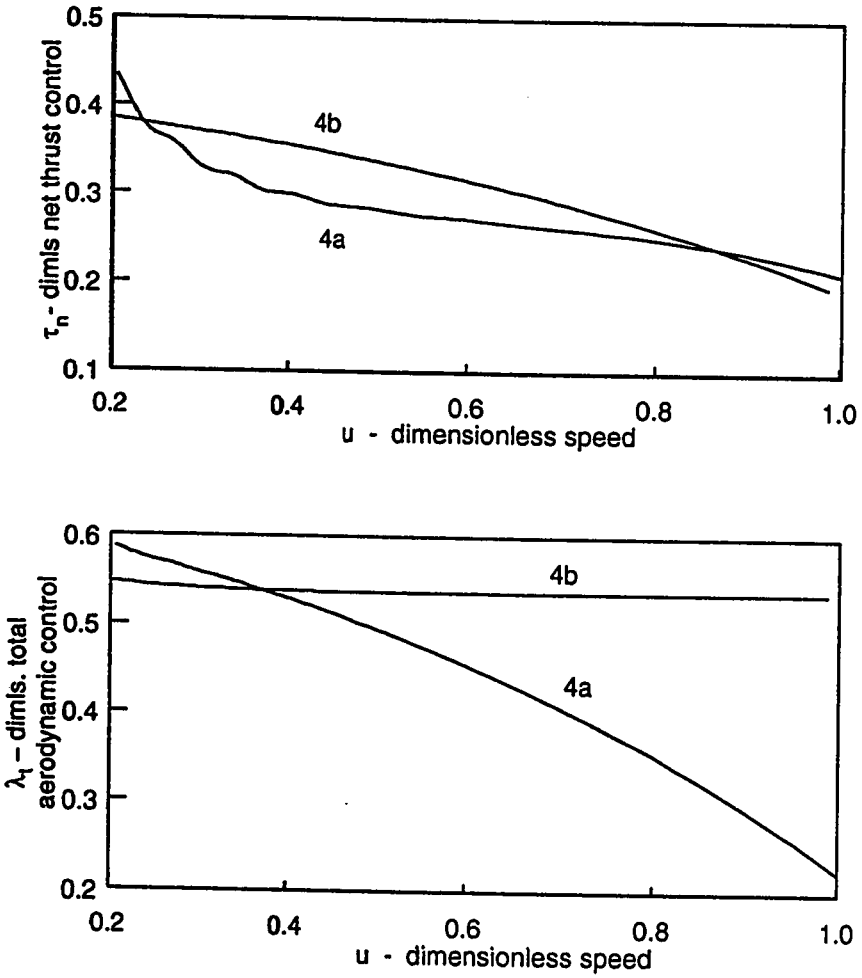

Figure 4.51: (a) τ_n - dimensionless net thrust control vs u - dimensionless velocity. (b) λ_t - dimensionless total aerodynamic control vs u - dimensionless velocity.

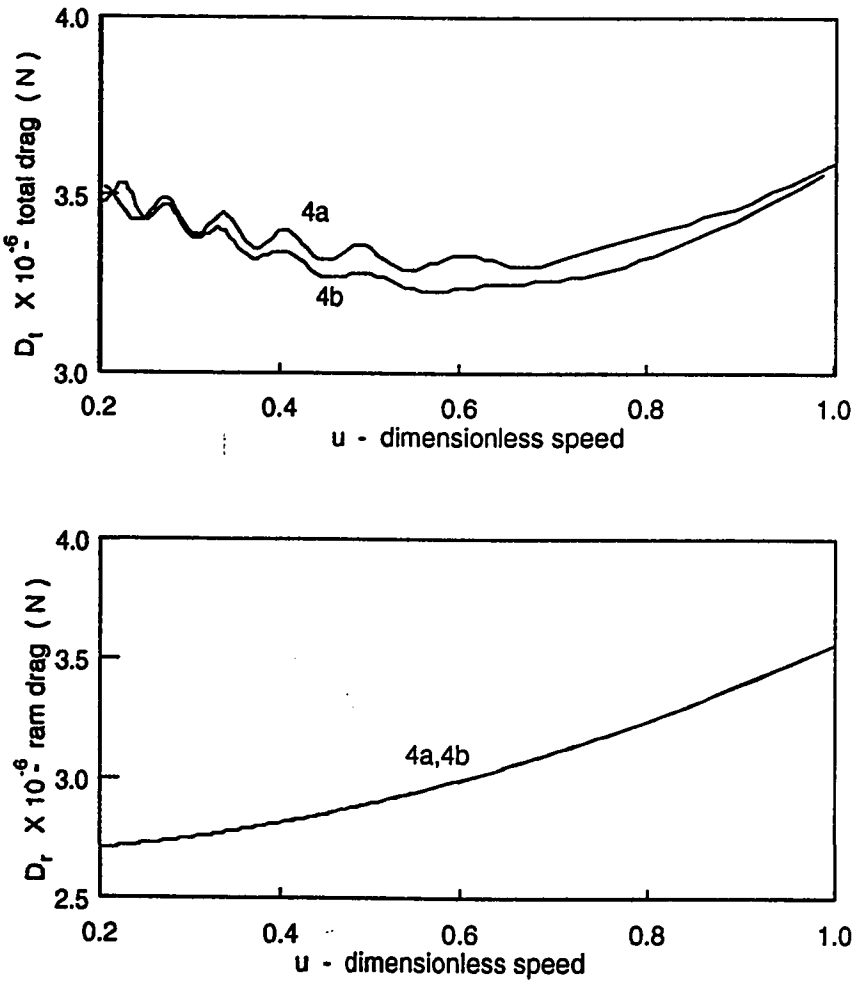

Figure 4.52: (a) D_t - total drag (N) vs u - dimensionless velocity. (b) D_r - ram drag (N) vs u - dimensionless velocity.

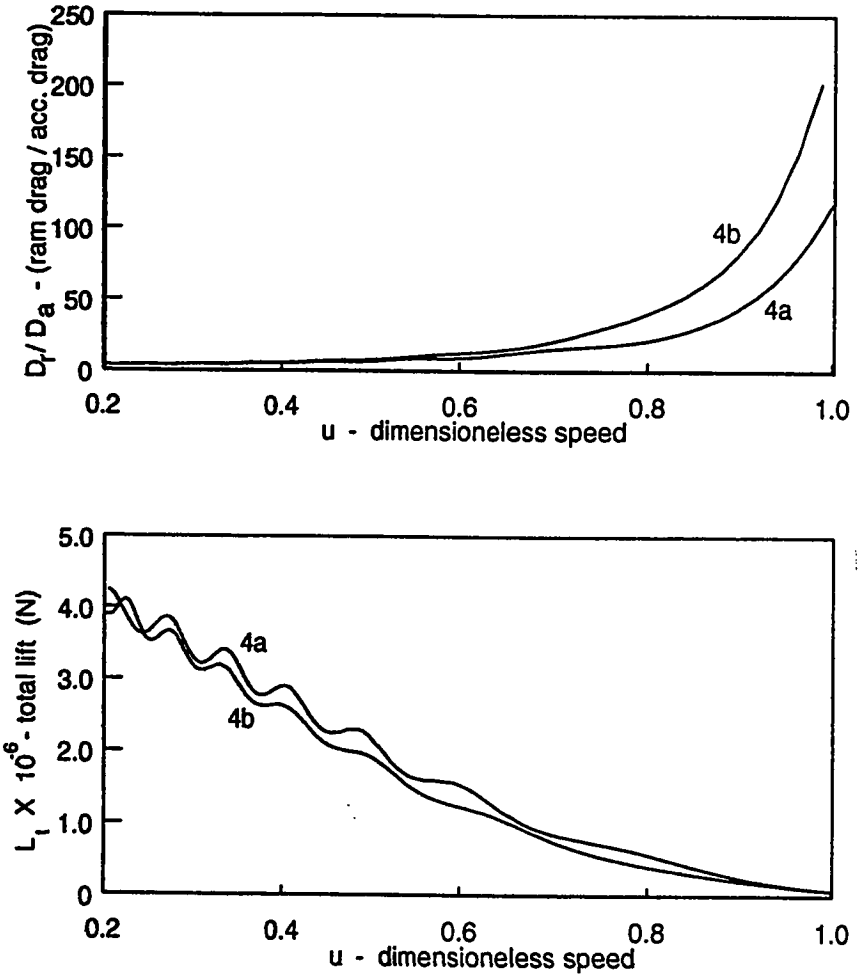

Figure 4.53: (a) D_r/D_a - (ram drag / aerodynamic drag) vs u - dimensionless velocity. (b) L_t - total lift (N) vs u - dimensionless velocity.

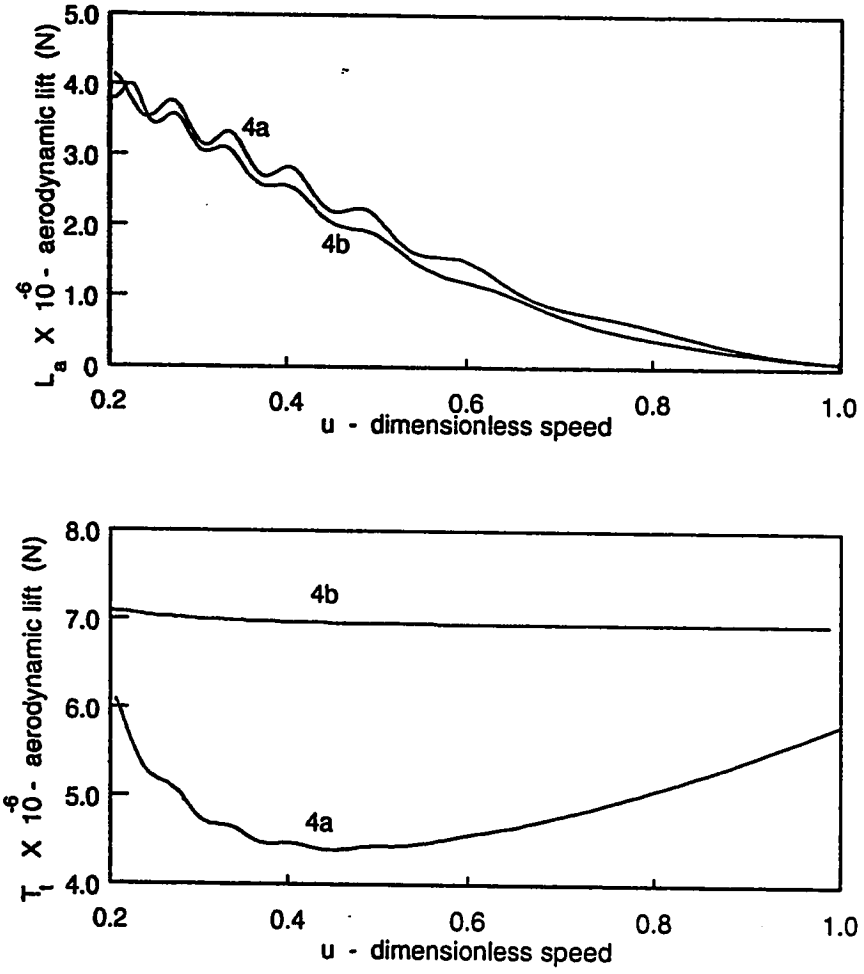

Figure 4.54: (a) L_a - aerodynamic lift (N) vs u - dimensionless velocity. (b) T_t - total thrust (N) vs u - dimensionless velocity.

4.5 Comparison Between Neural and Polynomial Controller

The following is a comparison between the polynomial and the neural controller,

1. The trajectories obtained using the neural controller are much smoother than those obtained using polynomial controller.

2. It was much easier to obtain feasible solutions using neural controller than while using the polynomial controller. This is very helpful, since it saves a lot of computer time.

3. Neural networks are known to have a capability of representing any nonlinear function given a sufficiently large number of nodes. Thus it is more reasonable to use a neural controller than a polynomial controller, when the functional form of the required controls are not known in advance.

4. It is observed that the desired level of control is not attained by varying τ or λ individually. i.e., for example, if you want to hit a final height h_f with two different velocities u_1 and u_2. It is not possible to attain this objective by just varying τ. In fact λ should also be simultaneously varied to get the desired result. This simultaneous variation of thrust control τ and aerodynamic control λ is difficult when we are using two different polynomials for τ andλ. Whereas this coupling of τ andλ is inherent in a neural controller. Thus a

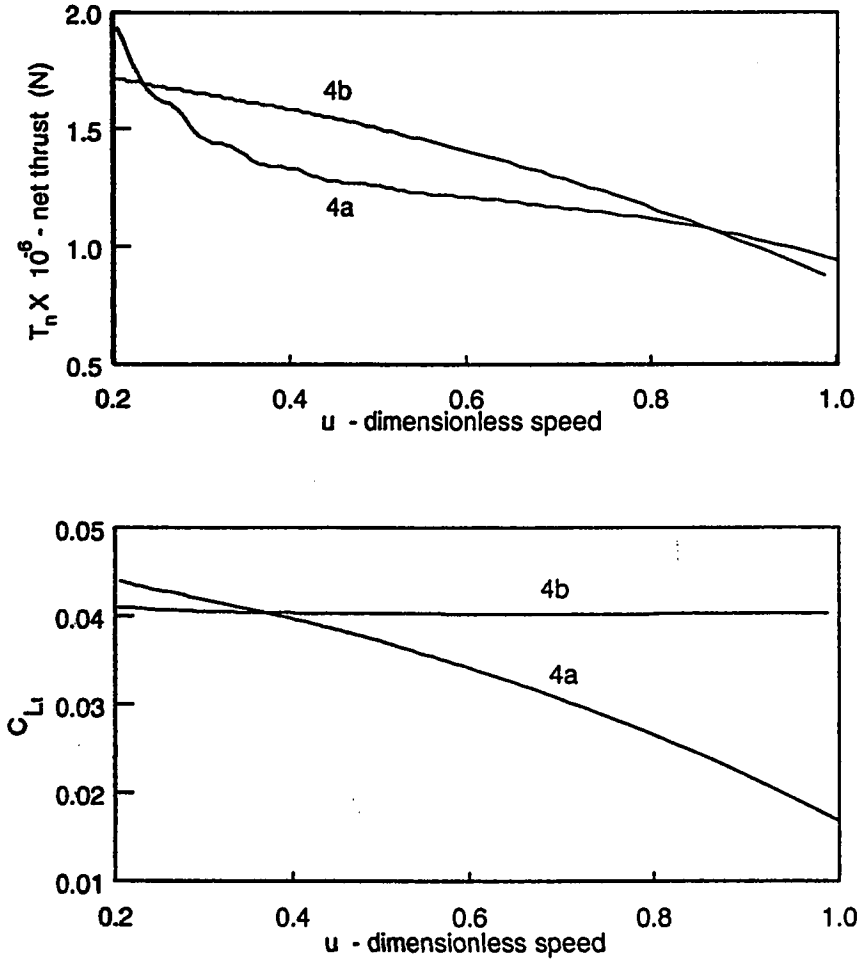

Figure 4.55: (a) T_n - net thrust (N) vs u - dimensionless velocity. (b) C_{Lt} - coefficient of total lift vs u - dimensionless velocity.

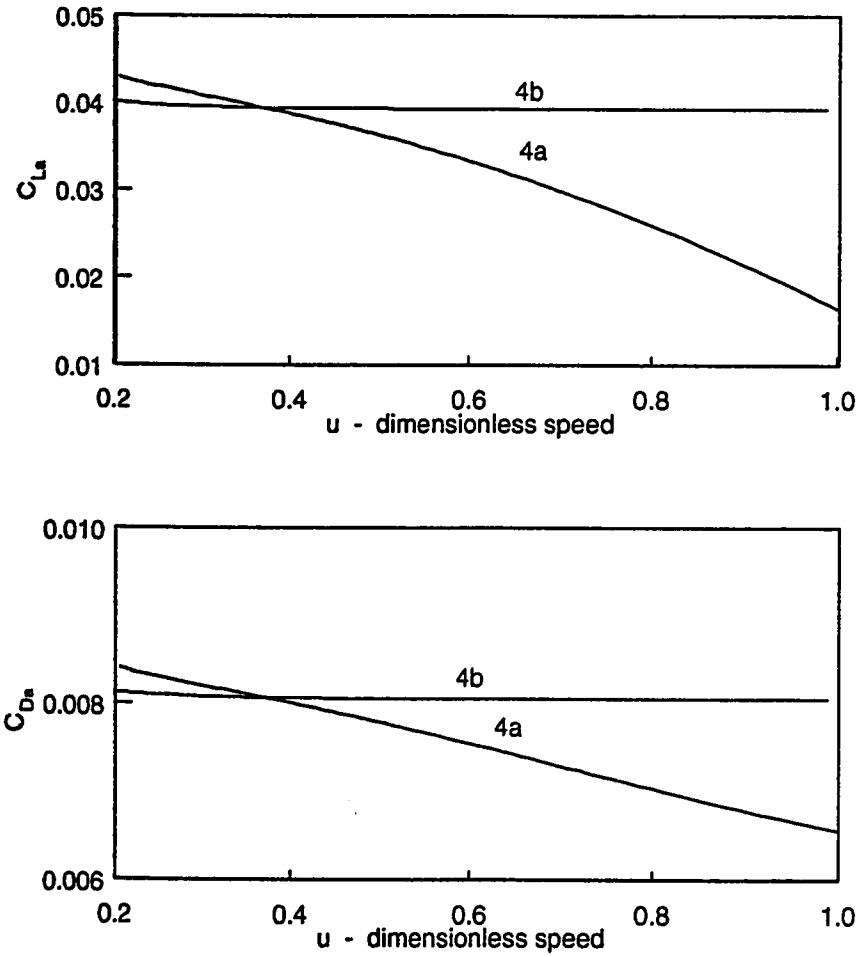

Figure 4.56: (a) C_{La} - coefficient of aerodynamic lift vs u - dimensionless velocity. (b) C_{Da} - coefficient of aerodynamic drag vs u - dimensionless velocity.

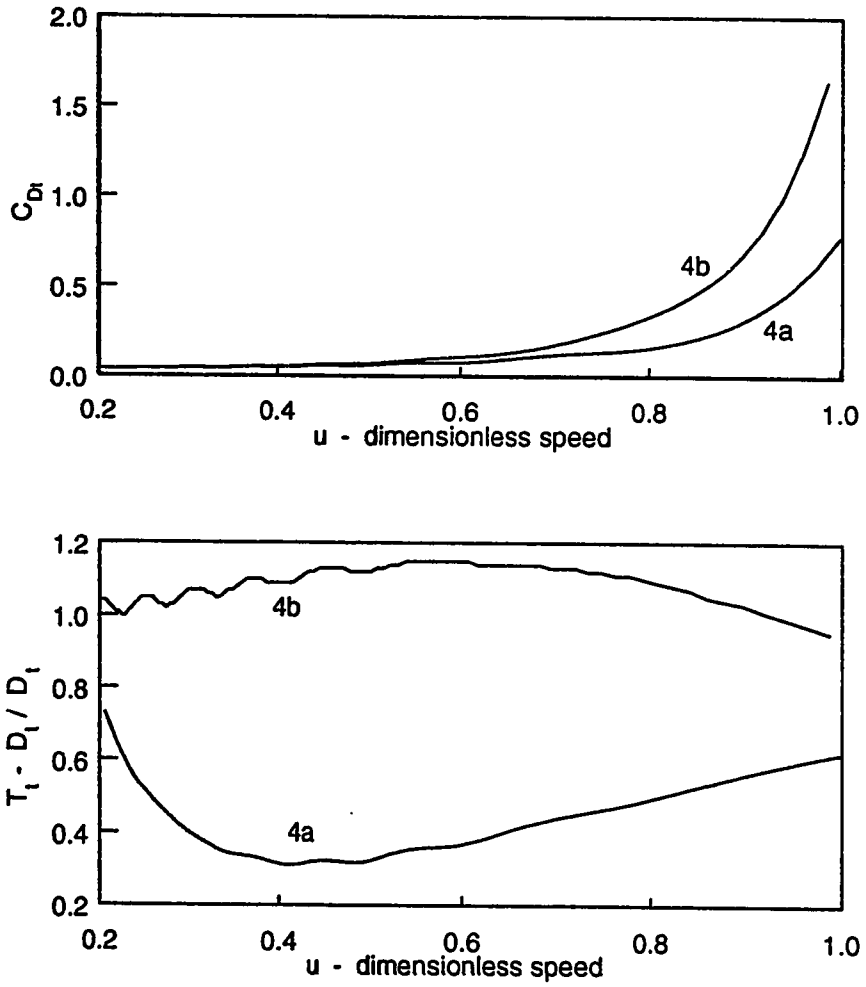

Figure 4.57: (a) C_{Dt} - coefficient of total drag vs u - dimensionless velocity. (b) $T_t - D_t/D_t$ vs u - dimensionless velocity.

better control is achievable using an neural controller. This was also observed while performing the simulation study.

5. It is observed that the heat loads obtained when using neural controller is slightly higher than those obtained using polynomial controller. This is because of the sub-optimal nature of the study under consideration. However, the results obtained are in an acceptable range.

6. It is seen that the fuel spent in some cases using the neural controller is higher. Even though the constraints on the fuel mass are satisfied in all cases, efficient use of fuel is very beneficial. In this respect the neural controller seems to be better. However, we should note that our objective was only to minimize the heat load, and was not concerned with fuel consumption.

Chapter 5

CONCLUSIONS AND FUTURE WORK

5.1 Conclusions

The study of control of hypersonic flight trajectories is of prime importance in the development of future hypersonic vehicles. This study has produced sub-optimal solutions to the trajectory optimization problem. An overview of the fundamental concepts needed for performing this study is presented. This includes derivation of equations of motion, the atmosphere, aerodynamic and propulsive forces, hypersonic aerodynamic heating and an introduction to neural network. On the basis of this fundamentals the problem of minimizing the heat load is formulated as a non-linear optimization problem. All necessary constraints that arise due to physical and

mission requirements are incorporated.

Two different forms of controllers are used to transform the optimization problem into a finite dimensional problem. The two controllers used are polynomial controller and neural controller.

An extensive optimization and simulation study was performed to obtain sub-optimal solutions to the problem. Our cases are studied by varying initial and final altitudes and by considering specific impulse as a constant or variable. Each case is studied by using both the polynomial controller and neural controller. The results obtained in general satisfying all the physical and mission constraints. This shows that the trajectories lie within reasonable flight corridor. The heat loads obtained are also within reasonable limits.

It is seen that there is not much difference in the trajectories obtained by considering the specific impulse constant or variable. The main affect is on the fuel consumption. From the comparison of the polynomial and neural controller it is seen that the overall performance of neural controller is better. However, in some instances the results obtained by the polynomial controller are better. Further studies with different forms of neural and polynomial controllers are needed to confirm these results.

In general the study performed shows that the minimized heat loads for hypersonic vehicles using air-breathing engines is in the range of $300kJ/cm^2$ to $350kJ/cm^2$. The new (neural) control scheme introduced performs very well and might serve as

a good alternative to the other forms of controllers.

5.2 Suggestions for future research

1. Studies could be performed with 3-D equations of motion, i.e., relaxing the constraint of flight in the equatorial plane.

2. We have studied one form of a neural controller, in future studies variations of the neural controller could be studied and its effect on the optimal trajectories ascertained.

3. Studies could be carried out to obtain optimal solutions to this problem.

4. In the equations used in this study some of the vehicles parameters have been assumed. For a more accurate study we can make use of experimental data or real life data. For example β, reciprocal of the scale height is assumed constant, this may be improved by using more data such as that obtained form real flight tests. The drag polar for aerodynamic forces could be a source of error, this can be improved by considering experimental data.

Appendix A

THE CONTROLLER PARAMETERS

Controller Parameters CASE 1a

$$t_f = 1.6000$$

$$a_1 = 0.8999 \quad a_2 = 0.4299 \quad a_3 = 0.9696E-01$$

$$b_1 = 0.6000 \quad b_2 = 0.3399 \quad b_3 = -0.1718E-01$$

$$d_1 = 0.6000 \quad d_2 = 0.1999 \quad d_3 = 0.7499E-01$$

Controller Parameters CASE 1b

$$t_f = 1.6000$$

$$[W] = \begin{bmatrix} -0.2486 & 0.6345E-01 & -0.9052 \\ 0.4989 & 0.6528 & -0.3964E-08 \end{bmatrix}$$

$$[X] = \begin{bmatrix} 0.4428 & 0.7118E-01 \\ 0.2631E-01 & 0.1900 \\ -0.4170 & 0.1856 \end{bmatrix}$$

$$d_1 = 0.6000 \quad d_2 = 0.19999 \quad d_3 = 0.2600E-01$$

Controller Parameters CASE 2a

$$t_f = 1.6000$$

$$a_1 = 0.8500 \quad a_2 = 0.4399 \quad a_3 = 0.9700E-01$$

$$b_1 = 0.6000 \quad b_2 = 0.3399 \quad b_3 = -0.1700E-01$$

$$d_1 = 0.6000 \quad d_2 = 0.1999 \quad d_3 = 0.7499E-01$$

Controller Parameters CASE 2b

$$t_f = 1.6000$$

$$[W] = \begin{bmatrix} 0.2486 & 0.6345E-01 & 0.9052 \\ 0.4989 & 0.9086E-01 & 0.0000 \end{bmatrix}$$

$$[X] = \begin{bmatrix} 0.8000E-01 & 0.7039E-01 \\ 0.2631E-01 & 0.9000E-01 \\ -0.4170 & 0.8562E-01 \end{bmatrix}$$

$$d_1 = 0.6000 \quad d_2 = 0.1999 \quad d_3 = 0.2600E-01$$

Controller Parameters CASE 3a

$$t_f = 1.6000$$

$$a_1 = 0.8932 \quad a_2 = 0.4617 \quad a_3 = 0.9019E-01$$

$$b_1 = 0.6000 \quad b_2 = 0.3399 \quad b_3 = -0.1637E-01$$

$$d_1 = 0.6000 \quad d_2 = 0.19999 \quad d_3 = 0.7499E-01$$

Controller Parameters CASE 3b

$$t_f = 1.6000$$

$$[W] = \begin{bmatrix} 0.2486 & 0.6345E-01 & 0.1052 \\ 0.4989 & 0.9086E-01 & 0.3964E-01 \end{bmatrix}$$

$$[X] = \begin{bmatrix} 0.8000E-01 & 0.7039E-01 \\ 0.2631E-01 & 0.9000E-01 \\ -0.4170 & 0.8562E-01 \end{bmatrix}$$

$$d_1 = 0.6000 \quad d_2 = 0.1999 \quad d_3 = 0.2600E-01$$

Controller Parameters CASE 4a

$$t_f = 1.6000$$

$$a_1 = 0.8201 \quad a_2 = 0.4856 \quad a_3 = 0.1025$$

$$b_1 = 0.5686 \quad b_2 = -0.3499 \quad b_3 = 0.3505E-02$$

$$d_1 = 0.6000 \quad d_2 = 0.1999 \quad d_3 = 0.2600E-01$$

Controller Parameters CASE 4b

$$t_f = 1.6000$$

$$[W] = \begin{bmatrix} 0.7324E-01 & 0.6345E-01 & 0.1559E-01 \\ 0.5229E-01 & 0.9086E-01 & -0.7514E-03 \end{bmatrix}$$

$$[X] = \begin{bmatrix} 0.1000 & 0.5460E-02 \\ 0.2892E-01 & 0.1400 \\ 0.6928E-01 & 0.8562E-01 \end{bmatrix}$$

$$d_1 = 0.6000 \quad d_2 = 0.1999 \quad d_3 = 0.2600E-01$$

Bibliography

[1] Tauber M.E. and Manees G.P. Aerothermo dynamics of transatmospheric vehicles,. *AIAA paper 86-1257.* 1986.

[2] Allen H.J. Eggers A.J and Neice S.E. Comprative analysis of the performance of long-range hypervelocity vehicles,. *NCCA Report No. 1382.*. 1958.

[3] Chapman R.R. An approximate analytical method for studying entry into planetary atmospheres,. *NACA TN 4276.*. 1958.

[4] Vinh N.X. Minimum fuel rocket maneuvers in horizontal flight.. *AIAA Journal. Vol. 11, No. 2.*. February 1973.

[5] Jr. Griffin J.W. Optimal three dimensional maneuvers of rocket powered hypervelocity vehicles with lift, bank angles and thrust control,. *Ph.D. Dissertation. Department of Aerospace Engineering. University of Michigan.*. 1973.

[6] Bletsos N. Buseman A., Vinh N.X. and Culp R.D. Flight with lift modulation inside a planetary atmosphere,. *International Astonautical Fedration (I.A.F.).*

123

Anaheim, California, 1976.

[7] Throckmorton D.A. Benchmark aerodynamic heat transfer data fromthe first flight of the space shuttle orbiter,. *AIAA-82-ooo3*,, January 1982.

[8] Rochelle W.C. Curry D.M. and Chao D.C. Space shuttle orbiter nose cap thermal analysis,. *AIAA-86-0388*, January 1982.

[9] Greenwood T.F. Foster I.D. and Lee D.B. Shuttle system ascent aerodynamic and plume heating,. *Shuttle Performance: Lessons Learned NASA CP 2283.*, March 1983.

[10] Al-Garni A.Z. Assending trajectories performance and control to minimize the heat load for the transatmospheric aerospace planes.. *Ph.D. Dessertation. Department of Aerospace Engineering, University of Maryland, College Park. Maryland.*, 1991.

[11] Al-Garni A.Z. and Barlow J. The ascending trajectories performance and control to minimize heat load for the transatmospheric aerospace planes.. *Journal of Guidance. Control. and Dynamics.*, August 1992.

[12] Al-Garni A. Analytical solutions for controls, heat and states of flight trajectories. *AIAA(JSR)*, 1994.

[13] N. X. Vinh. *Optimal Trajectories in Atmospheric Flight.* Elsevier Scientific Publishing Company, Amsterdam, 1981.

[14] Busemann A. Vinh N. X. and Culp R. D. *Hypersonic and Plenatery Entry Flight Mechanics.* University of Michigan Press Ann Arbor, Michigan, 1980.

[15] U.s. standard atmosphere, 1976. *NOAA, NASA, and USAF. Washington, DC,* 1976.

[16] Anderson Jr.J. D. *Introduction to Flight. Third Edition.*. McGraw-Hill. New York, 1989.

[17] Anderson Jr. J. D. *Fundementals of Aerodynamics.* McGraw-Hill, New York, 1984.

[18] Perkins C. D. and R. E. Hage. Airplane performance stability and control. *John Wiley and Sons. New York,* 1949.

[19] Marcum Jr D. C. Penlund J. A. and Stack S. H. Wall-temperature effects on the aerodynamics for hydrogen-fueled transport concept in mach 8 blowdown and shock tunnels. *NASA TP 2159.* pages 339 356. July 1983.

[20] Anderson Jr J. D. Bowcutt K. G. and Capriotti D. Viscous optimized hypersonic waveriders. *AIAA-87-0272. AIAA 25th Aerospace Science Meeting,* January 1987.

[21] Corda S. and Anderson Jr. J. D. Viscous optimized hypersonic waveriders designed from axisymmetric flow fields. *AIAA-88-0369. AIAA 26th Aerospace Sciences Meeting,* January 1988.

[22] Ken L. David A. W., Albion B. and John M. Flight, propulsion, and thermal control of advanced aircraft and hypersonic vehicles. *Handbook of Intelligent Control: Neural, Fuzzy and Adaptive Approaches*, 1992.

[23] Crzu C. I. Powell R. W., Shaughnessy J. D. and Naftel J. C. Ascent performance of an air breathing horizontal takeoff launch vehicle. *Journal of Guidance*, 14(4), 1991.

[24] Swithenbank J. Hypersonic air-breathing propulsion. *Progress in Aeronautical Sciences*, 1966.

[25] Anderson Jr. J. D. *Hypersonic and High Temperature Gas Dynamics*. McGraw-Hill Book Company, New York. 1989.

[26] Hankey W.L. *Re-Entry Aerodynamics*. AIAA educational series, 1988.

[27] Marvin J. G. and Deiwert G. S. Convective heat transfer in planetary gases. *NASA TR R-224*, July 1965.

[28] Shultz H. Aurthur P. D. and Gaurs F. L. Flat plate turbulent heat transfer at hypervelocities. *Journal of Spacecrafts and Rockets*, October 1966.

[29] Jones R. A. and Donaldson C. From earth to orbit in a single stage. *Aerospace America*, 25(8), August 1987.

[30] Wasserman P. Neural computing. *Van Nostrand Reinhold.New York*, 1988.

[31] Martinez-Sanchez M. Fundementals of hypersonic airbreathing propulsion. *Department of Aeronautics and Astronautics, MIT., AIAA, Profesional Study Series*, July 1988.

[32] Short Course Siminar Notes. Hypersonics: Technologies. applications andthe national aero-space plane. *Barthelemy. M.E.. duPont. A. A.. Green. M.. Heppenheimer. T. A. and Schaufele. R.. University extension. University of California, Irvine. California*, June 1992.

[33] Weinder J. P. Edwards C.L.W., Small W. J. and Johnston P. J. Studies of scramjet/airframe integration techniques for hypersonic aircraft. *NASA Langley Research Center. Hampton. Virginia 23665. Presented at the AIAA 13th. Aerospace Sciences Meeting. Pasadena. California*, January 1975.

[34] NASA Scientific and Technical Information Facility. A study of composite propulsion systems for advanced launch vehicle applications. *Summary Report. September 1966. Report No. 25.194. NASA-377. Project 5042. The Marquardt Corporation Rocketdyne. Lockeed-California Company.*, 1966.

[35] Wang T. Miele A. and Melvin W.W. Optimal abort landing trajectories in the presence of wind shear. *Journal of Optimization Theory and Aplications*. 55(2). November 1987.

[36] Cybenko G. Approximation by superposition of sigmoidal function. *Mathematics of Control signals and systems*, 2(4):303–314, 1989.

[37] Stinchcomb M. Hornik K. and White H. Multilayer feedforward networks are universal approximators. *Neural Networks*. 2:359–366. 1989.

[38] Al-Garni A. and Nizami S. J. Optimization and simulation package. *King Fahd University of Petroleum and Minerals, Saudi Arabia*, 1992.

[39] Imsl/math library, version 2.0. *IMSL Inc. Houstan. TX. USA*.. 1993.

[40] Jian L. Z. and Tits A. L. *Users Guide for FSQP Version 3.0d.* 1993.

[41] Lewis M. J. The prediction of inlet flow stratification and its influence on the performance of air-breathing hypersonic propulsion systems. *Doctor of Science Thesis, Department of Aeronautics and Astronautics. MIT*, June 1988.

Vita

- SYED SHAH ALI KHASIM JAVEED NIZAMI
- Born in Hyderabad, India
- Received Bachelor's degree in Mechanical Engineering from the Osmania University of Engineering and Technology, Hyderabad, India in July , 1991.
- Completed Master's degree requirements at King Fahd University of Petroleum and Minerals, Dhahran, Saudi Arabia in June, 1994.